Higher-Order Correlations in Complex Liquids

Dissertation
zur Erlangung des Doktorgrades
an der Fakultät für
Mathematik, Informatik und Naturwissenschaften
Fachbereich Physik
der Universität Hamburg

vorgelegt von

Michael Dartsch, geb. Koof

Hamburg

2021

Gutachter/innen der Dissertation:	Prof. Dr. Gerhard Grübel Prof. Dr. Arwen Pearson
Zusammensetzung der Prüfungskomission:	Prof. Dr. Gerhard Grübel Prof. Dr. Arwen Pearson Prof. Dr. Michael Potthoff Prof. Dr. Volker Abetz Prof. Dr. Alf Mews
Vorsitzender der Prüfungskomission:	Prof. Dr. Michael Potthoff
Datum der Disputation:	20.01.2022
Vorsitzender des Fach-Promotions-ausschusses Physik:	Prof. Dr. Wolfgang Hansen
Leiter des Fachbereichs Physik:	Prof. Dr. Günter Hans Walter Sigl
Dekan der Fakultät MIN:	Prof. Dr. Heinrich Graener

Abstract

Colloidal dispersions show a peculiar rheological behavior known as shear-thinning, that is the viscosity of a sample decreases with increasing shear rate. In this work the underlying structural changes that lead to this effect are studied by using samples consisting of polyacrylate-coated silica nanoparticles dispersed in polyethylene glycol-200. The silica particles are synthesized using a modified Stöber method and samples with volume fractions between $\phi = 0.22$ and $\phi = 0.53$ are prepared.

The experiments performed in this thesis utilize a setup combining a cone-plate rheometer with a small-angle x-ray scattering (SAXS) setup. In this way rheological and structural properties of the samples can be measured simultaneously. Data collected from the SAXS measurements are evaluated further using x-ray cross-correlation analysis (XCCA) in order to study higher-order correlations and local symmetries.

It is shown that under shear the highly concentrated nanoparticle dispersions form structures with hexagonal symmetry which can be interpreted as layers of hexagonal close-packed spheres. From XCCA the sixth Fourier coefficient of the cross-correlation function can be used as an order parameter to quantify the degree of local hexagonal order. In the regime of intermediate shear rates the degree of hexagonal order is correlated with the magnitude of the shear rate. An increase of the shear rate corresponds to an increase of local hexagonal order. Since the viscosity is decreasing with increasing shear rate it can be concluded that a higher degree of local order minimizes internal friction of the sample, and therefore lowers its viscosity.

Kurzfassung

Kolloidale Dispersionen zeigen ein interessantes Verhalten, das unter dem Begriff Scherverdünnung bekannt ist. Dies bedeutet, dass die Viskosität einer Probe mit steigender Scherrate abnimmt. In der vorliegenden Arbeit werden die strukturellen Veränderungen, die für diesen Effekt verantwortlich sind, mittels Proben untersucht, die aus polyacrylatbeschichteten Silica-Nanopartikeln bestehen, welche in Polyethylenglykol-200 dispergiert sind. Die Silica-Partikel werden mithilfe einer modifizierten Stöber-Synthese hergestellt und Proben mit Volumenanteilen zwischen $\phi = 0.22$ und $\phi = 0.53$ präpariert.

Die Experimente dieser Arbeit nutzen einen Versuchsaufbau, der ein Kegel-Platte-Rheometer mit Röntgenkleinwinkelstreuung (SAXS) kombiniert. Hierdurch können die rheologischen und strukturellen Eigenschaften der Proben gleichzeitig gemessen werden. Die Daten der SAXS-Messungen werden zusätzlich durch Röntgenkreuzkorrelationsanalyse (XCCA) evaluiert, um Korrelationen höherer Ordnung und lokale Symmetrien zu analysieren.

Es wird gezeigt, dass hoch konzentrierte Nanopartikeldispersionen unter Scherung Strukturen mit hexagonaler Symmetrie ausbilden, die als Schichten von hexagonal dichtest gepackten Kugeln interpretiert werden können. Aus den XCCA-Daten kann der sechste Fourierkoeffizient der Kreuzkorrelationsfunktion als Ordnungsparameter zur Quantifizierung der hexagonalen Ordnung herangezogen werden. Im Bereich mittlerer Scherraten ist der Grad der hexagonalen Ordnung mit dem Betrag der Scherrate korreliert, das heißt, die hexagonale Ordnung nimmt mit steigender Scherrate zu. Da die Viskosität mit zunehmender Scherrate abnimmt, kann daraus gefolgert werden, dass ein höherer Grad lokaler Ordnung die innere Reibung der Probe und damit ihre Viskosität reduziert.

Contents

1 Introduction

Colloidal dispersions are two-phase systems of particles in the nanometer length scale dispersed in a continuous medium. These systems can be catagorized as soft matter which is a subdivision of condensed matter systems. For these kind of materials, inter-particle interaction energies are in the regime of the thermal energy and, thus, structural changes can be introduced easily, either by mechanical or thermal stress.

The response of a material to external mechanical stress is studied in the field of rheology. Most colloidal dispersions show a peculiar rheological behavior that is known as shear thinning. When such a system is subject to shear deformation, its viscosity decreases with increasing shear rate, i. e. it becomes more liquid as the system is deformed faster. A prominent example from everyday life is wall paint. At rest, the paint is relatively viscous, which is desired so that it sticks to a brush and does not drip. When moving the brush along the wall, shear forces are applied to the paint and the viscosity decreases. In that way, the paint can be spread on the wall easier. In the end, after lifting the brush, no shear forces are present and the paint becomes more viscous again, preventing it from flowing down the wall.

The macroscopic rheological phenomenon of shear thinning is supposed to be attributed to microscopical changes of the structure of the dispersion. The investigation of this relationship is called structural rheology. In early work, the structure of colloidal dispersions under shear was investigated by means of small-angle neutron scattering[1–5]. These studies were later followed up by light scattering[6–8] as well as small-angle x-ray scattering[5,9] experiments.

In early publications by Ackerson et al.[1,6] and Ashdown et al.[2] the emergence of Bragg reflections with hexagonal symmetry in the scattering pattern of the sample under shear was observed. These were explained by the formation of face-centred cubic (FCC) crystallites with the (111) plane oriented perpendicular to the incoming beam. In 1994 Versmold offered a reinterpretation and attributed the phenomenon to the formation of hexagonal sliding layers[10]. This model was later backed up by additional theoretical work[11–15].

These studies considered the shear melting of already preordered structures and dealt with scattering data averaged over comparably large amounts of time, i. e. in the regime of minutes. The formation of order in a disordered sample by the application of shear forces and the subsequent decrease of viscosity is, however, not well studied yet.

The focus of this thesis is a detailed time-resolved analysis and quantification of the structure formation in colloidal dispersions under shear in the millisecond regime. As a model system, spherical silica nanoparticles with a hard-sphere interaction potential are prepared. With the advent of modern third-generation

synchrotron sources, x-ray scattering experiments with exceptionally high spatial and temporal resolution became possible. In this thesis, the recently developed x-ray cross-correlation analysis method [16,17] is used to extract symmetry information from small-angle x-ray scattering data of colloidal dispersions under shear and use this information as an order parameter to characterize the degree of order in the sample. The results are then combined with rheological measurements to illuminate the underlying relationship between structure formation induced by shear forces and the decrease of viscosity with increasing shear rates.

The thesis is structured as follows: In **chapter 2**, a general introduction into colloidal systems is given. Different stabilization mechanisms will be reviewed and typical pair-interaction potentials will be discussed. The preparation of silica nanoparticle dispersions will be presented, as well.

Chapter 3 gives an overview of the basic principles of rheology. The commonly used rheometer setups will be presented.

In **chapter 4** scattering methods will be introduced. First, a brief theoretical overview of the interaction between light and matter will be given. Afterwards, small-angle x-ray scattering and x-ray cross-correlation analysis will be illuminated further. In the end, the principles of dynamic light scattering which is used for the sample pre-characterization are discussed.

The experimental approach of this thesis will be presented in **chapter 5**. The results of the sample preparation as well as the characterization are discussed and the experimental setup will be illustrated together with the applied measurement scheme.

Chapter 6 is the main part of the thesis. The results of the experiments are presented and discussed in detail in this section.

In the final **chapter 7**, the work is summarized and an outlook is given.

2 Colloidal Systems

The IUPAC defines the term *colloidal* as "a state of subdivision, implying that the molecules or polymolecular particles dispersed in a medium have at least in one direction a dimension roughly between 1 nm and 1 µm, or that in a system discontinuities are found at distances of that order" [18]. A colloidal dispersion is a two-phase mixture where the dispersed substance is evenly distributed in a continuous medium. As a consequence, to form a colloidal dispersion one component must be insoluble in the other one.

Colloidal length scales are intermediate between atomic or molecular scales on the one hand and macroscopic aggregates on the other hand. Therefore, in science, colloids are often used as mesocopic model systems for atomic or molecular substances. The advantage is, that dynamic processes on the colloidal scale are much slower than their microscopic counterparts and easier to investigate. In addition, the structure formation on these larger length scales is less difficult to probe as well. Since the time and length scales of the particles and the dispersion medium are different by several orders of magnitude the dispersion medium can be considered a continuum. This makes it possible to describe the properties of colloids while neglecting the microscopic peculiarities of the medium.

Colloidal dispersions occur commonly in our everyday live. Some prominent examples are milk (fat dispersed in water), blood (cells dispersed in water), or mayonaise (oil droplets dispersed in water). Furthermore, colloids are widely used in technological applications such as agents cosmetics, color pigments in paints, or as a supporting material in industrial processes.

In general, in a colloidal dispersion the dispersed substance and the continuos medium can occur in various different combinations of aggregate states. In this work, the focus lies on colloidal suspensions, that is a solid substance is dispersed in a liquid medium. The underlying properties and principles of colloidal suspensions will be described in the following sections. For the most part, only spherical particles are considered.

2.1 Van der Waals attraction

If the dispersed particles and the continuous phase exhibit different polarizabilities, which is typically the case for colloidal dispersions, van der Waals forces lead to an attractive potential between the particles. The attractive forces are a result of random fluctuations in the electron cloud of the particles which lead to instantaneous electric dipoles. These dipoles can induce further dipoles in neighboring particles and create attractive interactions. These interactions are also referred to as London dispersion forces [19–21].

A general van der Waals potential is of the form

$$V_{\mathrm{vdW}}(r_{ij}) = -\frac{C}{r_{ij}^6} \quad . \tag{2.1}$$

Here, r_{ij} denotes the distance between two molecules i and j and C is a constant depending on the substance. Typically, the dispersion energy is in the range of around 4-10 kJ/mol and therefore weak compared to other interaction mechanisms such as electrostatic interactions. From equation 2.1 it can be seen that the pair-potential decreases with a factor of r_{ij}^{-6}, hence it is relatively short-ranged.

For identical, spherical, homogeneous particles of radius R dispersed in a continuous medium the attractive potential can be described using the Hamaker-constant H [22,23]

$$V_{\mathrm{a}}(r_{ij}) = -\frac{H}{6}\left[\frac{2R^2}{r_{ij}^2 - 4R^2} + \frac{2R^2}{r_{ij}^2} + \ln\left(1 - \frac{4R^2}{r_{ij}^2}\right)\right] \quad . \tag{2.2}$$

The constant H depends on the material properties as well as the medium in which the particles are dispersed. Equation (2.2) shows that the attractive forces between two mesoscopic spherical bodies in a medium is more long-ranged in comparison to the molecular scale.

2.2 Stabilization Mechanisms

Due to the origin of the van der Waals forces, all materials and substances are subject to attractive interactions. As a result particles dispersed in a medium are thermodynamically unstable and would inevitably coagulate irreversibly and precipitate in the form of macroscopic clusters. To overcome this problem, different stabilization mechanisms can be used to stabilize a colloidal dispersion.

2.2.1 Steric Stabilization

One possible way to avoid agglomeration in colloidal dispersions is steric stabilization [24]. Here, the particles are coated with short-chain ligands in a brush-like fashion which is displayed schematically in figure 2.1.

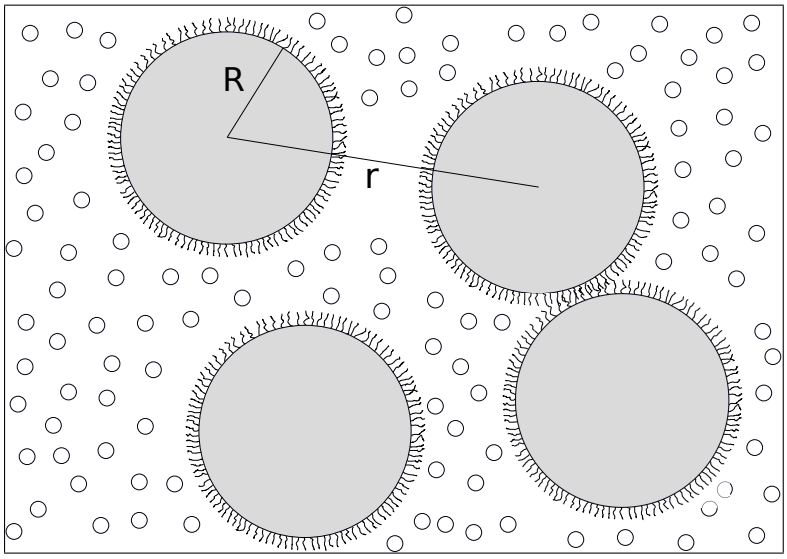

Figure 2.1: Schematic of a sterically stabilized colloid dispersion (adapted from [24]). The open circles represent the constituents of the dispersion medium. The particles of radius R are separated by a center-to-center distance r and are colored in gray. Their surfaces are modified with brush-like ligands resulting in an entropic repulsion at short distances.

Before two particles' surfaces touch the ligands interpenetrate each other which leads to an entropic repulsion of the overlapping molecule chains. Usually, the length of the molecule chains is much smaller compared to the size of the particles. In this case, the interaction between two particles i and j of radius R can be described by a simple hard-sphere potential:

$$V_{\mathrm{HS}}(r_{ij}) = \begin{cases} \infty, & r_{ij} < 2R \\ 0, & r_{ij} \geq 2R \end{cases} \tag{2.3}$$

It follows from equation (2.3) that the interaction potential is independent of temperature. The only contribution is the inter-particle distance or the volume fraction ϕ, respectively, which can be calculated by

$$\phi = \frac{4}{3}\pi R^3 \rho_{\mathrm{N}} \quad , \tag{2.4}$$

where ρ_N is the number density of hard-sphere particles. Depending on the volume fraction, these kind of particles show an interesting phase behavior[25]. At low volume fractions the particles form a liquid-like structure with short-range order and long-range disorder. At higher volume fractions even crystalline phases can be observed, whereas intermediate volume fractions exhibit a coexistance between both phases.

In addition, non-equilibrium states, such as glassy and supercooled states, can form. However, the formation of these phases require a disperse sample. A phase of hard-sphere particles is displayed in figure 2.2.

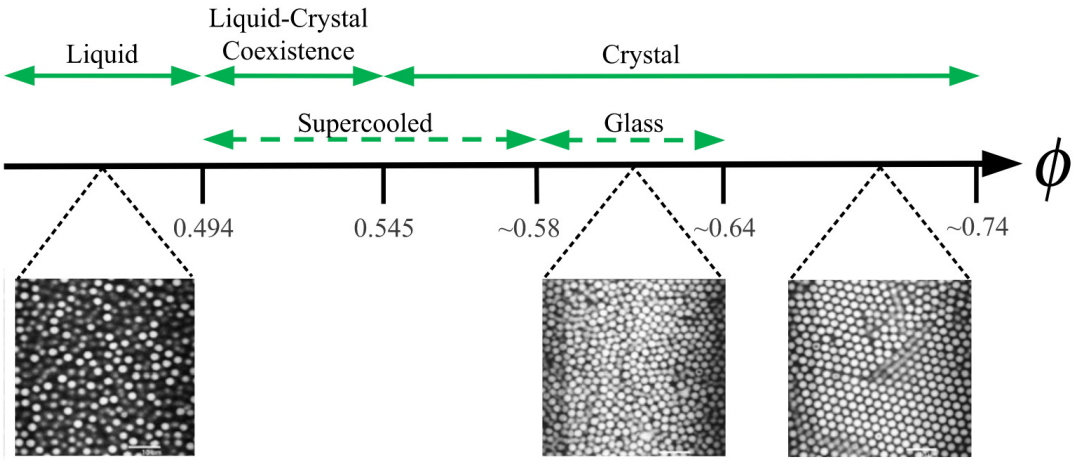

Figure 2.2: Phase diagram of monodisperse hard spheres as a function of the volume fraction ϕ (taken from [25]).

2.2.2 Electrostatic Stabilization

Another possibility of stabilizing colloidal dispersions is the addition of electrostatic interaction. This can be realized by introducing surface charges to the colloids which is usually achieved by dissociation of acidic end-groups, e.g. silanol (-Si-OH), carboxyl (-CO_2H), or sulfonic acid (-SO_3H) groups, in polar solvents. As a result, the particles become strongly charged, with surface charges between 10^2 - 10^5 elementary charges[26].

The surface charge of the particles leads to a long-ranged electrostatic repulsion which counteracts the short-ranged attractive van der Waals interaction. It must be taken into account that a dispersion itself must satisfy the principle of electroneutrality, i.e. the colloidal macroions are surrounded by dissolved counterions which form an electrochemical double layer. The double layer shields the charge of the particle so that a second particle experiences the force of an effective charge Z_{eff} which is lower than the nominal charge. A schematic of a charge-stabilized dispersion is illustrated in figure 2.3.

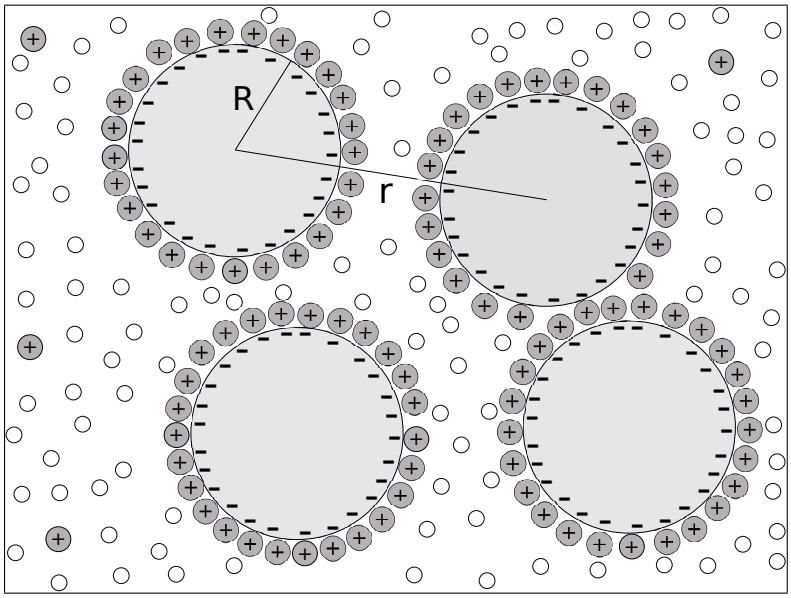

Figure 2.3: Schematic of a charge-stabilized colloid dispersion (adapted from [24]). The constituents of the dispersion medium are illustrated as open circles. The colloids, colored in gray, carry a negative surface charge. The positive counterions dissolved in the dispersion medium form an electrochemical double layer at the colloid surfaces.

The interaction potential of charge-stabilized colloidal dispersions can be described by the DLVO-theory[27,28], which is named after Derjaguin, Landau, Verwey, and Overbeek. The DLVO-potential consists of three contributions: a volume exclusion described by the hard-sphere potential (see equation (2.3)), the attractive van der Waals potential (see equation (2.1)), and an repulsive electrostatic part which can be expressed by a screened Coulomb or Yukawa potential

$$V_{\mathrm{Yukawa}}(r_{ij}) = \frac{(Z_{\mathrm{eff}}e_0)^2}{4\pi\varepsilon_0\varepsilon_{\mathrm{r}}}\left(\frac{\exp(\kappa R)}{1+\kappa R}\right)^2\frac{\exp(-\kappa r_{ij})}{r_{ij}} \quad . \tag{2.5}$$

In equation (2.5) Z_{eff} is the effective charge of the colloidal particles, e_0 the elementary charge, ε_0 the vacuum permittivity, and ε_{r} the relative permittivity of the continuous phase. r_{ij} is the distance of two particles i and j of radius R. κ is the inverse Debye-screening length which can be calculated by

$$\kappa^2 = \frac{4\pi\rho_{\mathrm{c}}(qe_0)^2}{\varepsilon_0\varepsilon_{\mathrm{r}}k_{\mathrm{B}}T} \quad . \tag{2.6}$$

Here, ρ_{c} is the number density of counterions with a charge of qe_0. k_{B} denotes Boltzmann's constant and T the absolute temperature. Ultimately, the DLVO potential can be expressed as

$$V_{\mathrm{DLVO}} = V_{\mathrm{HS}} + V_{\mathrm{Yukawa}} + V_{\mathrm{vdW}} \quad . \tag{2.7}$$

Similar to the hard-sphere particles described in the section before, charge-stabilized particles can as well form a variety of different phases. In addition to the volume

fraction, also the electrolyte concentration of the dispersion medium contributes to the phase behavior.

A phase diagram for charged polystyrene particles dispersed in a methanol-water mixture is displayed exemplarily in figure 2.4[29]. Due to the charge, the particles experience a more long-ranged interaction compared to hard-sphere particles. Hence, phase transitions can be observed at much lower volume fractions. At a constant electrolyte concentration and with an increasing volume fraction the dispersions undergo a transition from liquid-like to crystalline to a glassy state. With increasing electrolyte concentrations, the phase boundaries shift to higher volume fractions. At high electrolyte concentrations, where the screening of the particle charges has the largest effect, the particles behave similar to a hard-sphere systems.

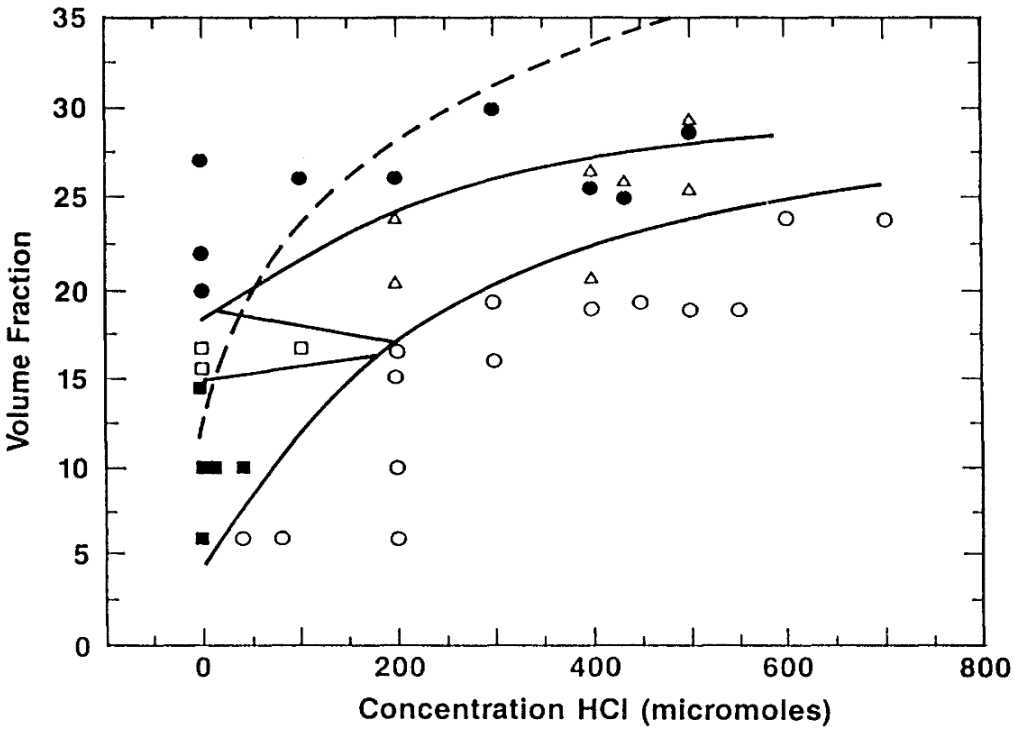

Figure 2.4: Phase diagram of spherical, charge-stabilized, polysterene particles in a 0.9-methanol-0.1-water mixture (taken from[29]). The phases are displayed as a function of the volume fraction and the concentration of hydrochloric acid. Solid squares: bcc crystals; open triangles: fcc-crystalls; open squares: fcc+bcc coexistance; closed circles: glass; open circles: liquids. Solid lines are guide-to-the-eye phase boundaries whereas the dashed line is the theoretical fcc-liquid boundary for a similar point-charge Yukawa system.

2.3 Preparation of silica nanoparticle dispersions

The preparation of silica nanoparticle dispersions can be achieved using two general pathways[30]: In the so called bottom-up approach the nanoparticles are grown chemically starting from a molecular level. On the other hand a macroscopic bulk material, e.g. quartz, can be dispersed in a medium using various size reduction techniques. This latter physical process is referred to as the top-down approach. In this work, the dispersions are prepared chemically. The method used is described in the following paragraphs.

In 1968 the Stöber process[31] was developed and is a widely used bottom-up approach to prepare charge-stabilized, spherical silica particles in the nanometer to micrometer size range. The advantage of this particular synthesis is that the resulting particles are uniform, monodisperse and controllable in size[32].

For the synthesis a molecular, silicic acid based precursor, commonly tetraethyl orthosilicate, is reacted with water in an alcoholic solution. Aqueos ammonia solution is used as a catalyst. The hydrolysis of the orthosilicate leads to a deesterification and a subsequent polycondensation of the substrate forming a siloxane network. The network is end-capped with silanol groups which dissociate in polar solvents resulting in a negative surface charge of the particles. Thus, the particles experience an electrostatic repulsion preventing them from agglomeration while the electrically neutral orthosilicate monomers are still able to diffuse to the particle surface and propagate the polymer growth.

The reaction mechanism can be described as follows. In the beginning of the reaction, tetraethyl orthosilicate is deesterified with water using aqueous ammonia solution as a catalyst

$$\mathrm{Si(OEt)_4 + x\ H_2O \xrightarrow{NH_4OH} Si(OEt)_{4-x}OH_x + x\ EtOH} \quad . \tag{2.8}$$

In the next step, the silanol groups react in a polycondensation to form the siloxane network

$$\mathrm{(RO)_3Si{-}OH + HO{-}Si(OR)_3 \longrightarrow (RO)_3Si{-}O{-}Si(OR)_3 + H_2O} \quad , \tag{2.9}$$

$$\mathrm{(RO)_3Si{-}OEt + HO{-}Si(OR)_3 \longrightarrow (RO)_3Si{-}O{-}Si(RO)_3 + EtOH} \quad . \tag{2.10}$$

The nucleation and growth process as well as the influence of the reactant concentrations and solvents have been studied extensively and are well understood[33]. By tuning the concentration of ammonia, water, and the monomer the particle size can be controlled while still obtaining monodisperse particle dispersions. It is also possible to effectively modify the particle surface using silane-coupling agents. Both the modified and unmodified particles exhibit interesting mechanical, thermal, physical, and chemical properties and, thus, are widely used as a filler material in polymer nanocomposites for various applications[30].

3 Rheology

Rheology is the study of flow and deformation. It investigates the response of condensed matter to an external stress. As a result of a rheological measurement one can determine if a material behaves "hard" or "soft" or, viewed differently, if a substance is more "solid-like" or "liquid-like", respectively.

In this chapter, the basic principles of this technique will be introduced. The main sources sued for this section are *Rheology: Principles, Measurements, and Apllications* by Christopher Macasko[34] and *The Structure and Rheology of Complex Fluids* by Ronald G. Larson[35].

3.1 Basic Principles

The basic behavior of matter under shear forces can be visualized by imagining two parallel plates separated by a small distance h as depicted in figure 3.1. The gap between both plates is filled with a liquid.

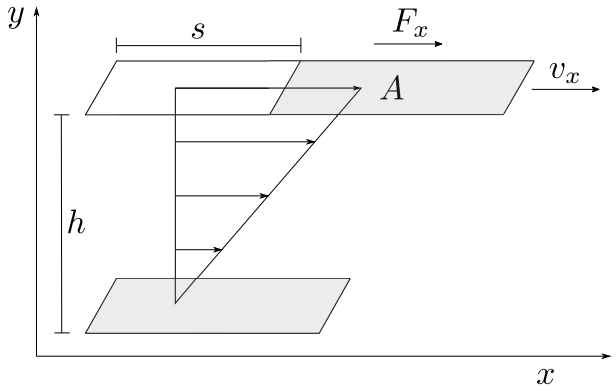

Figure 3.1: Schematic of a shear process. Two plates are separated by a small distance h. The gap between the plates is filled with a liquid. The lower plate is stationary while the upper one is moving with a constant velocity v_0. Due to the upper plate's motion, a velocity gradient forms inside the liquid.

While the upper plate is moving with a constant velocity of v_0 the lower plate remains at rest. Over time, the liquid layer directly in contact with the moving plate will start moving, too, and, due to momentum transfer in the normal direction, the adjacent layer will get in motion as well. In steady state, the layer closest to the moving plate will move with the same velocity as the plate whereas the bottom most layer will stay stationary. As a result, a linear velocity gradient

with a velocity distribution of

$$v_x = v_0 \frac{y}{h} \tag{3.1}$$

is established. To keep the upper plate moving at a constant velocity a force F_x needs to be applied to overcome the internal friction of the liquid. The ratio of that force to the area of the plate is called the shear stress

$$\tau = \frac{F_x}{A} \tag{3.2}$$

and has the unit of a pressure.

Another property of interest is the strain or shear deformation γ. Since the steady state velocity gradient is linear, the shear deformation is independent of the absolute position y between the plates and, thus, can be defined as

$$\gamma = \frac{\mathrm{d}s}{\mathrm{d}h} \quad , \tag{3.3}$$

where s is the upper plate's path of deflection.

Finally, the shear rate $\dot{\gamma}$ can be defined as the temporal derivative of the deformation which is the same as the velocity gradient normal to the applied force F_x

$$\dot{\gamma} = \frac{\mathrm{d}\gamma}{\mathrm{d}t} = \frac{\mathrm{d}}{\mathrm{d}t}\left(\frac{\mathrm{d}s}{\mathrm{d}h}\right) = \frac{\mathrm{d}}{\mathrm{d}h}\left(\frac{\mathrm{d}s}{\mathrm{d}t}\right) = \frac{\mathrm{d}v}{\mathrm{d}h} \quad . \tag{3.4}$$

Shear forces can be induced by two basic principles. The first case, called drag flow, is described in the section above. Here, the force is exerted by the drag of a moving surface.

The second possibility is pressure flow. In that case, the material is pushed through a channel by a pressure difference between the inlet and the outlet. This kind of shear forces is typically found for liquids flowing through a tube, e. g. in microfluidics applications or inside the nozzle of a liquid jet experiment [36–38].

Considering liquids the most basic law describing the deformation in response to external stress is Newton's law of viscosity

$$\tau = \eta\dot{\gamma} \quad , \tag{3.5}$$

where η is the dynamic viscosity of the liquid. Substances following this law, that is the stress is proportional to the shear rate, are considered Newtonian fluids. Most molecular liquids and gases, such as water or air, behave like this.

However, there are many liquids, especially dispersions and polymer melts, that deviate from the Newtonian behavior. Then, the viscosity is a function of the shear rate which is illustrated in figure 3.2. If the viscosity decreases with increasing shear rate this phenomenon is referred to as shear thinning. On the other hand, an increase of the viscosity at higher shear rates is called shear thickening. This peculiar macroscopic behavior is accompanied by structural changes on the microscopic level. The investigation of these structural changes

under the influence of shear forces is known as structural rheology and is the main focus in this work.

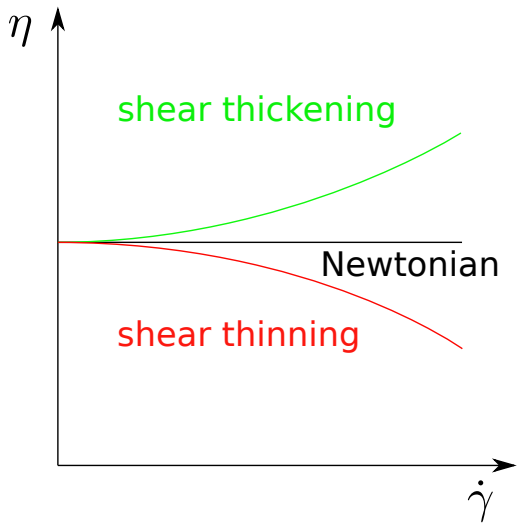

Figure 3.2: Different kinds of behavior of liquids under the influence of shear.

The most simple way to express deviations from the Newtonian behavior of liquids is in terms of a power law, the so called Ostwald-de Waele-relationship [39]

$$\tau = K\dot{\gamma}^n \quad , \tag{3.6}$$

$$\eta = K\dot{\gamma}^{n-1} \quad , \tag{3.7}$$

where K is called the flow consistency index and n the flow behavior index. $n = 1$ indicates Newtonian behavior, whereas $n < 1$ describes shear thinning and $n > 1$ shear thickening. This power law only approximates the behavior in certain ranges of shear rates. The parameters commonly change in the case of shear rates close to zero or high shear rates, respectively. This is because usually the structure of the fluid changes more drastically between the state at rest and low shear rates as compared to intermediate and higher shear rates, in which case the structure is more or less retained.

In the case of solids, the most simple relationship between force and deformation is Hooke's law

$$\tau = G\gamma \quad . \tag{3.8}$$

The constant of proportionality G is called the elastic modulus and is an inherent feature of solid materials.

Not all substances behave either "liquid-like" or "solid-like". Many materials, such as soft matter, exhibit features in between. These materials are called viscoelastic. One way to quantify the "hardness" or "softness" of a material is to perform rheological measurements under oscillatory shear. In this case, the sample is deformed as a sinusoidal function of time. As a result, the stress oscillates with the same frequency f, although shifted by a phase angle δ

$$\gamma(t) = \gamma_0 \sin(\omega t) \quad , \tag{3.9}$$

$$\tau(t) = \tau_0 \sin(\omega t + \delta) \quad , \tag{3.10}$$

where $\omega = 2\pi f$ is the angular frequency. The shear stress can be decomposed into two components, one in phase with the deformation and one shifted by $\pi/2$

$$\tau = \tau' + \tau'' = \tau_0' \sin(\omega t) + \tau_0'' \cos(\omega t) \quad . \tag{3.11}$$

Hence, the phase angle can be calculated as

$$\tan\delta = \frac{\tau_0''}{\tau_0'} \quad . \tag{3.12}$$

The viscous deformation in response to the external stress is time-dependent and irreversible while the elastic component is instantaneous and reversible. This can be expressed by defining two dynamic moduli G' and G''. G' is the elastic or storage modulus and is in phase with the deformation, thus, it corresponds to the elastic response of a material. G'' on the other hand is the out of phase component. It is called the loss modulus and indicates the viscous response to the external stress

$$G' = \frac{\tau_0'}{\gamma_0} \qquad G'' = \frac{\tau_0''}{\gamma_0} \qquad \tan\delta = \frac{G''}{G'} \quad . \tag{3.13}$$

Both dynamic moduli can be combined by expressing them as a complex modulus

$$G = G' + iG'' \,, \qquad \text{with} \quad |G| = \frac{\tau_0}{\gamma_0} \quad . \tag{3.14}$$

As a consequence, the dynamic viscosity becomes a complex property, too:

$$\eta = \eta' + i\eta'' \,, \qquad \text{with} \quad |\eta| = \frac{1}{\omega}|G| \tag{3.15}$$

$$\eta' = \frac{\tau_0''}{\dot\gamma_0} = \frac{G''}{\omega} \quad , \qquad \eta'' = \frac{\tau_0'}{\dot\gamma_0} = \frac{G'}{\omega} \quad , \tag{3.16}$$

where the shear rate is given by

$$\dot\gamma = \frac{\mathrm{d}\gamma}{\mathrm{d}t} = \gamma_0\omega\cos(\omega t) = \dot\gamma_0\cos(\omega t) \tag{3.17}$$

3.2 Rheometer Setups

Although there are many different setups for rheological measurements, the most prominent are the plate-plate, cone-plate, and a coaxial cylinder setup, called the Couette cell. Figure 3.3 shows all of the three setups schematically.

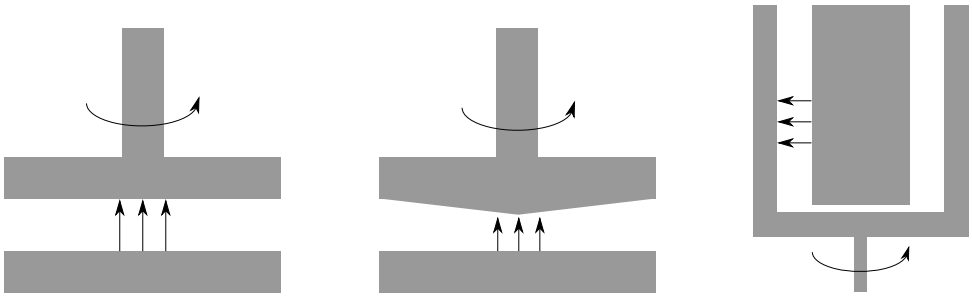

Figure 3.3: Different rheometer setups. Left: plate-plate setup, center: cone-plate setup, right: Couette setup. The arrows indicate the rotation axes and the direction of the shear gradient, respectively. Note: In contrast to figure 3.1 where one plane is sliding, here, the planes are rotating.

In these setups, the rheological measurements all work in the same way. The device measures the necessary torque required to reach a specific velocity and therefore a specific shear rate.

When comparing the different cell types in terms of the experiments performed in this work, the most important difference is the direction of the shear gradient, indicated by the arrows in figure 3.3. While in the plate-plate and cone-plate setups the gradient is parallel to the rotation axis, it is perpendicular in the case of the Couette cell. Considering the rheological measurements, this circumstance does not make any difference. However, in terms of the structural analysis, the direction of a probe compared to the direction of shear gradient is an important property, that needs to be kept in mind.

Even though the plate-plate and cone-plate setups seem similar in their general appearence, they exhibit a remarkable difference. In both cells the absolute velocity changes over the radius since the circumference near the rotation axis is smaller compared to the circumference at the edge of the cell. This means for the plate-plate setup, that the gradient of shear is a function of the distance from the rotation axis, i. e. the shear rate differs over the radius of the plate. The data analysis in that case is not straight forward. In the cone-plate setup, however, the opening angle of the cone (typically between 170°-180°) is chosen such that the difference of the velocities is compensated by the different gap widths so that the shear rate $\dot{\gamma} = v/h$ is constant over the whole radius of the cell.

4 Scattering Methods

In 1895 Wilhem Conrad Röntgen discovered an until then unknown type of radiation while experimenting with cathode rays which he called x-rays[40]. For this groundbreaking discovery Röntgen was awarded the first ever Nobel Prize in Physics in 1901.

In the following years scientists began utilizing this new type of radiation. Max von Laue found out that x-rays are diffracted by crystals and conclusions could be made about the atomic structure of the sample. With that finding the first x-ray scattering method was born. From here on out x-ray crystallography became an established tool to investigate the structure of a wide range of materials reaching from fairly simple minerals to very complex structures such as the DNA molecule[41] or protein-structures in general[42].

While crystalline substances with long-range order have been extensively investigated since the first half of the 20th century, the research of more complex samples in terms of positional and orientational order such as glasses, complex liquids, and soft matter[43,44] became possible by exploiting the features of synchrotron light sources beginning in the 1970s.

Since then a lot of progress has been made to refine the x-ray technology and push the experimental parameters to new limits. The recent advent of modern third-generation synchrotron sources as well as free-electron lasers and the resulting increase in photon flux and collimation enabled x-ray scattering experiments with exceptionally high spatial and temporal resolution.

In this chapter, the basic principles of the interaction of light, in particular x-rays, with matter as well as the scattering techniques used in this worked will be introduced. The main sources for this section are *Elements of Modern X-ray Physics* by Jens Als-Nielsen and Des McMorrow[45], *Soft-Matter Characterization* edited by Redouane Borsali and Robert Pecora[46], and *Dynamic Light Scattering* by Bruce J. Berne and Robert Pecora[47].

4.1 The Interaction of Light and Matter

X-rays are electromagnetic waves with wavelengths in the range of about 0.1 Å - 100 Å (1 Å = 10^{-10} m) and thus in the regime of interatomic length scales. The characteristic wavelength λ is often expressed in terms of the wave vector $\mathbf{k}$ defining the direction of propagation and having a magnitude of $k = |\mathbf{k}| = 2\pi/\lambda$. Mathematically the amplitude of the electric field can be described in the complex form

$$E(\mathbf{r}, t) = E_0 \exp\left[i\left(\mathbf{k}\cdot\mathbf{r} - \omega t\right)\right] \quad , \tag{4.1}$$

where E_0 is the maximum field amplitude, $\mathbf{r}$ is the spatial coordinate, ω the angular frequency, and t the time, respectively.

Depending on the energy a photon can interact with the electrons of an atom by either absorption or scattering. In an absorption process the energy of a photon is transferred to an electron which causes the electron to be expelled from the atom and hence results in a positive ionization. Quantitatively, absorption can be described by the attenuation of an incoming photon beam with a number of photons I_0 penetrating a sample with a penetration depth x by the relation

$$I(x) = I_0 \exp(-\mu x) \quad . \tag{4.2}$$

Here, μ is called the linear absorption coefficient and is a constant specific for a material at a given photon energy. The inverse of the absorption coefficient $1/\mu$ is called the attenuation length which is the penetration depths after which the initial number of photons has dropped to a value of $1/e$.

In a different process, instead of being absorbed, a photon can be scattered by a sample. The electric field of the incident x-rays exerts a force on the electrons of the sample. The electrons are accelerated and successively emit electromagnetic waves themselves isotropically. The scattered wave is then a result of the interference of these emitted waves. In the classical point of view, the photons are scattered *elastically*, i.e. the energies of the incident and the scattered photon remain the same. This is, however, not necessarily the case in a quantum mechanical consideration where the photon has a momentum of $\hbar\mathbf{k}$ which can be transferred to the electron in the scattering process so that the scattered photon would be lower in energy. This phenomenon of *inelastic* scattering is known as *Compton scattering*. Nevertheless, the dominating effect exploited by the methods and photon energies used in this work is the elastic scattering of x-rays and therefore the inelastic scattering will be neglected in this section.

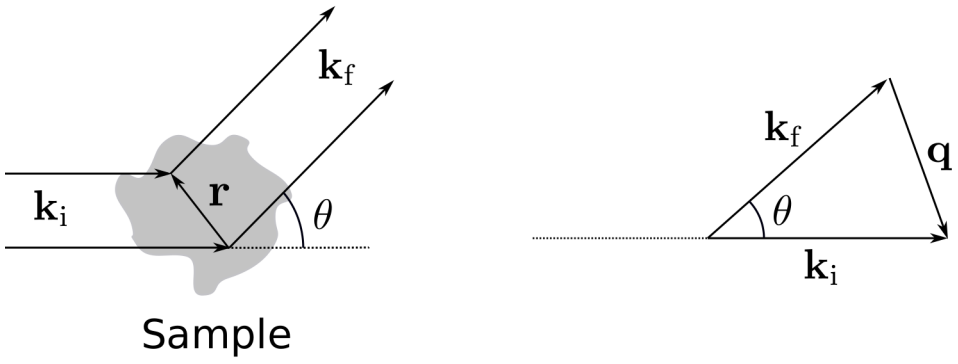

Figure 4.1: Illustration of an elastic scattering event. Left: Schematic overview; right: wave vector diagram.

The mechanism of an elastic scattering event is shown schematically in figure 4.1. The incident wave with wave vector $\mathbf{k}_i$ interacts with different points of the sample separated by $\mathbf{r}$ and is scattered by an angle θ. The difference of the wave vectors

of the incident and the scattered wave defines the scattering vector $\mathbf{q}$:

$$\mathbf{q} = \mathbf{k}_\mathrm{i} - \mathbf{k}_\mathrm{f} \quad . \tag{4.3}$$

The magnitude of the scattering vector can be calculated by

$$q = |\mathbf{q}| = \frac{4\pi n}{\lambda_\mathrm{vac}} \sin\frac{\theta}{2} \tag{4.4}$$

where n is the refractive index of the sample and λ_vac the vacuum wavelength of the photons. In case of x-rays, the refractive index of a material is close to unity and often omitted in the calculation.

4.2 Small-Angle X-ray Scattering

Spatial fluctuations of the electron density on length scales much larger than the wavelength of the incident photons lead to scattering in the region of small angles, typically below 10°. Small-angle x-ray scattering (SAXS) commonly considers scattering vectors in the range of roughly $0.006\ \mathrm{nm}^{-1} < q < 6\ \mathrm{nm}^{-1}$ which corresponds to length scales in the region of 1 nm to 1 µm.

When electromagnetic waves are scattered from multiple electrons, e.g., in atoms, molecules, or particles the resulting wave is a superposition of all scattered waves. For an atom containing Z electrons and with an electron density $\rho(\mathbf{r})$ the superposition of the scattering from all contributing volume elements $\mathrm{d}\mathbf{r}$ is described by the atomic form factor f_atom defined by

$$f_\mathrm{atom}(\mathbf{q}) = \int_\mathrm{atom} \rho(\mathbf{r}) \exp\left(i\mathbf{q}\cdot\mathbf{r}\right) \mathrm{d}\mathbf{r} \quad . \tag{4.5}$$

One can see from equation (4.5) that the scattered wave is the Fourier transfrom of the electron density. This means the real space electron distribution is converted to properties in reciprocal space, i.e. large distances d in real space are converted to small scattering vectors, and therefore small angles, in reciprocal space via $d = 2\pi/q$. For the limit of $q \to 0$, equation (4.5) approaches the total number of electrons Z of the atom.

For a molecule which consists of multiple atoms the molecular form factor F_molecule can be calculated by the sum of scattered waves from each individual atom

$$F_\mathrm{molecule}(\mathbf{q}) = \sum_j f_{\mathrm{atom},j}(\mathbf{q}) \exp\left(i\mathbf{q}\cdot\mathbf{r}_j\right) \quad . \tag{4.6}$$

A direct result from equation (4.6) is that if the scattering amplitude F_molecule is measured for sufficiently many values of $\mathbf{q}$ in principle the relative positions of individual atoms $\mathbf{r}_j$ could be retrieved.

In the next higher step of complexity one can consider particles consisting of multiple molecules. In that case the scattered wave is described by

$$E(\mathbf{q}, t) = E_0 \sum_{n=1}^{N} F_n(\mathbf{q}) \exp\left(i\mathbf{q}\cdot\mathbf{r}_n - i\omega t\right) \quad . \tag{4.7}$$

In a SAXS experiment the utilized photon detectors will only detect the photon intensity and not the field amplitude. These properties are related by

$$I(\mathbf{q},t) = |E(\mathbf{q},t)|^2 \quad . \tag{4.8}$$

Using equation (4.7) this results in

$$\begin{aligned} I(\mathbf{q}) &= \sum_n F_n(\mathbf{q}) \exp\left(i\mathbf{q}\cdot\mathbf{r}_n\right) \sum_m F_m(\mathbf{q}) \exp\left(-i\mathbf{q}\cdot\mathbf{r}_m\right) \\ &= |F(\mathbf{q})|^2 \sum_n \sum_m \exp\left[i\mathbf{q}\cdot(\mathbf{r}_n - \mathbf{r}_m)\right] \quad . \end{aligned} \tag{4.9}$$

As a consequence only the amplitude of the scattered waves is measured and the information about the phase is lost. This phenomenon is widely known as the phase problem. To overcome this limitation, e.g. in order to extract the aforementioned positions of atoms in a molecule, elaborate methods of phase retrieval must be utilized. These will, however, not be discussed in this work.

4.2.1 Form Factor of monodisperse systems

For a dilute system of N identical non-interacting particles the scattering intensity is given by

$$I(\mathbf{q}) = N\,|F(\mathbf{q})|^2 \tag{4.10}$$

and mainly depends on the shape and size of the particles. Since the particles are usually dispersed in a medium the relevant parameter determining the scattering intensity is the difference of the electron density of the particles and the medium $\Delta\rho = \rho_\mathrm{P} - \rho_\mathrm{M}$ and thus

$$F(\mathbf{q}) = \int \Delta\rho(\mathbf{r}) \exp\left(i\mathbf{q}\cdot\mathbf{r}\right) \mathrm{d}\mathbf{r} \quad . \tag{4.11}$$

In case of particles with a spherical symmetry the spatial average results in

$$F(q) = 4\pi \int_0^\infty \Delta\rho(r) \frac{\sin(qr)}{qr} r^2 \mathrm{d}r \tag{4.12}$$

and is only dependent on the magnitude of the scattering vector q. For a solid spherical particle with radius R, an electron density difference

$$\Delta\rho(r) = \begin{cases} \Delta\rho, & r \le R \\ 0, & r > R \end{cases} \tag{4.13}$$

and the integration of equation (4.12) results in

$$I(q) = |F(q)|^2 = V^2\Delta\rho^2 \left(\frac{3\left[\sin(qR) - qR\cos(qR)\right]}{(qR)^3} \right)^2 \tag{4.14}$$

$$= V^2\Delta\rho^2 P(q,R) \tag{4.15}$$

where $P(q, R)$ is the form factor of spherical particles with Volume V.

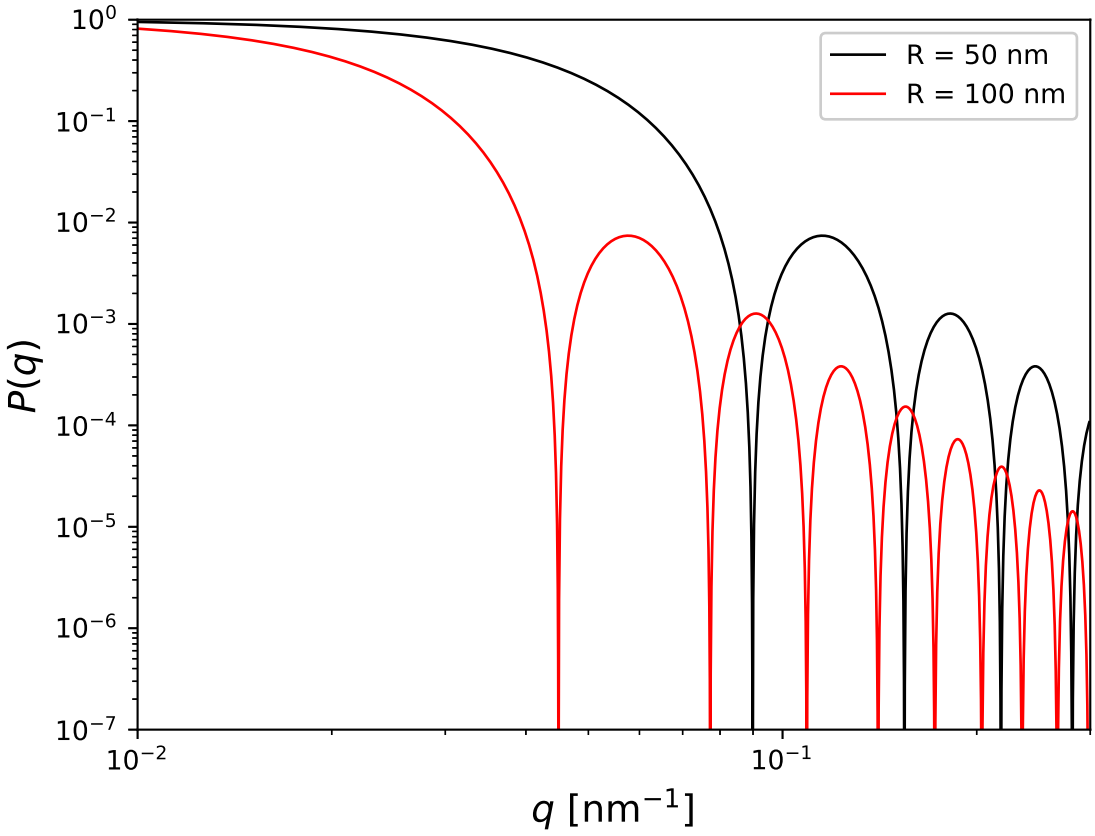

Figure 4.2: Calculated form factor of solid spherical particles for different radii.

Figure 4.2 illustrates the calculated form factor of monodisperse spherical particles with different radii. The form factor exhibits an oscillating behavior with decreasing amplitude. The slope of this decrease is proportional to q^{-4}, which is known as Porod's law, and the minima are shifted to lower scattering vectors with increasing radii. The first minimum can be observed at $qR \approx 4.49$.

4.2.2 Form factor of disperse systems

In reality, most colloidal particles synthesized by e.g. polycondensation or radical polymerization are not uniform in size. Their size distribution can commonly be described with a Schulz-Zimm distribution[48–52]:

$$D(R, \overline{R}, Z) = \frac{1}{(Z+1)!} \left(\frac{Z+1}{\overline{R}} \right)^{Z+1} R^Z \exp\left(-R \cdot \frac{Z+1}{\overline{R}} \right) \tag{4.16}$$

where R and $\overline{R}$ are the radius and the mean radius of the particles, respectively. Z is a parameter describing the width of the distribution. One can calculate the dispersity p via

$$p = \frac{\Delta R}{\overline{R}} = \frac{1}{\sqrt{Z+1}} \quad . \tag{4.17}$$

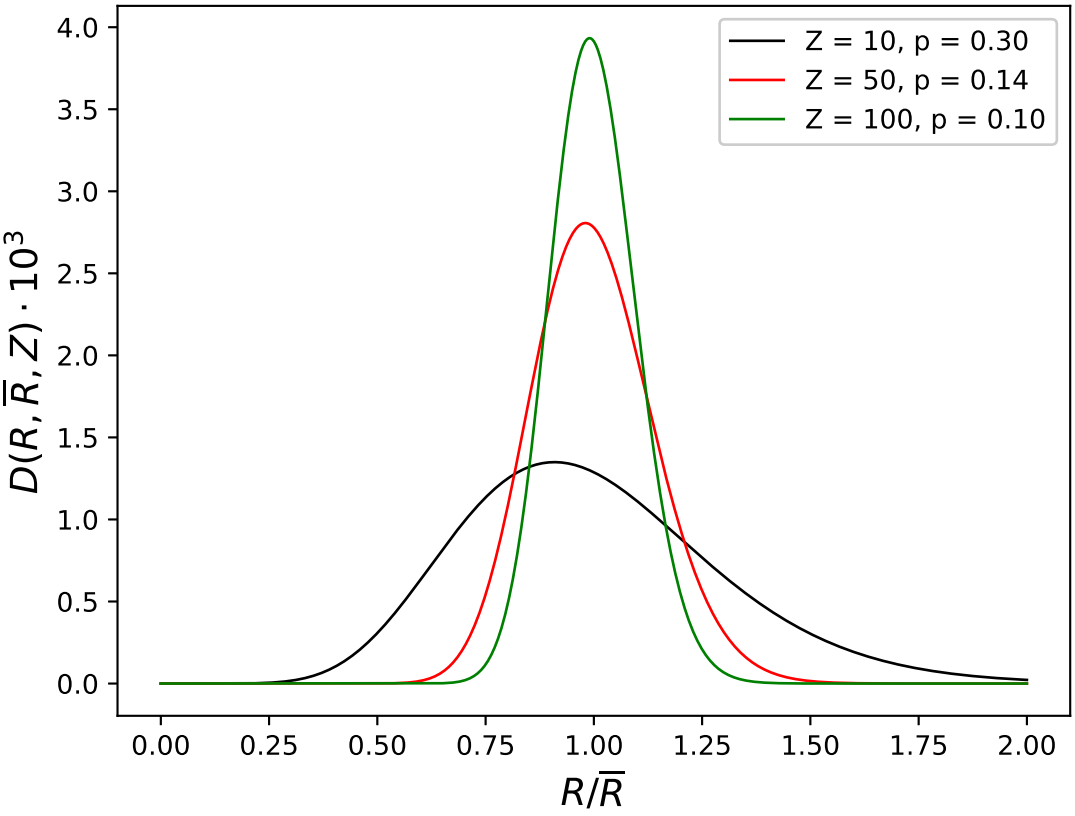

Figure 4.3: Schulz-Zimm distribution for different Z parameters.

Figure 4.3 shows the Schulz-Zimm distribution for varying parameters of Z.

To calculate the scattering intensity of a disperse sample, the size distribution must be taken into account:

$$I(q) = N\Delta\rho^2 \int_0^\infty D(R)V^2(R)P(q,R)\mathrm{d}R \qquad \text{with} \qquad \int D(R)\mathrm{d}R = 1 \quad . \tag{4.18}$$

In this case, the form factor can be calculated analytically using equation (4.19) [48]

$$P_{\mathrm{Z}}(X) = \frac{9Z!(Z+1)^6}{X^6(Z+6)!}\left[\frac{1}{2} + \frac{1}{2}\left(\frac{Z+2}{Z+1}\right)X^2 + \left[G(2X)^{(1/2)(Z+1)}Q(X)\right]\right] \tag{4.19}$$

with

$$X = qR \tag{4.20}$$

$$G(y) = \frac{(Z+1)^2}{(Z+1)^2 + y^2} \tag{4.21}$$

$$\begin{aligned} Q(X) = &-\frac{1}{2}\cos\left[(Z+1)F(2X)\right] - XG^{1/2}(2X)\sin\left[(Z+2)F(2X)\right] \\ &+ \frac{1}{2}X^2\left(\frac{Z+2}{Z+1}\right)G(2X)\cos\left[(Z+3)F(2X)\right] \end{aligned} \tag{4.22}$$

$$F(y) = \arctan \frac{y}{Z+1} \quad . \tag{4.23}$$

Figure 4.4 shows the form factors calculated for spherical particles with a mean radius $\overline{R} = 100$ nm for different dispersities. The extrema are less pronounced with increasing dispersity.

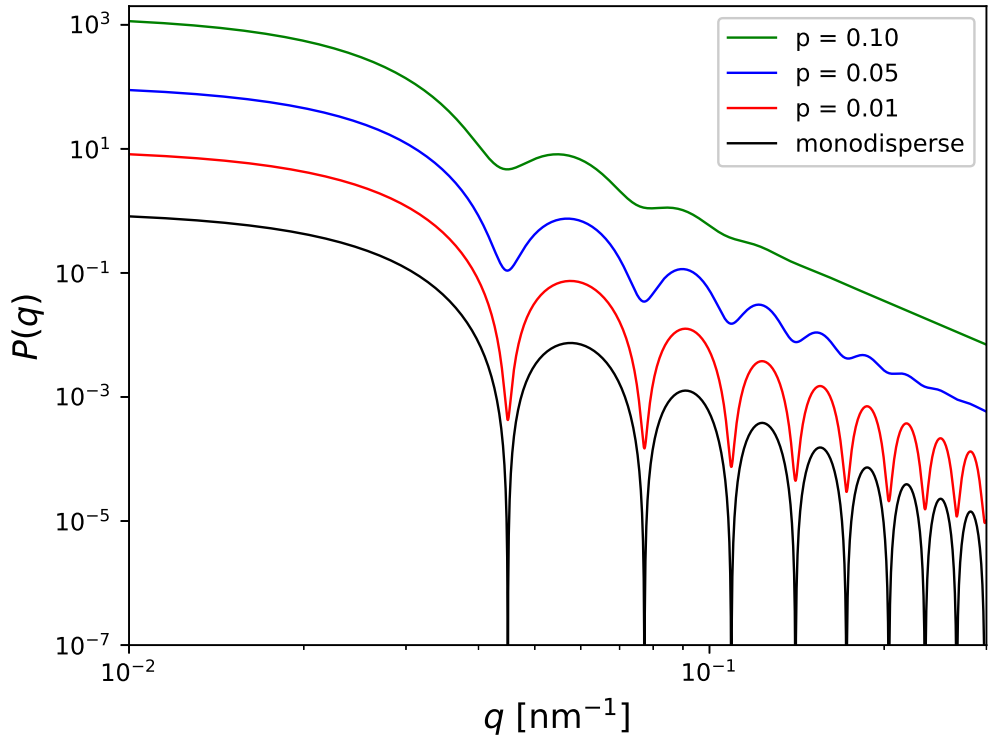

Figure 4.4: Calculated form factor of monodisperse and disperse spherical particles with mean radius $\overline{R} = 100$ nm. The disperse from factors are scaled by powers of 10 for better visibility.

4.2.3 Structure Factor

In concentrated particle systems the scattering intensity is additionally influenced by the inter-particle interaction and is taken into account by the static structure factor $S(q)$. For diluted, non-interacting particles $S(q) \approx 1$. For spherical particles with a narrow size distribution $I(q)$ can be factorized as[46,53]

$$I(q) = NV^2 \Delta\rho^2 P(q) S(q) \quad . \tag{4.24}$$

The structure factor can be calculated by

$$S(q) = 1 + 4\pi\rho_{\mathrm{N}} \int_0^\infty (g(r) - 1) \frac{\sin(qr)}{qr} r^2 \mathrm{d}r \tag{4.25}$$

with ρ_{N} the number density of particles in the dispersion. $g(r)$ is the pair-correlation function describing the probability of finding a particle in a volume

element $4\pi r^2 \mathrm{d}r$ at distance r from another particle. This function is dependent on the inter-particle interaction potential and therefore, by measuring the structure factor of a sample valuable information about the interaction potential can be extracted.

The calculation is, however, relatively complex. One can define a total correlation function

$$h(r) = g(r) - 1 \tag{4.26}$$

whose calculation involves many-body interactions. Ornstein and Zernike proposed to split the total correlation function into two parts which results in the so called Ornstein-Zernike integral equation [54]

$$h(r_{12}) = c(r_{12}) + \rho_{\mathrm{N}} \int c(r_{13}) h(r_{32}) \mathrm{d}\mathbf{r}_3 \quad . \tag{4.27}$$

Here, $c(r_{12})$ is the, a priori unknown, direct correlation function describing the portion of the structure resulting from the pair-potential between two particles 1 and 2. Since the system consists of N particles also indirect interactions between the two particles caused by the influence of the remaining $N-2$ particles need to be taken into account which is achieved by the second part of the sum in equation (4.27).

Substituting $h(r_{32})$ in equation 4.27 results in an infite recursion, thus, to solve the equation so called closure relations must be introduced which approximate the direct correlation functions. The simplest approximation is

$$c(r) = -\frac{1}{k_{\mathrm{B}} T} U(r) \tag{4.28}$$

where k_{B} is Boltzmann's constant, T the absolute temperature, and $U(r)$ the pair-potential of the particles. This approach is called the mean spherical approximation (MSA) [55]. The MSA yields good results for highly concentrated dispersions with short-range interaction [56] but fails to predict structures for diluted dispersions and highly charged particles.

As a consequence more elaborate closure conditions have been investigated. Some of the widely used conditions are the rescaled mean spherical approximation (RMSA) [57], the hypernetted chain (HNC) [58] and the Percus-Yevick (PY) approximation [59].

In the framework of this thesis the Percus-Yevick approximation will be used since it provides sufficient results for short-ranged repulsive potentials, like the hard-sphere potential, and also for a variety of different concentrations. The biggest advantage, however, is the existence of analytical solutions for the hard-sphere potential [60] using the Percus-Yevick approximation. The closure relation for the Percus-Yevick approximation is

$$c(r) = g(r) \left[1 - \exp\left(-\frac{U(r)}{k_{\mathrm{B}} T} \right) \right] \quad . \tag{4.29}$$

Once the direct correlation is known, the structure factor can be calculated by

$$S(q) = \frac{1}{1 - \rho_{\mathrm{N}} \hat{c}(q)} \tag{4.30}$$

where $\hat{c}(q)$ is the Fourier transform of $c(r)$. Figure 4.5 shows the calculated structure factor for monodisperse hard spheres of radius $r = 100$ nm and different volume fractions ϕ.

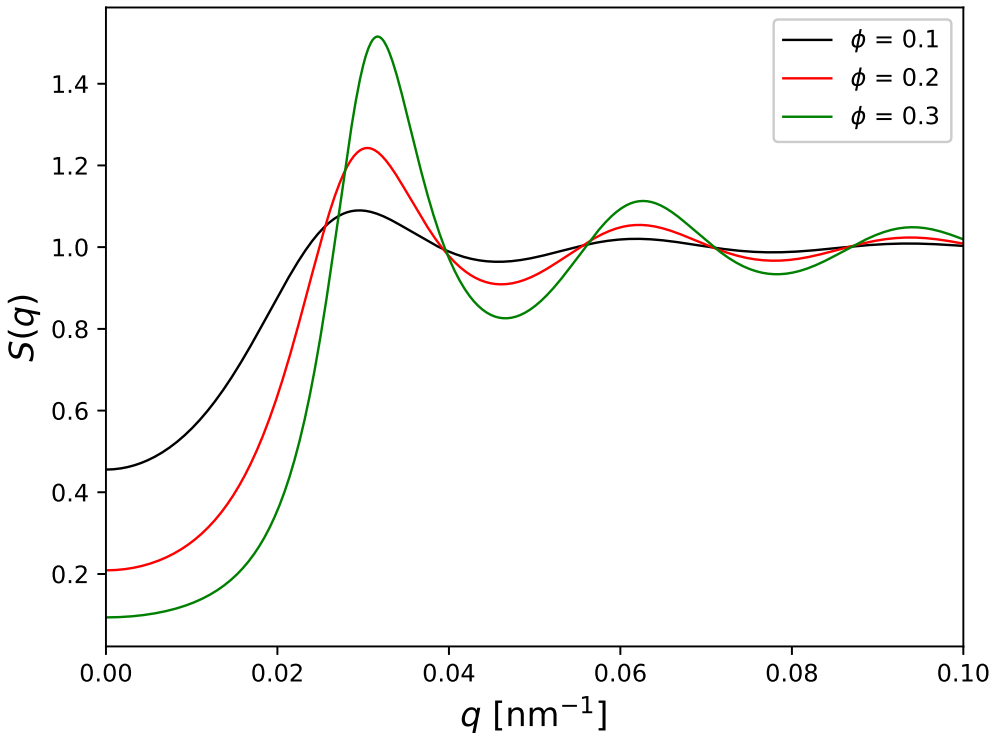

Figure 4.5: Calculated structure factor of monodisperse particles with radius $R = 100$ nm and different volume fractions ϕ.

The structure factor reaches a maximum and afterwards oscillates with decreasing amplitude. This behavior is typical for systems with a liquid-like structure, i.e. short-range order and long-range disorder. In the region of high values of q the structure factor approaches unity. Conversely, in the limit of $q \to 0$ the structure factor reaches a value of

$$\lim_{q \to 0} S(q) = \rho_{\mathrm{N}} k_{\mathrm{B}} T \kappa_{\mathrm{T}} \tag{4.31}$$

with κ_{T} beeing the isothermal compressibility.

4.3 X-ray Cross-Correlation Analysis

In 1977 Kam proposed the idea of using angular intensity correlations in scattering experiments to determine the structure of single particles in dilute solutions[61]. Commonly, the scattering pattern resulting from small angle scattering

experiments displays the orientational average of the dissovled particles. However, if the scattering intensity is recorded with a time resolution shorter than the reorientation time of the particle, it is possible to retrieve additional structural information beyond the ones routinely extracted from the radial intensity distribution.

When a coherent light beam impinges on a disordered sample it gives rise to a random scattering signal in the far field, a so called "speckle pattern". This pattern is the superposition of scattered waves from each individual scatterer and therefore encodes the instantaneous spatial arrangement of particles inside the scattering volume.

With the advancements made in the development of x-ray sources, such as third-generation synchrotrons and free-electron lasers, it became feasible to apply the angular cross-correlation approach to x-ray experiments. The work of Wochner et al.[16,17] showed that the x-ray cross-correlation analysis (XCCA) can be used to investigate hidden local symmetries in disordered matter. It was demonstrated that XCCA can reveal local structures with rotational symmetry in dispersions of non-crystalline PMMA spheres.

Following this work, multiple theory and simulation studies were performed to demonstrate the possibilities of this technique[62–66]. In recent experimental studies, XCCA was applied to investigate the local structure of e. g., colloidal nanocrystals[67], colloidal thin films[68–71], liquid crystals[72,73] and in situ self-assembled nanocrystals[74,75]. In addition to that several experiments were carried out in an effort to retrieve the structure of single particles in solution[76–79].

In the following part, the mathematical background of the cross-correlation analysis will be described. Figure 4.6 shows a scattering pattern of a SAXS experiment overlayed with the schematic of the principle geometry used for XCCA.

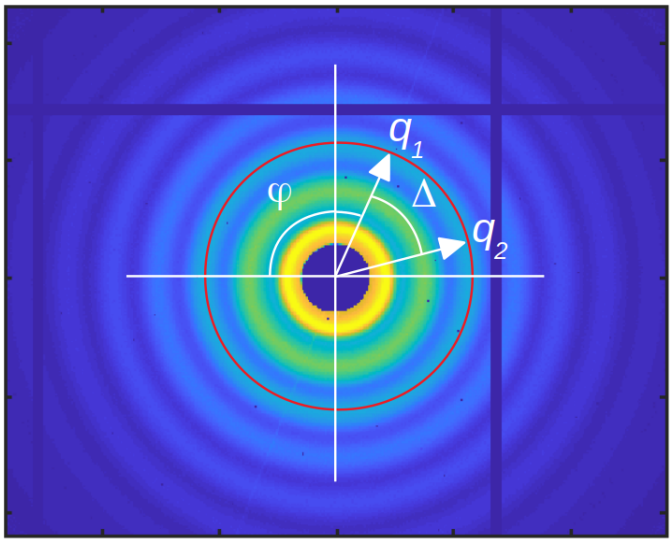

Figure 4.6: Scattering pattern in SAXS geometry showing the schematic of the geometry used in x-ray cross-correlation analysis. Two scattering intensity signals at scattering vectors $\mathbf{q}_1$ and $\mathbf{q}_1$ separated by an angle Δ are correlated over the azimuthal angle φ.

In the framework of this thesis, cross-correlation functions are considered for scattering vectors with equal magnitudes

$$q = |\mathbf{q}_1| = |\mathbf{q}_2| \quad . \tag{4.32}$$

The cross-correlation function $C(q, \Delta)$ is calculated by correlating the scattering intensities at two scattering vectors separated by an angle Δ

$$C(q, \Delta) = \frac{\langle I(q, \varphi) I(q, \varphi + \Delta) \rangle_\varphi - \langle I(q, \varphi) \rangle_\varphi^2}{\langle I(q, \varphi) \rangle_\varphi^2} \quad , \tag{4.33}$$

where φ is the azimuthal angle and $\langle \dots \rangle_\varphi$ denotes an azimuthal average. The cross-correlation function can be expressed by a Fourier series

$$C(q, \Delta) = \sum_{l=-\infty}^{\infty} C_l(q) \exp(il\Delta) \tag{4.34}$$

with the C_l being the lth Fourier coefficient of the cross-correlation function. The Fourier coefficients may be calculated using the inverse Fourier transform

$$C_l(q) = \frac{1}{2\pi} \int_0^{2\pi} C(q, \Delta) \exp(-il\Delta) \, \mathrm{d}\Delta \quad . \tag{4.35}$$

By normalizing the intensity

$$\hat{I}(q, \varphi) = \frac{I(q, \varphi) - \langle I(q, \varphi) \rangle_\varphi}{\langle I(q, \varphi) \rangle_\varphi} \tag{4.36}$$

the Fourier coefficients are related to the intensity via the Wiener-Khinchin theorem [80,81]

$$C_l(q) = |\hat{I}_l(q)|^2 \quad , \tag{4.37}$$

where $\hat{I}_l$ is the lth Fourier coefficient of the angular intensity distribution. The magnitude of the Fourier coefficients is a measure of the local l-fold symmetry of the scattering pattern and, thus, of the local order of the sample in the illuminated scattering volume. For example, a local hexagonal order is indicated by an increase of the 6th Fourier coefficient and, possibly, higher order multiples it.

4.4 Dynamic Light Scattering

In addition to the structural information which can be obtained by the techniques discussed above dynamic properties of a sample can be investigated using dynamic light scattering (DLS) exploiting visible light as well as x-ray photon correlation spectroscopy (XPCS) utilizing light in the x-ray regime. Both techniques share the same underlying principles which will be described in this section.

As described in section 4.3 a disordered sample illuminated by a coherent light beam gives rise to a speckle pattern. When observed over time, the particle

movement causes a fluctuation of the pattern, and thus, of intensity recorded by a detector. The noise-like intensity signal can be analyzed in terms of the second order intensity auto-correlation function

$$g_2(\mathbf{q},\tau) = \frac{\langle I(\mathbf{q},t)I(\mathbf{q},t+\tau)\rangle_t}{\langle I(\mathbf{q},t)\rangle_t^2} \tag{4.38}$$

where τ is the delay time and $\langle \dots \rangle_t$ denotes the temporal average. In the limit of short delay times the signal is fully correlated resulting in

$$\lim_{\tau\to 0}\langle I(\mathbf{q},t)I(\mathbf{q},t+\tau)\rangle_t = \langle I^2(\mathbf{q},t)\rangle_t \quad . \tag{4.39}$$

In case of the other extreme, for sufficiently long delay times the two signals become completely uncorrelated, and thus

$$\lim_{\tau\to\infty}\langle I(\mathbf{q},t)I(\mathbf{q},t+\tau)\rangle_t = \langle I(\mathbf{q},t)\rangle_t\langle I(\mathbf{q},t+\tau)\rangle_t = \langle I(\mathbf{q},t)\rangle_t^2 \quad . \tag{4.40}$$

The corresponding field auto-correlation function, often also called the intermediate scattering function, is defined as

$$g_1(\mathbf{q},\tau) = f(\mathbf{q},\tau) = \frac{\langle E(\mathbf{q},t)E^*(\mathbf{q},t+\tau)\rangle_\mathrm{e}}{\langle E(\mathbf{q},t)E^*(\mathbf{q},t)\rangle_\mathrm{e}} \tag{4.41}$$

with $\langle \dots \rangle_\mathrm{e}$ expressing the ensemble average and the intermediate scattering function

$$f(\mathbf{q},\tau) = \frac{S(\mathbf{q},\tau)}{S(\mathbf{q},0)} \quad . \tag{4.42}$$

Here, $S(\mathbf{q},0) = S(\mathbf{q})$ is the static structure factor which was already discussed in section 4.2.3. $S(\mathbf{q},\tau)$ is called the dynamic structure factor. In the case of N identical particles it can be defined as

$$S(\mathbf{q},\tau) = \frac{1}{N}\sum_{i=1}^{N}\sum_{j=1}^{N}\langle \exp\left[i\mathbf{q}\left(\mathbf{r}_i(t) - \mathbf{r}_j(t+\tau)\right)\right]\rangle_\mathrm{e} \quad . \tag{4.43}$$

In an ergodic system, e.g. disordered or liquid-like ordered, diffusive nanoparticles dispersed in a medium which are investigated in this work, the time-averaged intensity-correlation function can be connected to the ensemble-averaged field-correlation function via the Siegert relation

$$g_2(\mathbf{q},\tau) = 1 + \beta(\mathbf{q})g_1^2(\mathbf{q},\tau) \quad . \tag{4.44}$$

β is the speckle contrast and is a correction factor dependent on the coherence properties of the light source and the scattering geometry. Dynamic light scattering experiments commonly exploit laser sources which can be considered fully coherent within the scope of the experiment and hence $\beta = 1$.

Monodisperse particles undergoing Brownian motion can usually be described with a single exponential decay

$$g_1(\mathbf{q},\tau) = \exp\left(-\Gamma(\mathbf{q})\tau\right) \tag{4.45}$$

where Γ is the relaxation rate. The inverse $\tau_c = 1/\Gamma$ is called the characteristic relaxation time and is the time period in which the initial value of g_1 has dropped by $1/e$. Combining equations (4.44) and (4.45) results in

$$g_2(\mathbf{q}, \tau) = 1 + \beta(\mathbf{q}) \exp\left(-2\Gamma(\mathbf{q})\tau\right) \quad . \tag{4.46}$$

The relaxation rate can be related to the diffusion coefficient D_0 by

$$\Gamma(\mathbf{q}) = D_0(\mathbf{q})q^2 \quad . \tag{4.47}$$

When considering diluted, spherical, and monodisperse particles dispersed in a continuous medium the diffusion coefficient is direction and distance independent and can be calculated using the Stokes-Einstein equation [82]

$$D_0 = \frac{k_\mathrm{B}T}{6\pi\eta R_\mathrm{H}} \quad . \tag{4.48}$$

η is the dynamic viscosity of the dispersion medium and R_H the hydrodynamic radius of the particles. Figure 4.7 shows an exemplary intensity auto-correlation function of diffusing particles in water. The g_2-function decays exponentially from a starting value of two to a final value of unity.

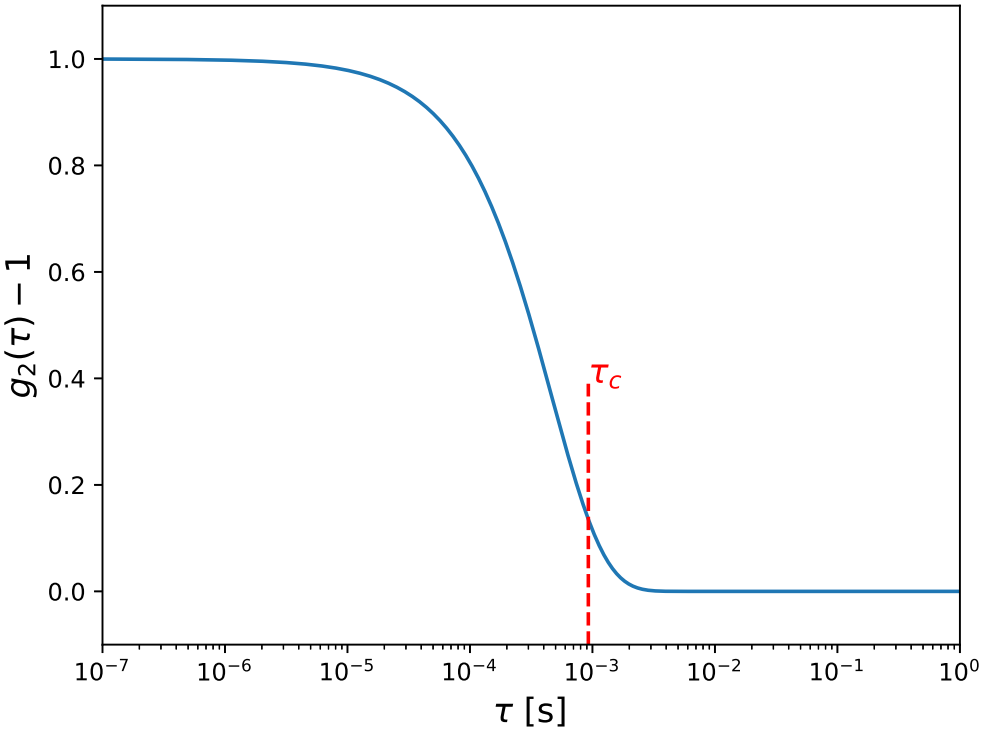

Figure 4.7: Calculated intensity auto-correlation function for diffusing nano particles dispersed in water with a hydrodynamic radius of 100 nm. The calculation assumes a wavelength of 532 nm (typical for a commonly used frequency-doubled Nd:YAG laser) and a scattering angle of 90°. τ_c marks the characteristic relaxation time.

As discussed before, in reality colloidal systems are usually not uniform in size. To take size dispersity into account, due to the distribution of diffusion coefficients the g_1-function must be expressed as an integral [83]

$$g_1(\tau) = \int_0^\infty G(\Gamma) \exp(-\Gamma\tau) \mathrm{d}\Gamma \tag{4.49}$$

with a normalized distribution of relaxation rates $G(\Gamma)$. However, the inversion of the experimentally obtained correlation function with the aim to retrieve information about the size distribution of a sample is considered an ill-posed problem [84]. Possible solutions to this problem are the cumulant method [83,85] as well as the CONTIN algorithm proposed by Provencher [86,87].

The cumulant method approximates the distribution by expressing the logarithm of the correlation function as a Taylor series

$$\log\left[g_1(\tau)\right] = \sum_{m=1}^{\infty} \frac{k_m}{m!}(-\tau)^{-1} \tag{4.50}$$

where k_m are called the cumulant coefficients. This method, however, assumes that only one class of particles is present which has a Gaussian size distribution.

In case of a multimodal, non-Gaussian particle size distribution, the CONTIN algorithm may give better results compared to the cumulant method. The algorithm treats the correlation function g_1 as a Laplace transform of the relaxation rate distribution $G(\Gamma)$ and uses Tikhonov regularization [88] to calculate the inverse Laplace transform.

5 Experiment

This chapter describes the details of the experimental work performed in the framework of this thesis. The preparation as well as the charaterization of the samples will be presented and the setup used for the combined rheology and small-angle x-ray scattering experiment will be shown. Finally, the measurement protocol which was used for parts of the rheology measurements are explained.

5.1 Sample

The samples used in this work consist of spherical silica nanoparticles coated with 3-trimethoxysilyl propyl methacrylate (TMSPM) that are dispersed in polyethylene glycol with a molar mass of 200 g/mol (PEG-200). The preparation as well as the characterization are described in this section.

5.1.1 Preparation

The nanoparticles were prepared using a modified Stöber synthesis [31] described in section 2.3 loosely adapted from Lee et al. [9] In the following, the synthesis of sample A with a radius of 150 nm and a volume fraction of 0.50 is described in detail. The other samples are prepared analogously.

A mixture of 6 ml aqueous ammonia solution (NH_4OH, 25 % m/m, Sigma-Aldrich), 32 g deionized water (H_2O), and 175 g anhydrous ethanol (EtOH, Sigma-Aldrich, Rotipuran) is put into a three-neck round-bottom flask and heated to a temperature of 50 °C. Under vigorous stirring 16 g tetraethyl orthosilicate (TEOS, Sigma-Aldrich) are added rapidly and the reaction is allowed to proceed for two hours. Then, 9 g of TMSPM (Sigma-Aldrich) are added and the reaction continues for another hour. After that, the nanoparticles are precipitated by centrifugation and washed with anhydrous ethanol three times. Finally, the particles are dispersed in PEG-200 (Sigma-Aldrich) such that the desired volume fraction is reached. The reaction conditions used for the different samples are shown in table 5.1.

Table 5.1: Reaction conditions used for the sample preparation.

Sample	A	B	C	D
NH_4OH [ml]	6	7	6.5	15
H_2O [g]	32	32	32	32
EtOH [g]	175	175	175	200
TEOS [g]	16.0092	15.9534	16.0052	5.0277
TMSPM [g]	9.0131	8.9916	9.0655	5.0221
Temperature [°C]	50	50	50	room temperature

5.1.2 Pre-Characterization

The samples are pre-characterized prior to the x-ray scattering experiments at the storage ring. The particle radius is measured using dynamic light scattering and the correct shape is confirmed by transmission electron microscopy. The succesful coating process is inferred in [9] as well as in this thesis, from the stability of the dispersions in PEG-200 and ethanol, and the lack of stability in water.

Dynamic Light Scattering

To pre-characterize the samples before the x-ray scattering experiment the radii are determined using dynamic light scattering (see section 4.4). A standard DLS experiment requires single scattering from the sample. Thus, the extraction of the radius by means of the Stokes-Einstein equation only works in case of non-interacting particles. Therefore, the samples are diluted such that the dispersions are visually transparent but still show scattering effects when light is shone on them. This makes sure that multiple scattering does not occur and, since the particles behave hard sphere-like, the sample is diluted enough to avoid particle interaction.

The radius was found to be independent of the dispersion medium. DLS measurements resulted in the same values for the particles dispersed in ethanol as well as in PEG-200. For the measurements of the samples A, B, and C, ethanol was used as a dispersion medium whereas sample D was measured in PEG-200.

DLS measurements are performed using a goniometer setup from LS Instruments (Switzerland) with a laser of wavelength 660 nm. The diluted samples are measured at scattering angles between 50° and 100° in steps of 5° at a temperature of 20 °C for 60 s each. The resulting intensity auto-correlation functions $g_2(\tau)$ are fitted using a single exponential function (see equation (4.46)). An example is shown in figure 5.1.

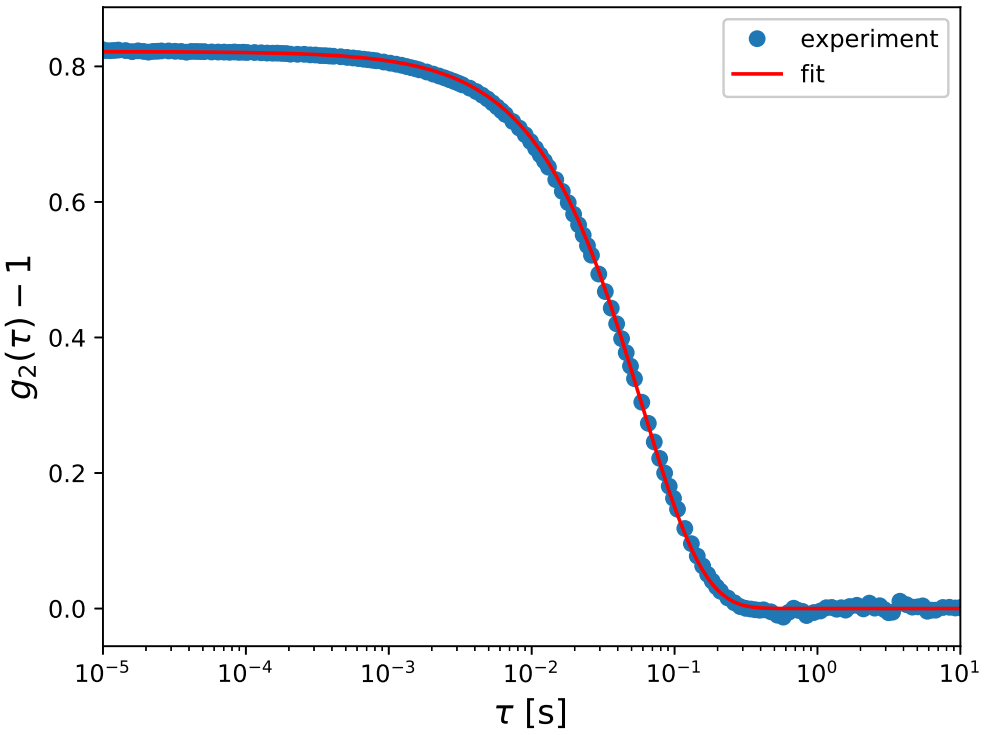

Figure 5.1: Intensity auto-correlation function of sample A in PEG-200 at an angle of 90°. The blue circles show the measured data and the red line displays the single exponential fit.

From the fit of the intensity auto-correlation functions the relaxation rate Γ is extracted for each angle. Using the relation from equation (4.47) the diffusion coefficient D_0 can be extracted. Therefore, the scattering angle is converted into the scattering vector q using equation (4.4). Afterwards, Γ is plotted against q^2 and fitted with a linear function, the slope of which is the diffusion coefficient. An example is shown in figure 5.2.

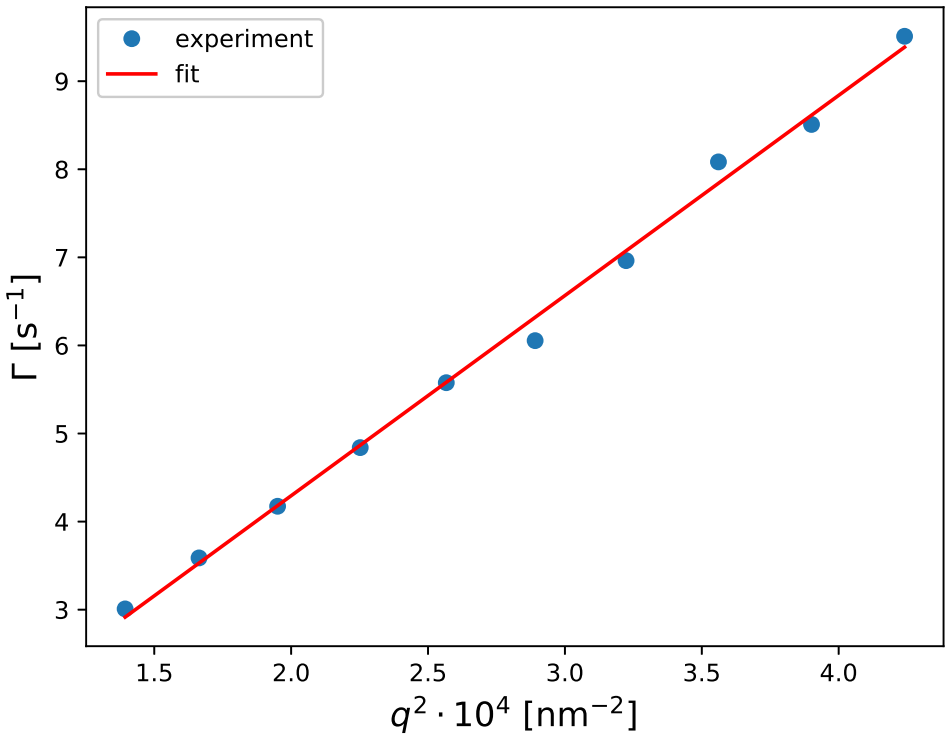

Figure 5.2: Relaxation rates Γ extracted from the exponential fits of the intensity auto-correlation functions plottet against the square of the scattering vector q^2. The blue circles show the data points and the red line displays the linear fit.

In the last step, the hydrodynamic radius of the particles is calculated from the diffusion coefficient using the Stokes-Einstein-equation (4.48). It is important to note, that the calculated radii are average values. The procedure described above does not take into account a size distribution but treats the particles as monodisperse. The results of the DLS analyses are shown in table 5.2.

Table 5.2: Diffusion coefficients and radii of the samples obtained from the DLS analysis. The errors are the errors of the fit and not to be confused with dispersities.

Sample	A	B	C	D
R_H [nm]	157 (±4)	141 (±4)	129 (±8)	80 (±1)
$D_0 \cdot 10^{14}$ [m^2 s^{-1}]	2.27 (±0.05)	2.53 (±0.07)	2.78 (±0.15)	213 (±4.3)
Dispersion medium	PEG-200	PEG-200	PEG-200	ethanol

Transmission Electron Microscopy

The analysis of the dynamic light scattering experiments, as described in the section above, only results in average values of the particles' hydrodynamic radii. One important feature that is not investigated by that technique is the shape of the particles. To confirm the spherical shape of the particles the samples are probed by transmission electron microscopy (TEM).

Therefore, the samples were diluted with ethanol and a droplet of the dispersion is put onto a copper grid. The sample is then dried in air. An example of the TEM measurements is displayed for sample A in figure 5.3.

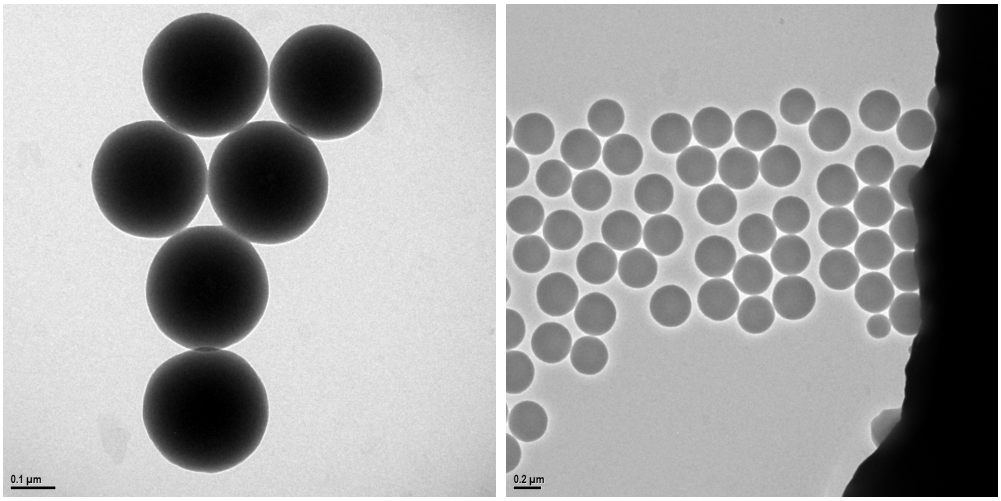

Figure 5.3: Transmission electron micrographs of sample A. The images confirm the spherical shape and also show a a relatively uniform size distribution. The scale bar in the left image represents 100 nm and the one in the right image 200 nm. The average radius of the particles as calculated from these images is 152 nm.

The images show that the samples are spherical in shape and comparably monodisperse in size. It is important to note that the radii extracted from the TEM-measurements are usually smaller compared to the DLS measurements. This is the case because DLS measures a hydrodynamic radius of the particles, i.e. the radius of the particles' silica core plus the polyacrylate coating layer as well as adsorbed water and ions. As a result, the hydrodynamic radius is always larger than the radius of the isolated, dried, particle.

As mentioned above, the TEM images were taken to confirm the spherical shape of the particles. The average radius of the particles of sample A as calculated from the images in figure 5.3 is 152 nm which is in a reasonable range compared to the reasults obtained from DLS. However, the images show only a few particles each so that it is not feasible to determine a size distribution of the sample because of the non-sufficent statistics.

5.2 Experiment setup

The experiment was carried out at the coherence beamline P10 at the storage ring PETRA III at DESY in Hamburg. The samples are investigated using the unique vertical rheoSAXS setup combining a modified Haake Mars 3 rheometer with a coherent x-ray beam and a detector in SAXS geometry [89]. A schematic of the setup as well as a photograph are displayed in figure 5.4.

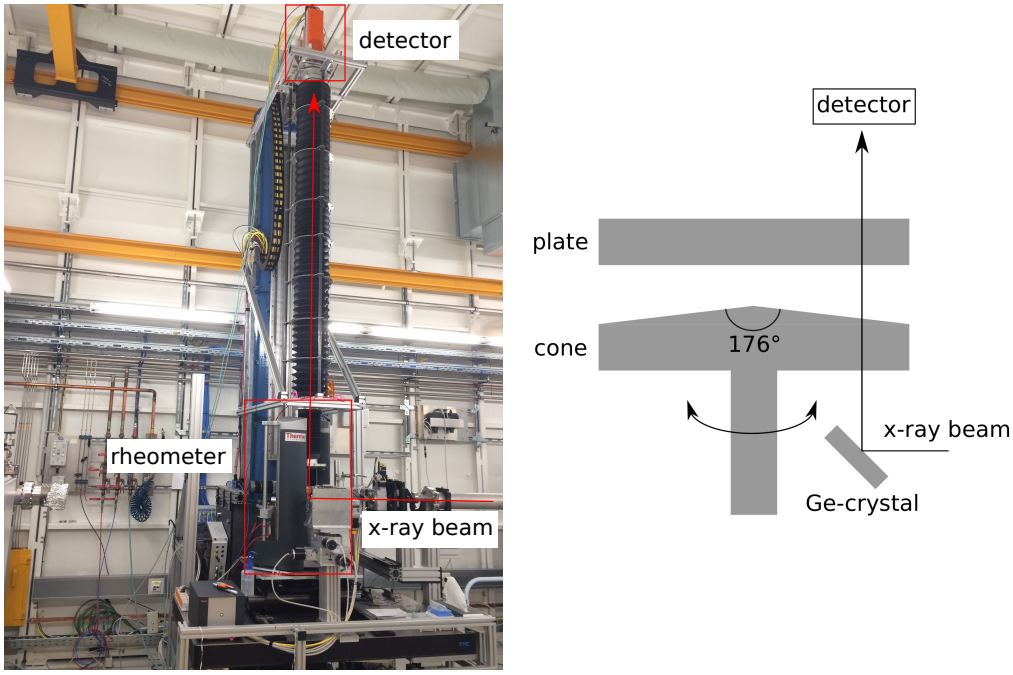

Figure 5.4: Vertical rheoSAXS setup at the coherence beamline P10 at PETRA III. The x-ray beam is reflected upwards by the 333-reflection of a Germanium single crystal, passes the rheometer setup, and is detected with a LAMBDA 750K detector. Left: photograph; right: schematic representation.

The parameters used during the experiment are shown in table 5.3. The x-ray beam generated by the undulator approaches the end station of the beamline horizontally. It is reflected upwards by 90° using the 333-reflection of a Germanium single crystal.

The cone of the rheometer setup has milled windows for the x-ray beam to pass through and its surface is covered with Kapton to contain the sample. The plate has a drilled hole which is fitted with a diamond window and the surface is covered with Kapton, as well.

After passing through the rheometer, the primary photon beam is absorbed by a beamstop and the scattered photons are detected by a photon counting detector. In this experiment the LAMBDA 750K (Large Area Medipix3-Based Detector Array) detector was used [90]. It consists of 1556×516 pixels with a pixel size of 50×50µm^2. Images are detected with exposure times between 0.01 s and 1 s.

Table 5.3: Experiment parameters used at beamline P10.

Photon energy	8.052 keV
Detector	LAMBDA 750K
Pixel size	55×55 µm^2
Sample-detector distance	2.99 m
Beam size	15×15 µm^2
Rheometer	modified Haake MARS 3

The rheological measurements are performed in cone-plate geometry using a cone with an opening angle of 176°. Oscillatory shear was used with a frequency of 0.1 Hz. The amplitude is varied throughout the experiment. It is important to note that the rheometer and the detector are not synchronized, so that the rheological measurements need to be synchronized with the x-ray measurements after the experiment.

5.3 X-ray Characterization

In addition to the pre-characterization mentioned in the sections above basic characteristic parameters of the samples at rest were measured using small-angle x-ray scattering. These measurements were performed at beamline P10 of PETRA III using the setup described in section 5.2.

5.3.1 Form factor

The radii and dispersities of the samples have been determined by measuring the form factors. As described before, this procedure is more accurate than the dynamic light scattering approach. On the one hand, in DLS a monodisperse system was assumed and on the other hand, the measured radius is a hydrodynamic radius.

For the form factor measurements the samples were diluted enough such that no structure factor could be observed. In case of the samples used here, the dilution was approximately 1:1000 with PEG-200 resulting in a volume fraction of around 0.05 %.

The samples were measured with an exposure time of one second. The two-dimensional intensity patterns are integrated azimuthally so that the intensity is obtained as a function of the modulus of the scattering vector. The resulting data points were then fitted assuming hard sphere particles with a Schulz-Zimm size distribution (see section 4.2.2). The radius can be directly extracted from the corresponding fit whereas the dispersity is calculated from the Z-parameter of the Schulz-Zimm distribution using equation (4.17). As an example, the result of sample A is shown in figure 5.5.

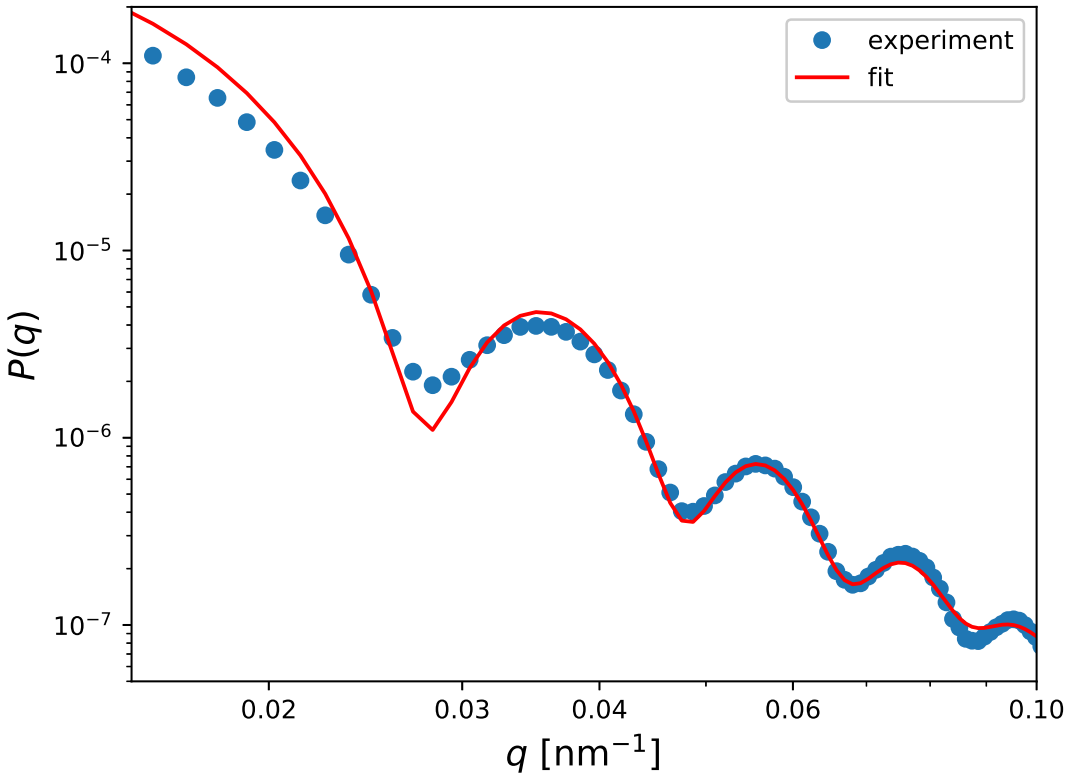

Figure 5.5: Form factor of sample A. The blue circles represent the data collected by SAXS and the red line the fit. This particular fit results in a radius of 160 nm and a dispersity of 0.062.

The parameters extracted from the form factor measurements of all samples are summarized in table 5.4 at the end of the next section.

5.3.2 Structure factor

In the next step the structure factor was measured. The measurements were carried out in SAXS geometry, as well, utilizing the concentrated samples used in the rheology experiments afterwards. A typical scattering pattern is shown for sample A in figure 5.6.

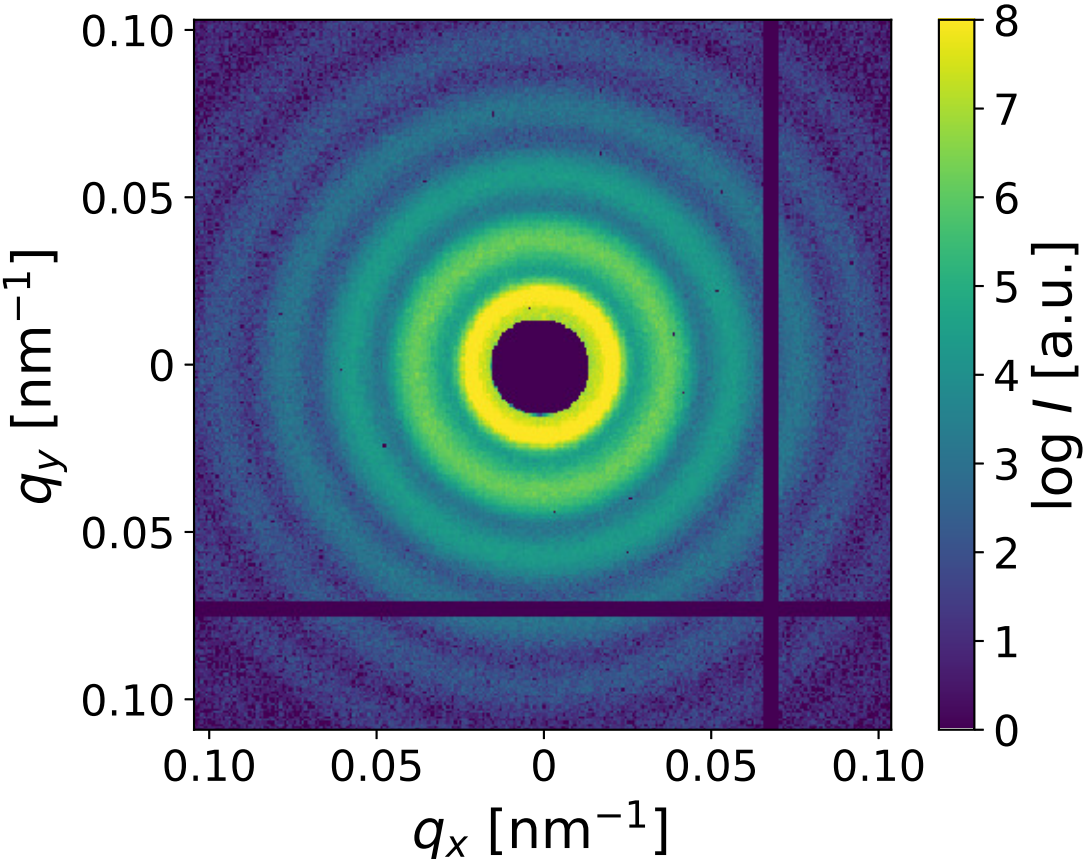

Figure 5.6: Scattering pattern of sample A with a volume fraction of 0.50 recorded with an exposure time of 0.1 s. The sample consists of liquid-like ordered, spherical nanoparticles resulting in the isotropic, annular scattering pattern.

Similar to the form factor determination, in the first step the scattering function is calculated from the two-dimensional scattering pattern by azimuthal integration. The scattering function of sample A is shown in figure 5.7. The scattered intensity of the sample oscillates around the form factor with decreasing amplitude at large scattering vectors. This behavior is typical for a liquid-like ordered sample.

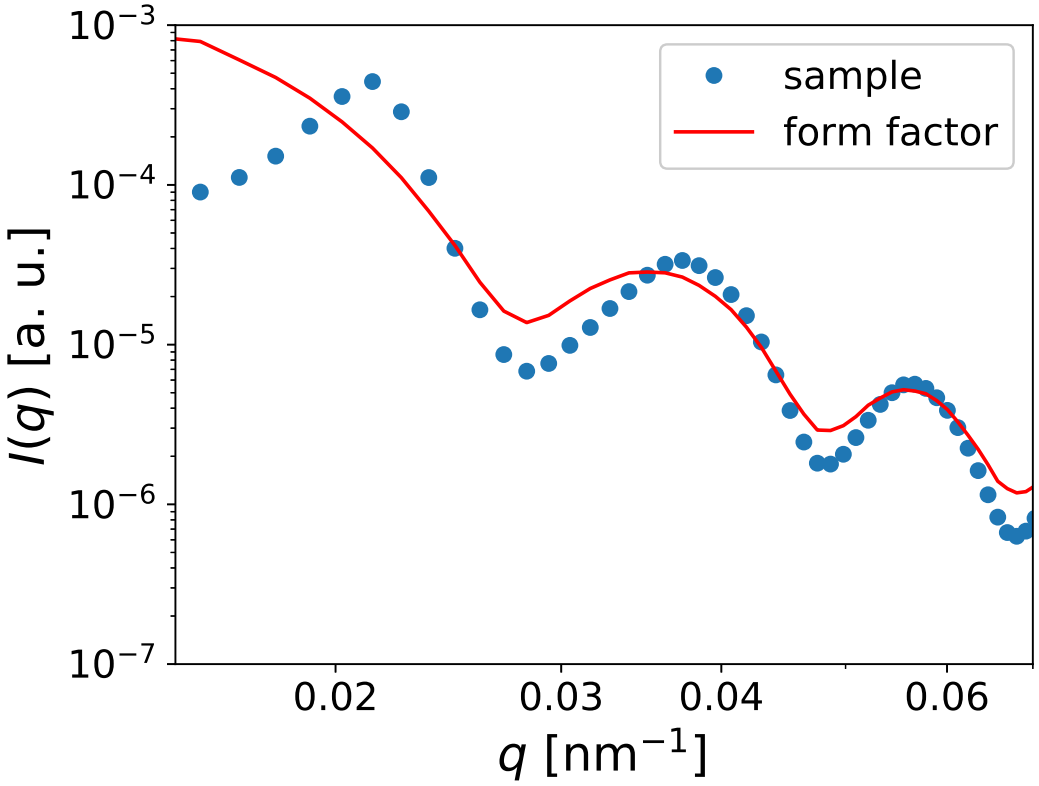

Figure 5.7: Scattering function of sample A (blue) and the corresponding form factor (red). The intensity of the sample oscillates around the form factor with decreasing amplitude at large scattering vectors.

Next, the structure factor is calculated using equation (4.24) by dividing the scattering function of the sample by its form factor. It is important to note, that the scattered intensity from the concentrated sample differs from the scattered intensity of the form factor since in the latter case the sample is highly diluted. Thus, when calculating the structure factor the form factor is scaled by a constant such that the resulting structure factor oscillates around a value of one. The resulting structure factor of the samples are shown in figures 5.8 and 5.9.

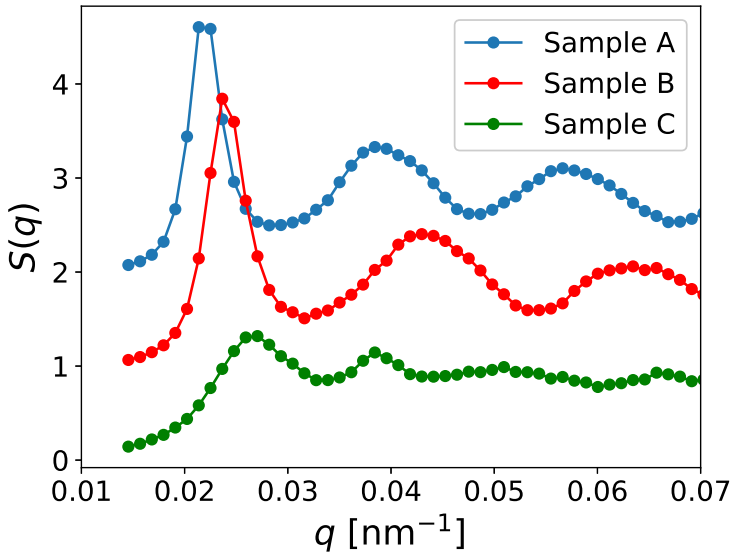

Figure 5.8: Structure factors of samples A, B, and C. The graph of sample B is shifted upwards by one and the one of sample A by two, respectively. The lines are a guide to the eye and do not represent measured values.

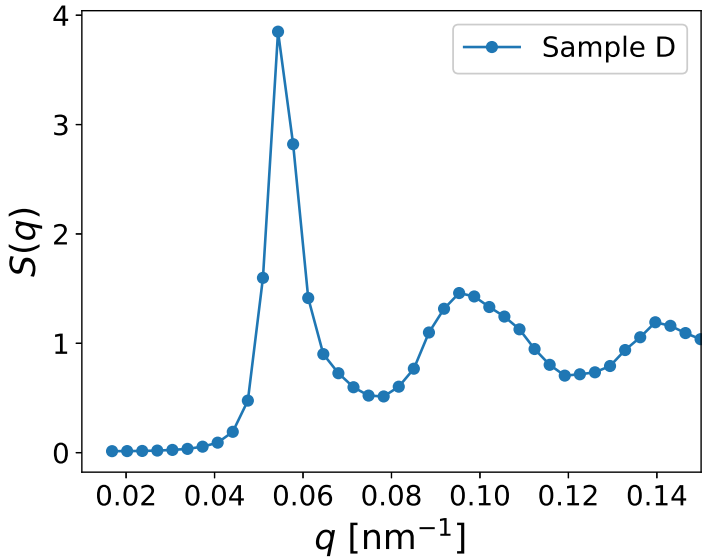

Figure 5.9: Structure factors of sample D. Because of the smaller radius of this sample, the structure factor maximum is shifted to higher values of q. Therefore, this graph is shown separately. The lines are a guide to the eye and do not represent measured values.

In a last step, the measured structure factor is compared to one calculated using the Percus-Yevick approximation to extract information about the volume fraction of the sample. Since this approach assumes monodisperse hard-sphere particles the Percus-Yevick structure factor is only an approximation. For the particle radius the radius determined by the form factor measurements is used.

The volume fraction is chosen such that the calculated structure factor is in good agreement with the first maximum of the measured data. Because of the approximative nature the calculated structure factor is more and more out of phase at larger scattering vectors. The comparison of the calculated and measured structure factor is shown for sample A in figure 5.10.

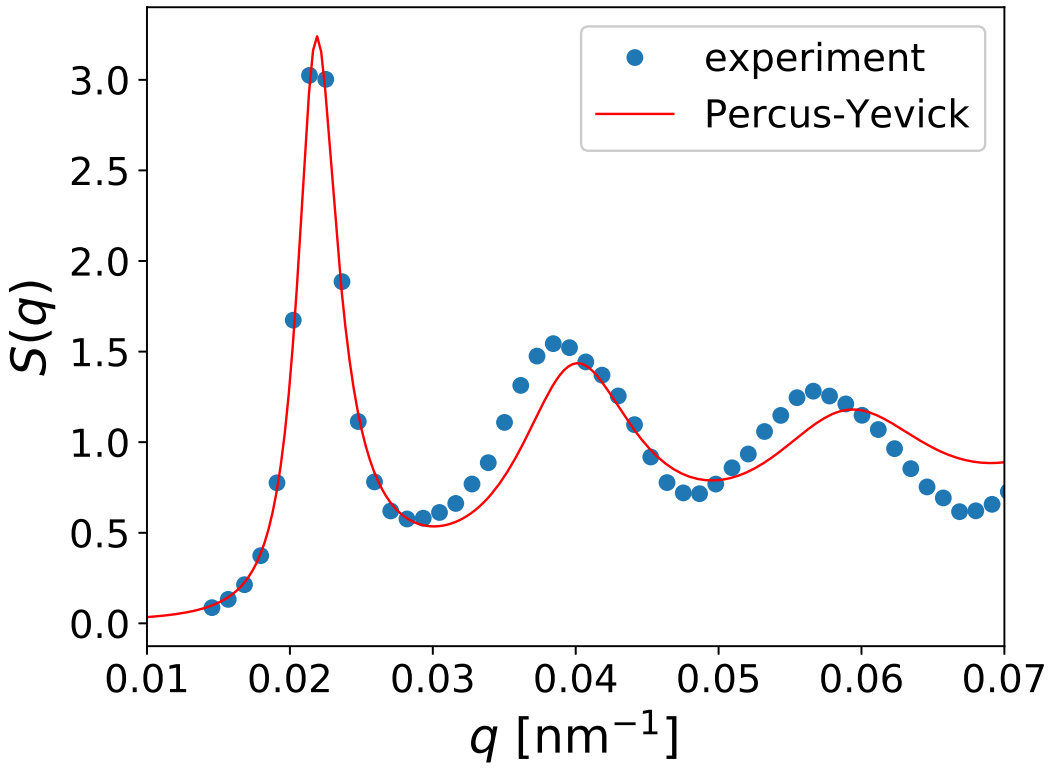

Figure 5.10: Measured (blue) and calculated (red) structure factor of sample A. The measured structure factor is obtained from small-angle x-ray scattering and the calculated one using the Percus-Yevick approximation [60]. As parameters for the calculated structure factor a radius of 160 nm and a volume fraction of 0.50 are used.

The volume fractions determined by this approach for all samples are shown in table 5.4.

Table 5.4: Characteristic parameters of the samples used in this work. The values are determined by small-angle x-ray scattering.

Sample	A	B	C	D
R [nm]	160 ±0.7	148 ±0.9	117 ±0.5	64 ±0.2
Z	261 ±26	168 ±19	261 ±31	200 ±13
p	0.062 ±0.003	0.077 ±0.004	0.062 ±0.004	0.071 ±0.002
ϕ	0.50	0.52	0.22	0.53

In summary, the synthesized particles have radii ranging from 64 nm to 160 nm and show dispersities below 8 % which can be considered as monodisperse. With

samples A, B, and D, most of the samples are prepared at volume fractions of around 50 %, while sample C is considerably lower concentrated at less than half the volume fraction of the other samples.

5.4 Standard Measurement Protocol

The main protocol used for the combined rheology and SAXS measurements is described in this section. In the beginning of the experiment, the cone is mounted to the rheometer and an internal inertia calibration is performed. As long as the same cone is used for the experiment the calibration does not need to be repeated.

Before measuring each sample all surfaces are cleaned with isopropyl alcohol and a lint-free wipe. Afterwards, the surfaces are dried and dusted using pressured air and an internal zero-point calibration is carried out, i. e. calibrating the motor settings in order to reach a contact between the cone and plate. Following the calibration, a volume of 450 µl of the sample is dispensed onto the cone and the gap between the cone and plate is set to a distance of 0.251 mm measured from tip of the cone. After preparing the rheometer and the beamline the x-ray scattering as well as the rheometer measurements are started simultaneously.

As mentioned previously, the rheometer is operated using oscillatory shear with a frequency of 0.1 Hz. The deformation amplitude is varied in the following way:

- The measurement begins with a waiting time of five seconds, i. e. an amplitude of $\gamma_0 = 0$.
- After that, the oscillation starts with an amplitude of $\gamma_0 = 0.01$ for five oscillation cycles which corresponds to a time period of 50 s in case of a frequency of 0.1 Hz.
- In the following, the amplitude is doubled after each consecutive 5 oscillation cycles until a final amplitude of 0.08 is reached.
- After measuring the cycles at 0.08, the process is repeated starting with an amplitude of 0.01, again. Like before, after each five oscillation cycles the amplitude is doubled, this time upto a final amplitude of 0.16, which is twice as high as the previous final amplitude.

This whole procedure, starting at 0.01, doubling the amplitude after 5 oscillations up to a final value which is twice as high as the one before, is repeated until a final amplitude of 2.56 is reached. For clarification, the program is summarized in table 5.5 and visualized in figure 5.11, as well.

Table 5.5: Amplitude settings used in the measurement protocol.

set of oscillations	amplitudes γ_0
first 5 seconds	0
1st	0.01, 0.02, 0.04, 0.08
2nd	0.01, 0.02, 0.04, 0.08, 0.16
3rd	0.01, 0.02, 0.04, 0.08, 0.16, 0.32
4th	0.01, ..., 0.64
5th	0.01, ..., 1.28
6th	0.01, ..., 2.56

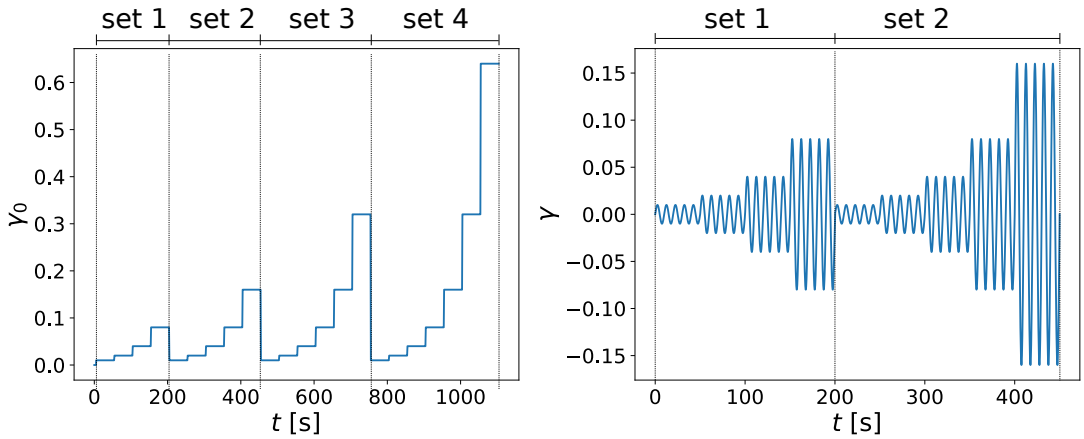

Figure 5.11: Visualization of the settings used in the measurement protocol. Left: Amplitude scheme of the experiment. Shown are the first 4 sets. In the standard experiment, 6 sets are performed until a final amplitude of 2.56 is reached. Right: Resulting deformations shown for the first two sets.

Figure 5.12 displays two oscillation cycles and visualizes the variation of the parameters over time. For the shear rate, the absolute value is chosen instead. While the cone of the rheometer alternates between clockwise and counter-clockwise rotation, which is indicated by the sign, the shear rate is independent of the direction. Note, that for every one oscillation cycle the shear rate shows two minima and maxima. The maximum shear rate for a given γ_0 can be calculated using equation (3.17) resulting in

$$\max(\dot{\gamma}) = \max[\gamma_0 \omega \cos(\omega t)] = \gamma_0 \omega = \gamma_0 \cdot 2\pi f \tag{5.1}$$

In case of the example shown in figure 5.12 with $\gamma_0 = 0.01$ and $f = 0.1$ Hz the maximum shear rate is $\dot{\gamma}_{\max} \approx 0.006\ \mathrm{s}^{-1}$.

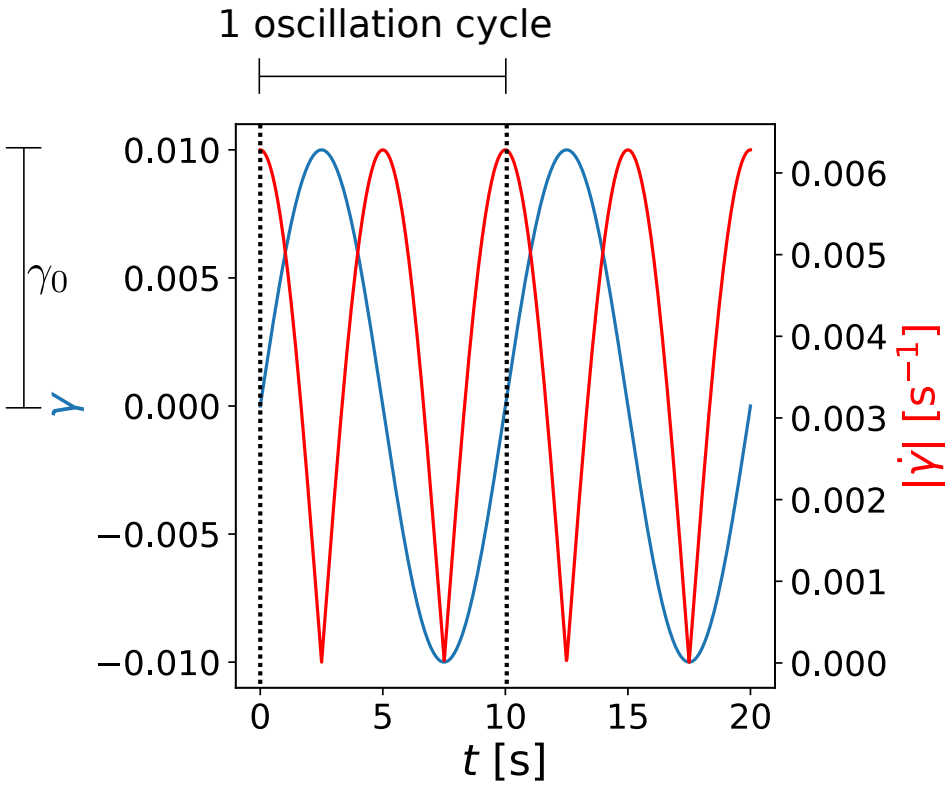

Figure 5.12: Illustration of the parameters during an oscillation cycle for $\gamma_0 = 0.01$. While the cone of the rheometer alternates between clockwise and counter-clockwise rotation, which is indicated by the sign, the shear rate is independent of the direction. Therefore, for every one oscillation cycle, the shear rate exhibits two maxima and minima.

The protocol described above is chosen because of mainly two reasons. Firstly, the behavior of each individual sample at high amplitudes, and, thus, high shear rates, is not known before the measurement. Shear thinning can lead to such low viscosities that the samples get ejected from the rheometer at the comparably high angular velocities reached at high amplitudes. This is the reason for the gradual increase of the final amplitude in each set. In this way, multiple sets can be measured even if an incident occurs at higher amplitudes.

Secondly, by repeating the whole measurement process starting from the lowest amplitude in each set, possible hysteresis effects can be probed. In addition, it can be investigated if the observed effects are only shear rate-dependent or also time-dependent.

6 Structure of Colloidal Systems Under Shear

In this chapter, the behavior of the samples under oscillatory shear is presented. The rheological properties are compared with the underlying structural changes which are measured in situ utilizing small-angle x-ray scattering. The samples show different behavior for different volume fractions and, hence, are discussed in different sections.

6.1 Sample at High Volume Fraction

In the first section the behavior of sample D is investigated. This sample consists of nanoparticles with a radius of 64 nm dispersed in PEG-200 with a volume fraction of 0.53. Figure 6.1 shows the scattering pattern of sample D at rest.

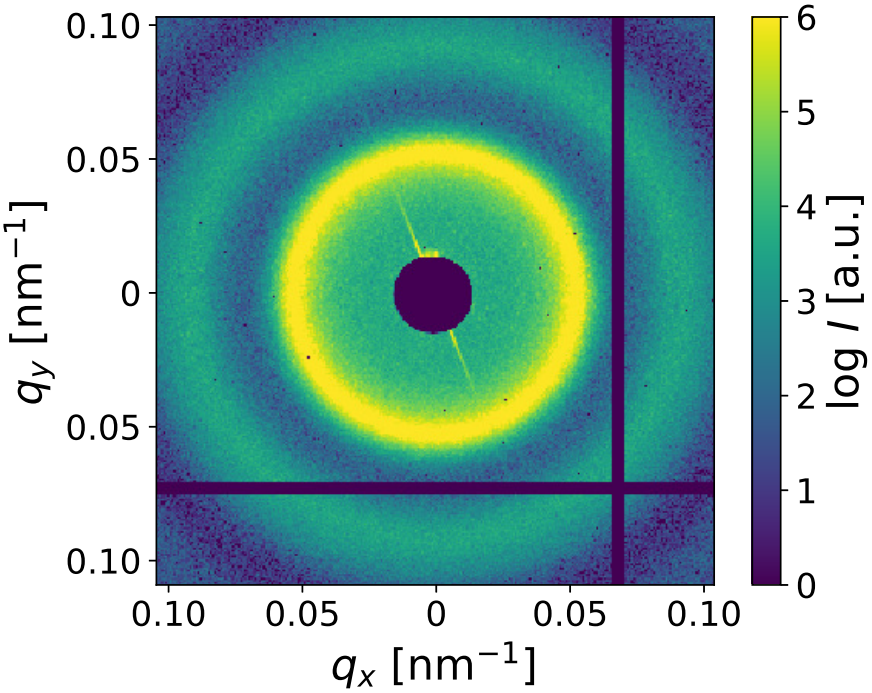

Figure 6.1: Scattering pattern of sample D at rest recorded with an exposure time of one second.

At rest, the sample exhibits the expected pattern of a liquid-like ordered sample and resembles the structure factor as shown in section 5.

For the rheological measurement of sample D the typical approach of a stress sweep is used. The sample is measured applying stresses between 0.01 Pa and 100 Pa which correspond to deformations between 10^{-5} and 0.75 that can be extracted as an average over the measurement time. For each stress value the sample is sheared for 200 seconds at 0.1 Hz and 2000 small-angle x-ray scattering patterns are recorded with an exposure time of 0.1 seconds. All measurements are performed with the same loading of the sample, i. e. no new sample was filled into the shear cell between different stresses. The SAXS patterns averaged over the whole measurements are shown in figure 6.2.

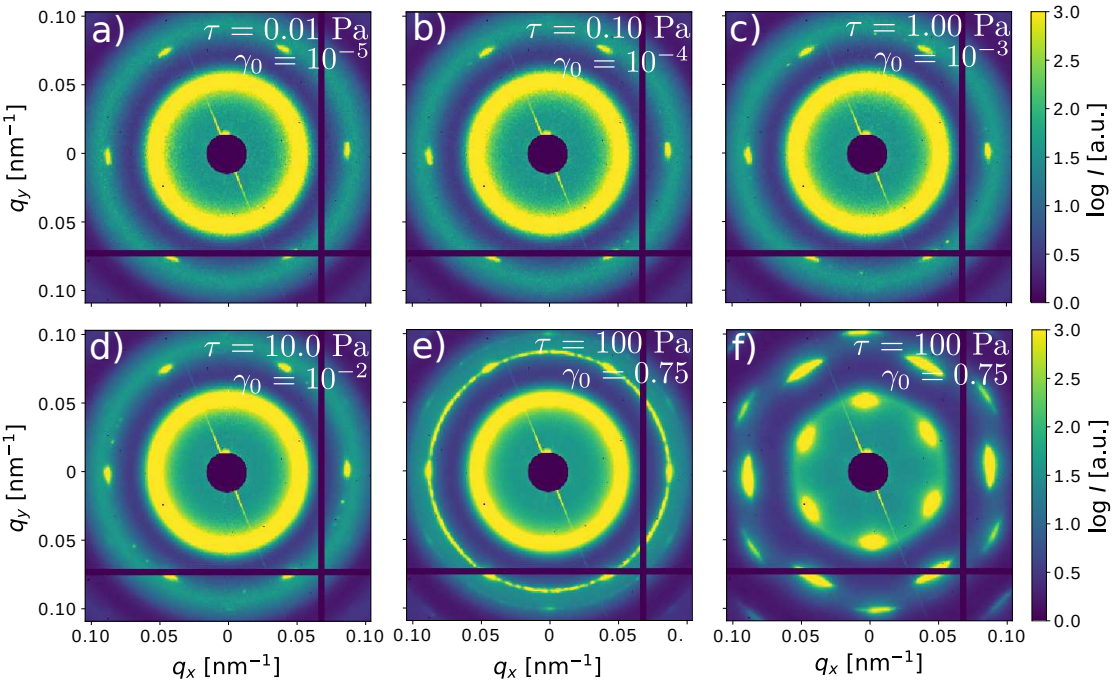

Figure 6.2: Scattering patterns of sample D averaged over the rheology measurements at different shear stresses with the same sample loading. Between the images e) and f) the cone of the rheometer was rotated by half a revolution at a shear rate of $\dot{\gamma} = 1$ s^{-1}.

The slightest rotation of the cone leads to structure formation in this particular sample. Due to the necessary preparation procedures before the start of the measurent, the sample is already preordered which is visible in figure 6.2 a). Bragg reflections with hexagonal symmetry are observable in the second intensity maximum from the beginning of the experiment. The Bragg reflections are visible continuously and are not apperaring and disappearing during the oscillation.

The scattering patterns look similar in images a) to c). This indicates, that the comparably small deformation amplitudes have no effect on the structure of the sample. Small changes in the form of additional Bragg reflections in the second intensity maximum become observable beginning from a deformation of $\gamma_0 = 0.01$, which is the lowest amplitude used in the measurements of samples A, B, and C discussed in the next section. During the measurement at $\tau = 100$ Pa a powder-like scattering pattern forms showing sharp rings at the same q where

the Bragg reflections were visible before.

In section 5.2 it was described that the cone of the rheometer setup has milled in windows for the x-ray beam to pass through. After the measurement shown in image e) the cone ended up in a position where one of the metal bridges blocked the x-ray beam path. In preparation for a measurement of the final structure the cone was rotated for half a revolution with a shear rate of $\dot{\gamma} = 1\ \mathrm{s}^{-1}$. As a consequence, the scattering pattern changed drastically and the result is shown in figure 6.3. Starting with this structure, another measurement is performed using the same conditions as the measurement before. The results are shown in figure 6.2 f).

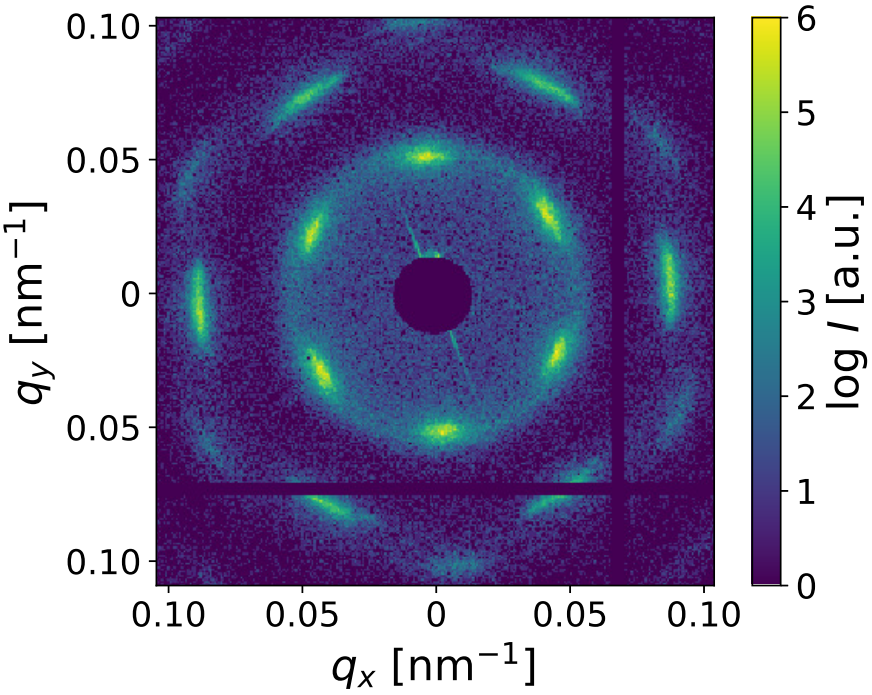

Figure 6.3: Scattering pattern of sample D at rest after the cone of the rheometer was rotated by half a revolution at a shear rate of $\dot{\gamma} = 1\ \mathrm{s}^{-1}$. The image is taken with an exposure time of 0.1 seconds.

Initially and in the case of low shear stress τ, Bragg reflections appear in the second intensity maximum of the sample. Therefore, a peak is visible in the second structure factor maximum $q = 0.086\ \mathrm{nm}^{-1}$ which is shown in figure 6.4. X-ray cross-correlation analysis is performed to reveal the distribution of the Fourier coefficients of the cross-correlation function at the scattering vector of the occuring Bragg reflections. The result is displayed exemplarily for the stress measurement of $\tau = 1.0$ Pa in figure 6.5. It is representative for the measurements with lower stress, as well. From the XCCA results it is evident that the Fourier coefficients which are multiples of six show the largest amplitudes. This is expected because of the six-fold symmetry of the scattering pattern. In the right image of figure 6.5 the most prominent Fourier coefficient C_6 is resolved as a function of time. At low amplitudes C_6 follows a noisy pattern. The sixth

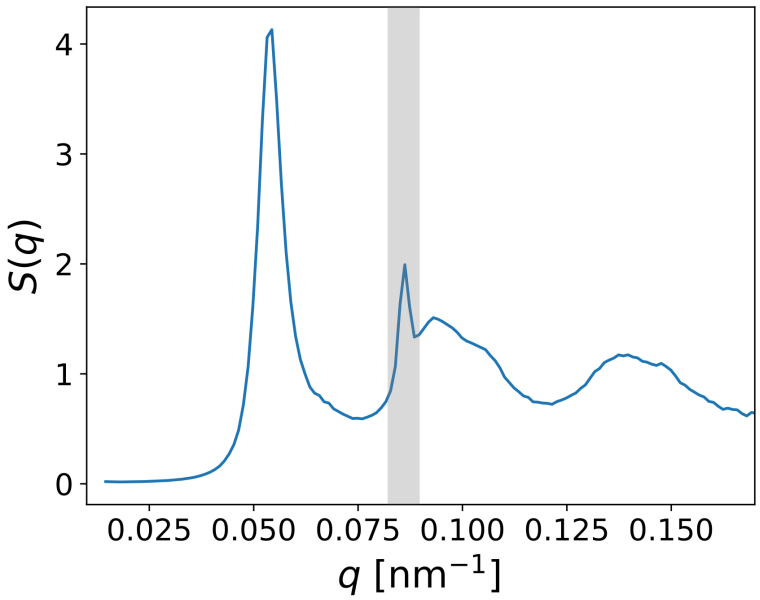

Figure 6.4: Structure factor of sample D calculated from the average of the first second of the rheology measurement at a stress of $\tau = 1.0$ Pa. A small peak is visible in the second maximum at $q = 0.086$ nm^{-1}.

Fourier coefficient fluctuates around a non-zero value, i. e. the six-fold symmetry is not changing over the course of the measurement.

During the measurement applying the highest shear stress of $\tau = 100$ Pa the formation of a powder-like scattering pattern is observed. Since figure 6.2 e) displays only the average pattern over the whole 200 seconds of the measurement, single scattering patterns at different points of the measurement are shown in figure 6.6.

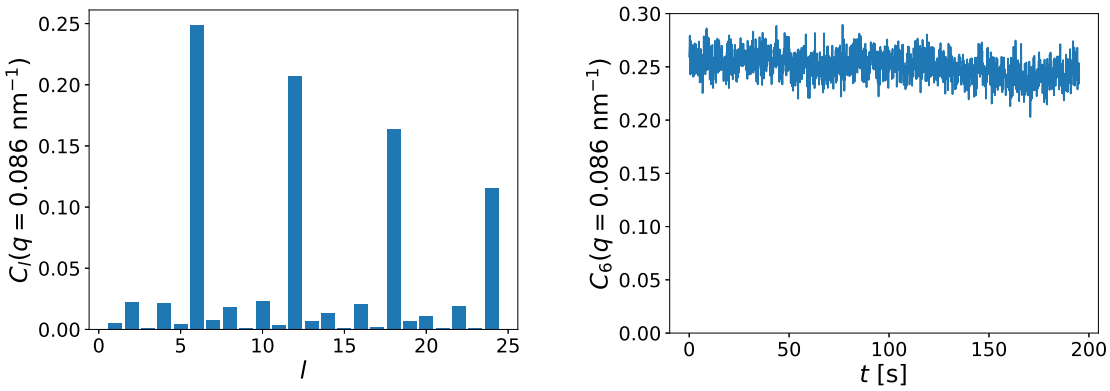

Figure 6.5: Left: Distribution of Fourier coefficients of the cross-correlation function averaged over the measurement at $\tau = 1.0$ Pa. Fourier coefficients which are multiples of six show the largest amplitudes; right: Sixth Fourier coefficient of the cross-correlation function of sample D at $\tau = 1.0$ Pa resolved over time.

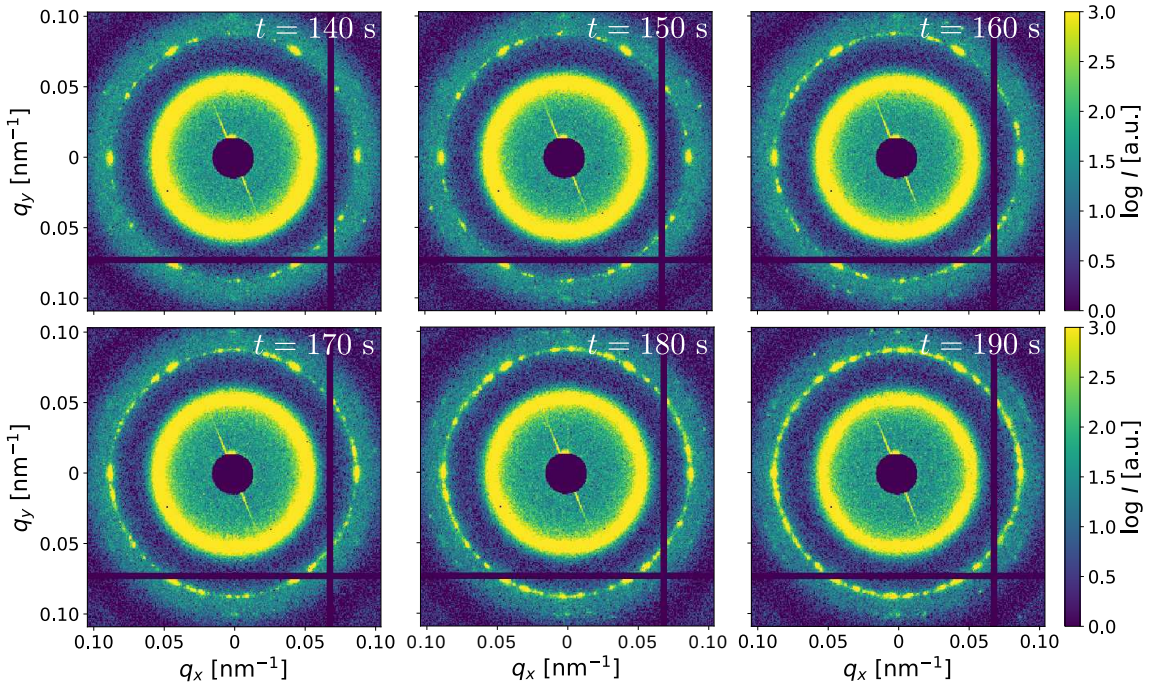

Figure 6.6: Single scattering patterns recorded at different time points of the shear experiment applaying a shear stress of $\tau = 100$ Pa. More and more Bragg reflections appear at the same scattering vector $q = 0.086$ nm^{-1} forming a powder-like scattering pattern. The first intensity maximum becomes narrower over time, as well.

It can be observed that over time additional Bragg reflections become visible at the same scattering vector of $q = 0.086$ nm^{-1} but rotated around the center of the pattern. Upon closer inspection, Bragg reflections can be observed also at larger scattering vectors at around $q = 0.10$ nm^{-1}. In figure 6.6, the visible section of the detector is quite small to enhance the visibility of the most intense Bragg reflections. The evolution of a larger section of the structure factor is illustrated in figure 6.7.

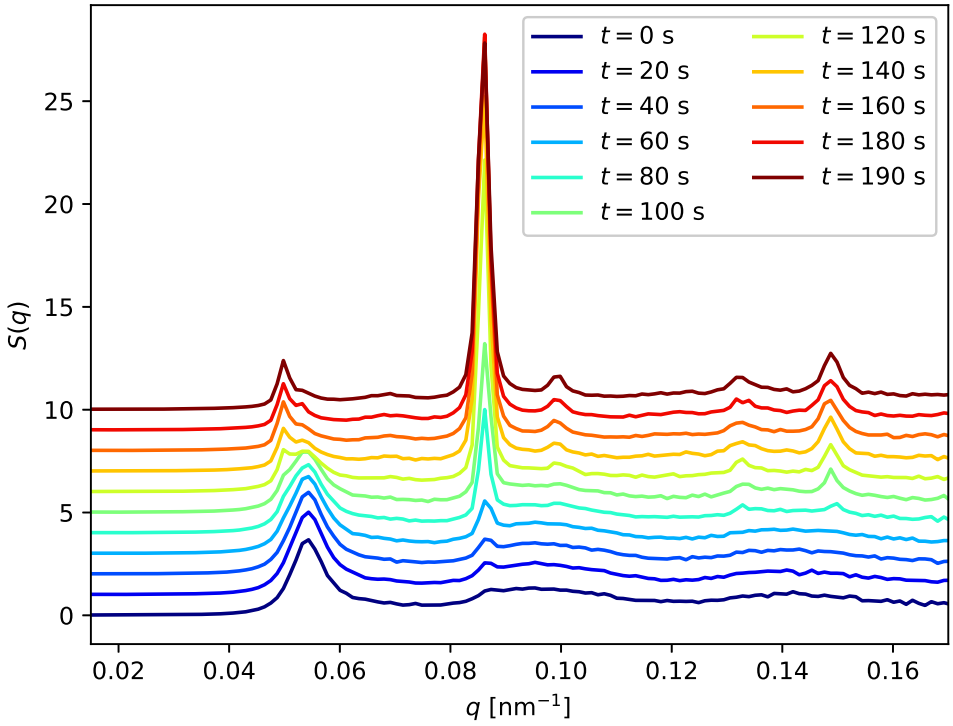

Figure 6.7: Structure factor of sample D at different time points of the shear experiment applying a shear stress of $\tau = 100$ Pa. The graphs are shifted vertically for clarity.

The maximum of the liquid structure factor at around $q \approx 0.053$ nm^{-1} decreases over time while the Bragg peaks begin to appear and get more pronounced. The peak at $q = 0.086$ nm^{-1} which corresponds to the Bragg reflections with hexagonal order observable from the beginning of the experiment is the most intense. In addition to the increasing intensity of the appearing peaks, their position slightly shifts to larger scattering vectors with time.

The underlying real space structure of the sample is a two-dimensional hexagonal layer structure (see also figure 6.32 at the end of section 6). Figures 6.8 and 6.9 show the structure factor of sample D calculated from the powder-like pattern (image e) in figure 6.2) and the final scattering pattern (image f) in figure 6.2) together with the calculated positions of Bragg reflections assuming the two-dimensional hexagonal layer structure.

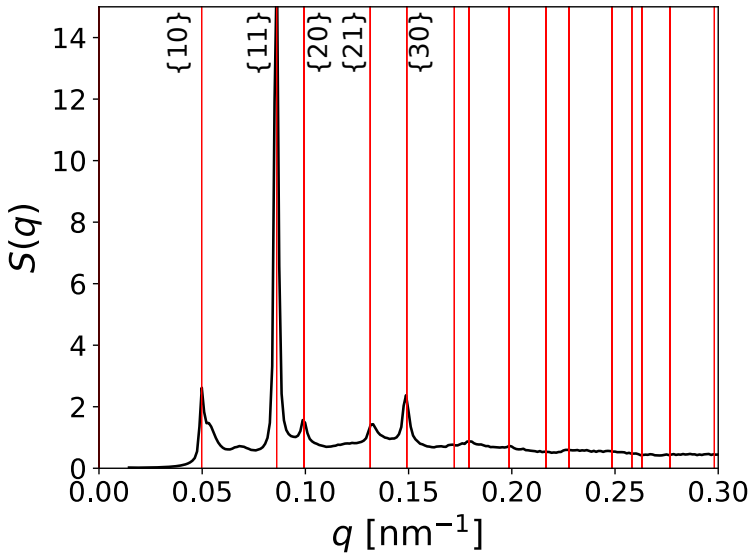

Figure 6.8: Structure factor of the powder-like scattering pattern of sample D. The red lines correspond to the positions of Bragg reflections originating from a two-dimensional hexagonal layer structure with a lattice constant of $a = 146$ nm.

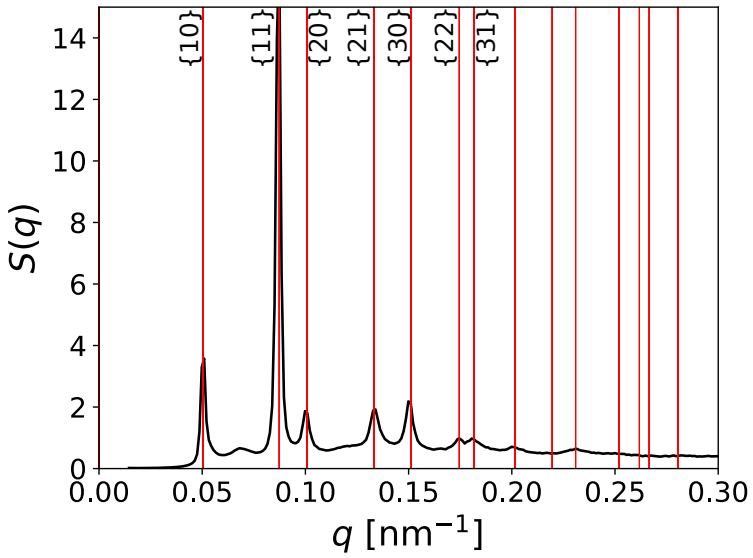

Figure 6.9: Structure factor of the final scattering pattern of sample D. The red lines correspond to the positions of Bragg reflections originating from a two-dimensional hexagonal layer structure with a lattice constant of $a = 144$ nm.

The positions of Bragg reflections originating from a two-dimensional hexagonal layer structure can be calculated using equation 6.1 [10]. It should be noted that this calculation predicts only the position of the Bragg reflections while no

statement is made about the intensities.

$$q_{hk} = \frac{2}{\sqrt{3}} \frac{2\pi}{a} \sqrt{h^2 + k^2 + hk} \tag{6.1}$$

Here, h and k are the Miller indices and a is the lattice constant of the hexagonal lattice. The results from the calculation show that the assumption of a two-dimensional hexagonal lattice is predicting the position of observable peaks in the structure factor reasonably well. The shoulder close to the {10} reflection visible in figure 6.8 can be attributed to the residual underlying liquid structure factor maximum. The peak between the {10} and {11} reflection observable in both figures is, however, not predicted by the model. A possible explanation could be an increase of three-dimensional order, in which case this particluar peak could correspond to the {102} reflection of a hexagonal close-packed unit cell.

The occurence of Bragg reflections with hexagonal symmetry can be attributed to the formation close-packed two-dimensional layers of particles when shear is applied to the sample. In the beginning, only thin layers exist so that only the most intense {10} reflection can be observed. The other, less intense, reflections are not observable since they are dominated by the structure factor of the liquid-like ordered particles. At higher shear rates the layers are growing so that also these reflections become visible. The formation of a powder-like scattering pattern indicates that multiple layers are forming which are parallel, but randomly oriented, i. e. randomly rotated around the layer normals.

Apparently, the short rotation with the comparably high shear rate of $\dot{\gamma} = 1\ \mathrm{s}^{-1}$ in order to position the cone of the rheometer correctly, caused the layers to orient themselves, the result of which is the scattering pattern with much sharper Bragg reflections as seen in figure 6.2 f).

The behavior of the sixth Fourier coefficient of the cross-correlation function C_6 over time was already shown for the case of low shear stress where no significantly structured signal could be observed. Beginning from a shear stress of $\tau = 10$ Pa an oscillating behavior starts to show. Figures 6.10 - 6.12 illustrate the behavior of C_6 over time in the last three measurements of sample D.

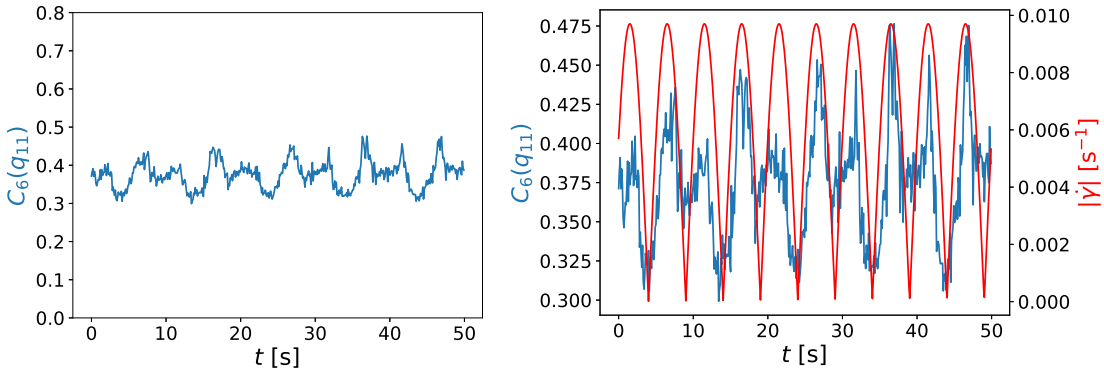

Figure 6.10: Sixth Fourier coefficient of the cross-correlation function of sample D at $\tau = 10.0$ Pa. Left: clean illustration of C_6; right: C_6 overlayed with the corresponding shear rate.

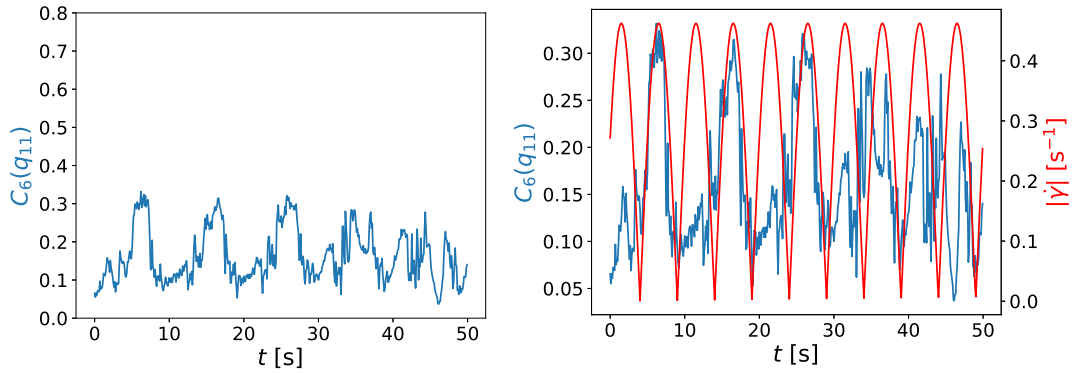

Figure 6.11: Sixth Fourier coefficient of the cross-correlation function of sample D at $\tau = 100.0$ Pa. Left: clean illustration of C_6; right: C_6 overlayed with the corresponding shear rate.

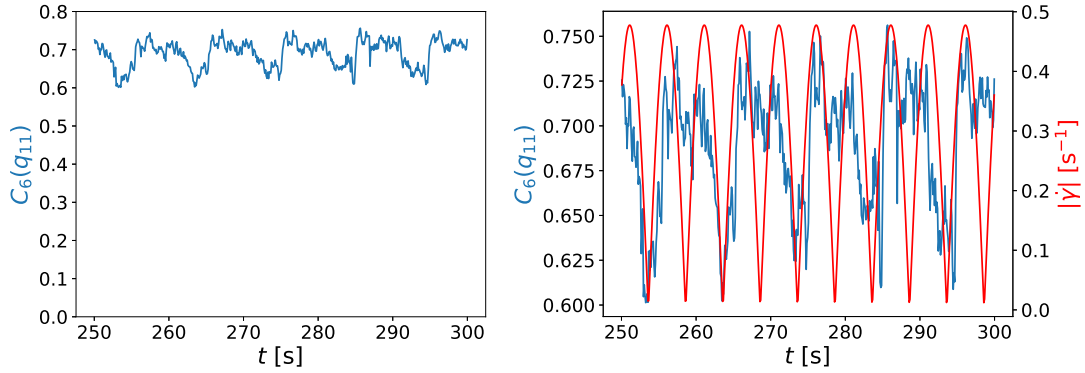

Figure 6.12: Sixth Fourier coefficient of the cross-correlation function of sample D at $\tau = 100.0$ Pa after the sample is ordered due to the application of rotational shear. Left: clean illustration of C_6; right: C_6 overlayed with the corresponding shear rate.

It can be observed that C_6 calculated at the $\{10\}$ reflection is oscillating. The minima are different from zero which is another indication for the persistent layer structure.

In case of the $\tau = 10.0$ Pa measurement, the oscillations have the same frequency as the shear rate. However, it can be observed, that every other maximum has a lower amplitude than the previous one. This is even more obvious in the first measurement at $\tau = 100$ Pa. Looking at the second measurement at this shear stress, the oscillation of C_6 occurs with only half of the frequency. During one oscillation period the Fourier coefficient is increasing together with the shear rate. After reaching the shear rate maximum, C_6 is roughly constant for a whole oscillation period and finally decreases together with the shear rate again. Both of these phenomena cannot be explained at this point in time and need further investigation.

Sample D shows the expected shear thinning behavior as illustrated in figure 6.13.

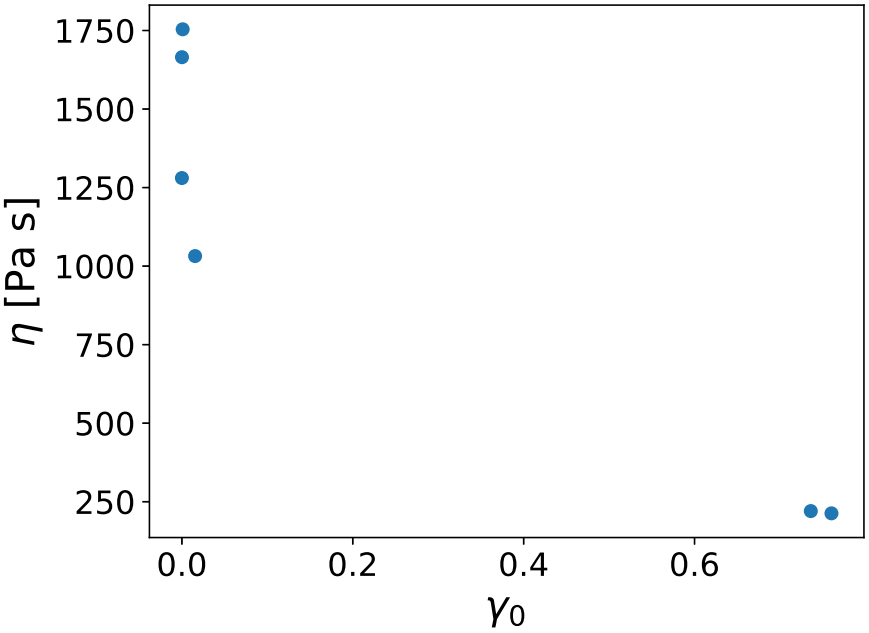

Figure 6.13: Viscosity of sample D as a function of deformation.

The viscosity at low deformations is significantly higher compared to the other samples (see following sections). Sample D is the one with the highest volume fraction, a possible explanation for the comparably high viscosity is the phase diagram of hard spheres. As shown in figure 2.2 the phase behavior changes from liquid-like to supercooled in this regime of volume fractions. The exact volume fractions of this transition may vary because of the dispersity of the sample. The overall course of the decreasing viscosity at increasing deformations is, however, similar.

In figure 6.14, the variance of the sixth Fourier coefficient calculated at the {11} reflection as a function of deformation is displayed. The dependence of the variance of the sixth Fourier coefficient can be interpreted as beeing linear. However, only very few data points can be evaluated for sample D. For the following samples, the measurement procedure was adjusted to investigate the behavior in greater detail. Instead of measuring with constant shear stresses τ constant deformation amplitudes γ_0 are applied and the deformations are chosen such that a sufficient interval of datapoints becomes available. See section 5.4 for a detailed explanation of the measurement protocol.

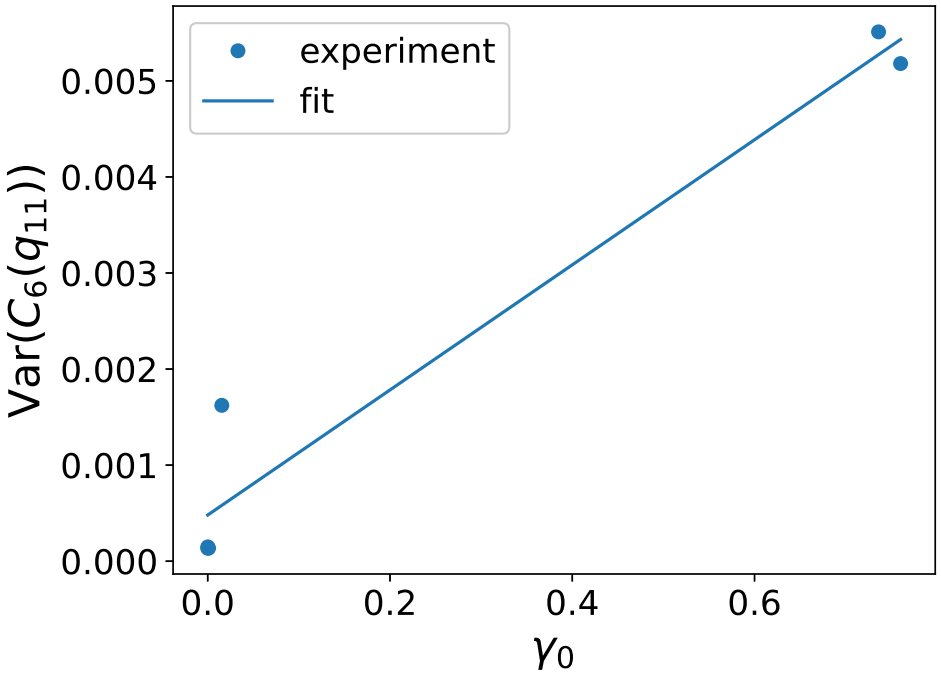

Figure 6.14: Variance of the sixth Fourier coefficient of the cross-correlation function as a function of deformation of sample D.

6.2 Samples at Intermediate Volume Fraction

The rheological and structural behavior of the samples A and B with volume fractions of $\phi = 0.50$ and $\phi = 0.52$, respectively, is similar and will be discussed in detail in this section.

6.2.1 Low Oscillation Amplitudes

In the first part, the behavior of the samples at oscillation amplitudes of $\gamma_0 = 0.32$ and below are discussed. While the rheological behavior does not change at higher amplitudes, the x-ray scattering results are different and, hence, discussed in a separate section.

Small-Angle X-ray Scattering

Figure 6.15 shows the scattering pattern of sample A at rest at the beginning of the shear experiment. The scattering pattern resembles the one shown before in the evaluation of the structure factor. Compared to the previous sample D, the intensity maxima appear at smaller scattering vectors which is expected because of the larger particle radii. Other than that, they are similar and show the same behavior as expected for a liquid-like ordered sample.

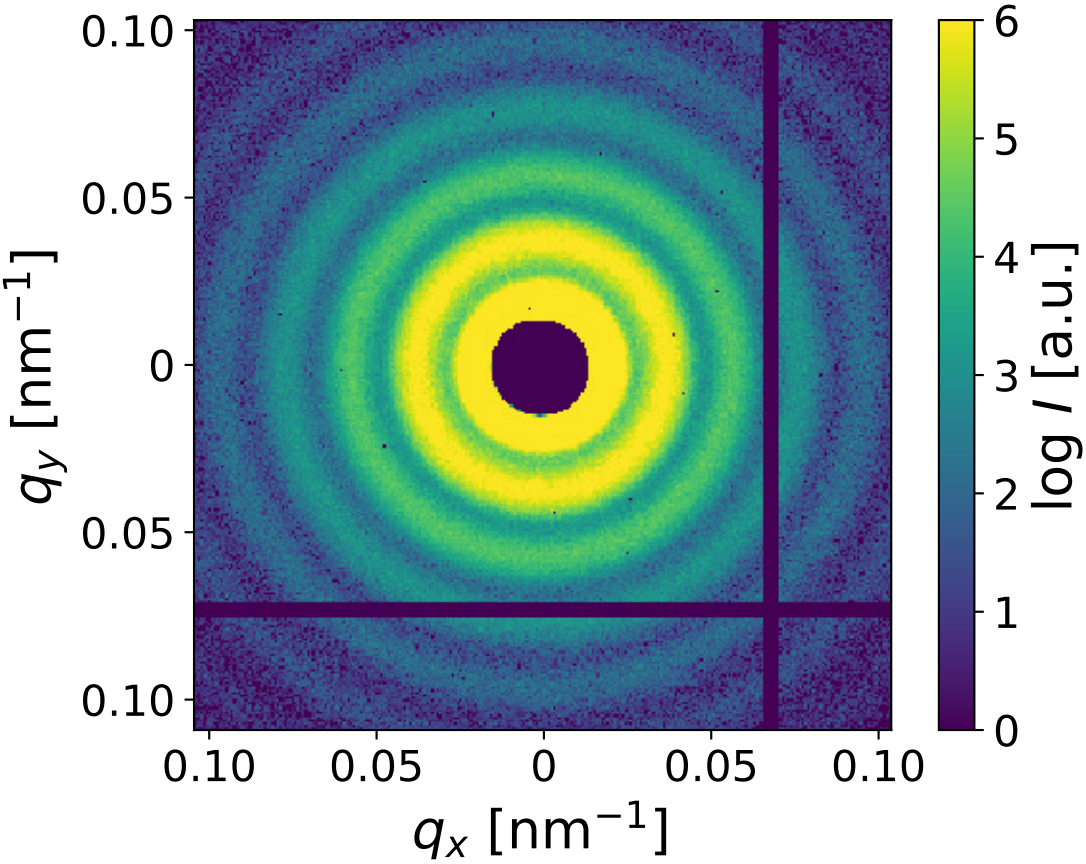

Figure 6.15: Scattering pattern of sample A at rest before the start of the shear experiment recorded with an exposure time of one second. The pattern shows the same intensity distribution as the structure factor shown before.

For the investigation of this sample, shear forces are applied in the way described in section 5.4. Oscillatory shear is used at a frequency of 0.1 Hz starting from a deformation of $\gamma_0 = 0.01$. Subsequently, the deformation is doubled after every five oscillation cycles which corresponds to a time of 50 s per deformation. During the shear experiment x-ray scattering images where taken with an exposure time of 0.2 seconds each. The scattering pattern displayed in figure 6.16 shows the scattered intensity of sample A averaged over the first 5000 images, i. e. the first 1000 s of the experiment.

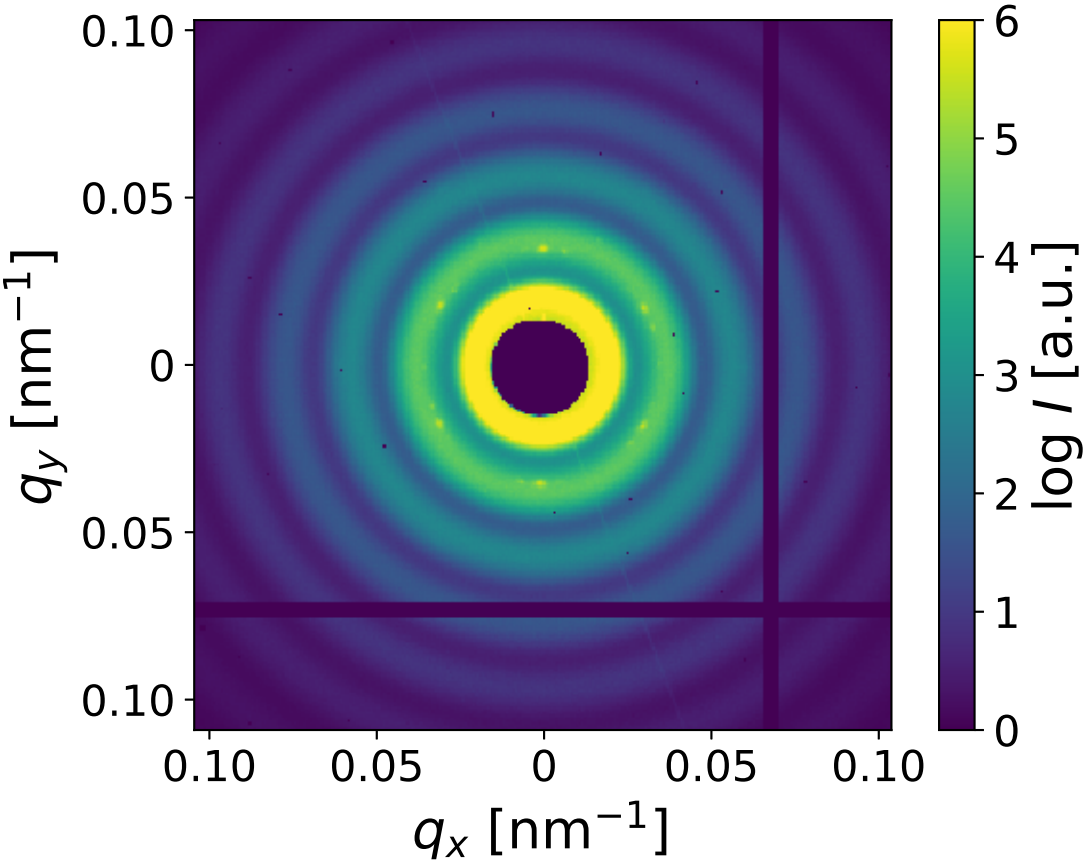

Figure 6.16: Scattering pattern of sample A under shear averaged over the first 1000 seconds of the experiment. Bragg reflections with hexagonal symmetry are visible in the second structure factor maximum at $q = 0.035$ nm^{-1}.

In figure 6.16, Bragg reflections with a hexagonal symmetry can be observed in addition to the liquid structure factor. The reflections are located in the second maximum of the scattering pattern. Upon closer inspection, it can be seen that a second set of Bragg reflections with hexagonal symmetry is visible rotated by a few degrees. In the structure factor calculated from the averaged data the existence of the Bragg reflections is indicated by a small shoulder at $q = 0.035$ nm^{-1} in the second maximum as illustrated in figure 6.17.

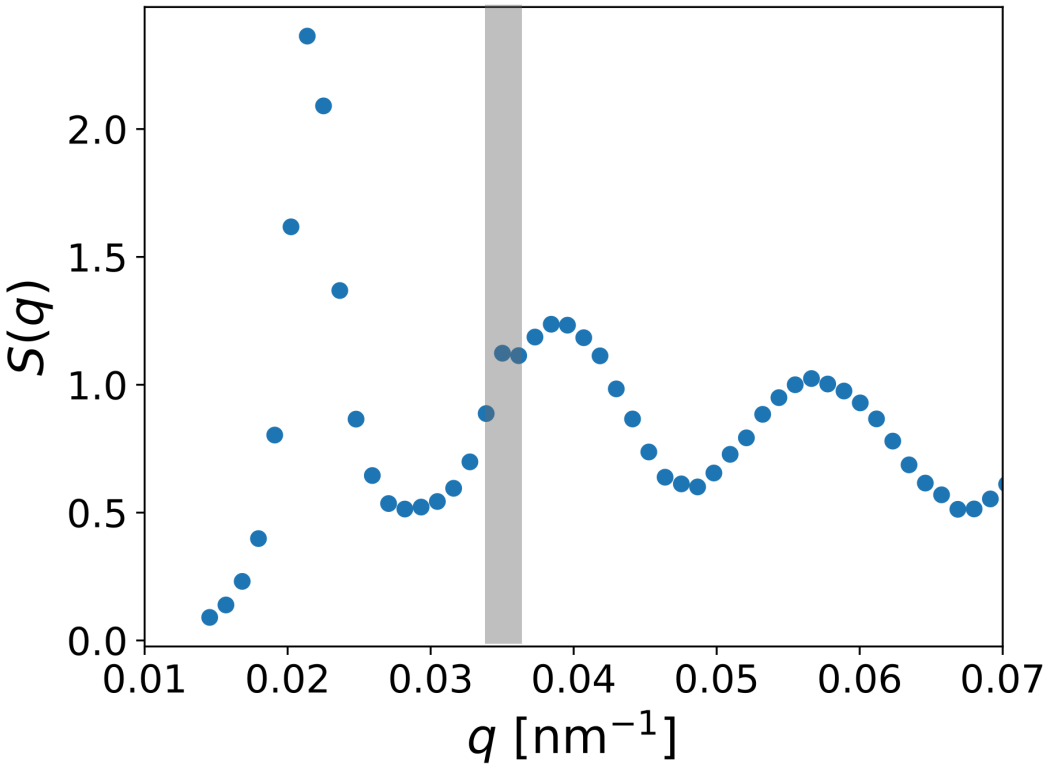

Figure 6.17: Structure factor of sample A calculated from the averaged scattering patterns recorded over the first 1000 seconds of the shear experiment. A small shoulder can be observed in the second maximum at $q = 0.035$ nm^{-1}.

Similar observations were made in various scattering experiments before [1–9]. The occurence of Bragg reflections with hexagonal symmetry can be explained by the formation of two-dimensional hexagonal close-packed layers forming perpendicular to the gradient of shear, and, thus, perpendicular to the incident photon beam [10] (see figure 6.32 at the end of this section). It can be calculated that the Bragg reflection with the highest relative intensity of this kind of structure is the (11) reflection [11] which is the one observable here. The twinned Bragg reflections indicate a second set of layers parallel to the first one but rotated. A possible explanation is that the layers are forming at both surfaces of the shear cell. However, this feature seems to occur randomly and no consistent parameters can be identified in that case. A more in-depth discussion about the two-dimensional layer structure of the sample forming under shear was already presented in section 6.1 for sample D.

As mentioned before, the scattering pattern shown in figure 6.17 is an average over 1000 seconds. Figure 6.19 shows individual scattering patterns recorded with an exposure time of 0.2 s at different stages of an oscillation cycle as illustrated in figure 6.18.

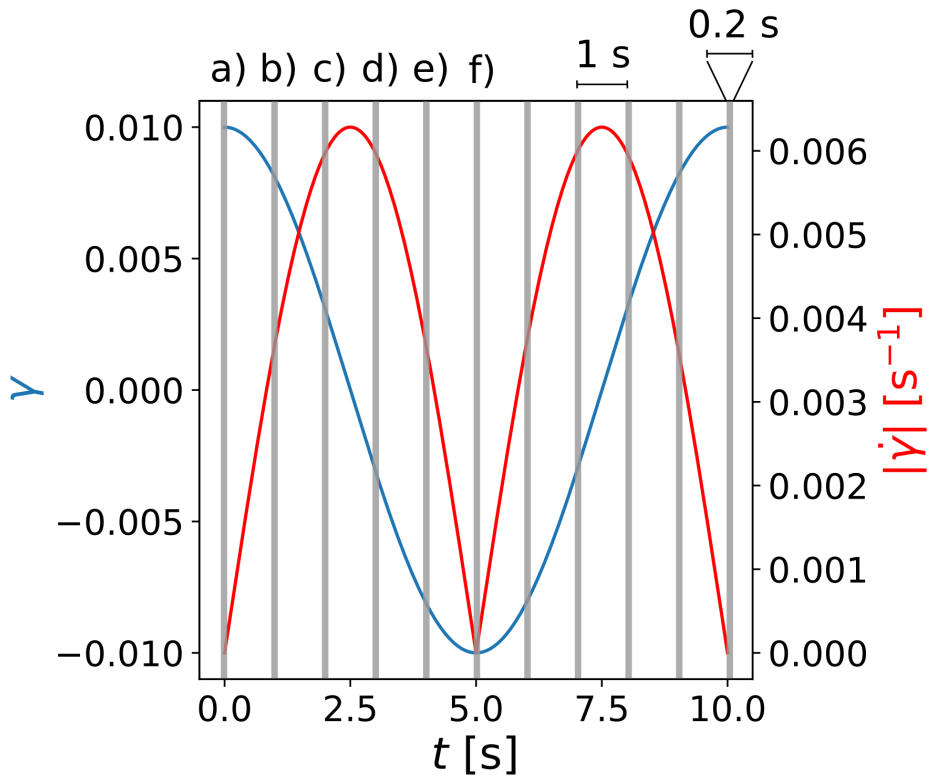

Figure 6.18: Illustration of the measurements taken in figure 6.19 in relation to the point in time of an oscillation cycle.

In the beginning of the oscillation period, that is, the cone of the rheometer does not move and the shear rate is zero, the scattering pattern is isotropic (figure 6.19 a)). When the cone starts rotating in the first direction, Bragg reflections with hexagonal symmetry become visible and are more and more pronounced as the cone accelerates. The intensity of the Bragg reflections decreases again when the cone decelerates and vanishes when the cone comes to stop after the first half of the oscillation cycle (figure 6.19 e)). The same behavior can be observed in the second half of the oscillation cycle. This phenomenon is in stark contrast to sample D where Bragg reflections were visible over the whole course of the measurement and not disappearing at low shear rates.

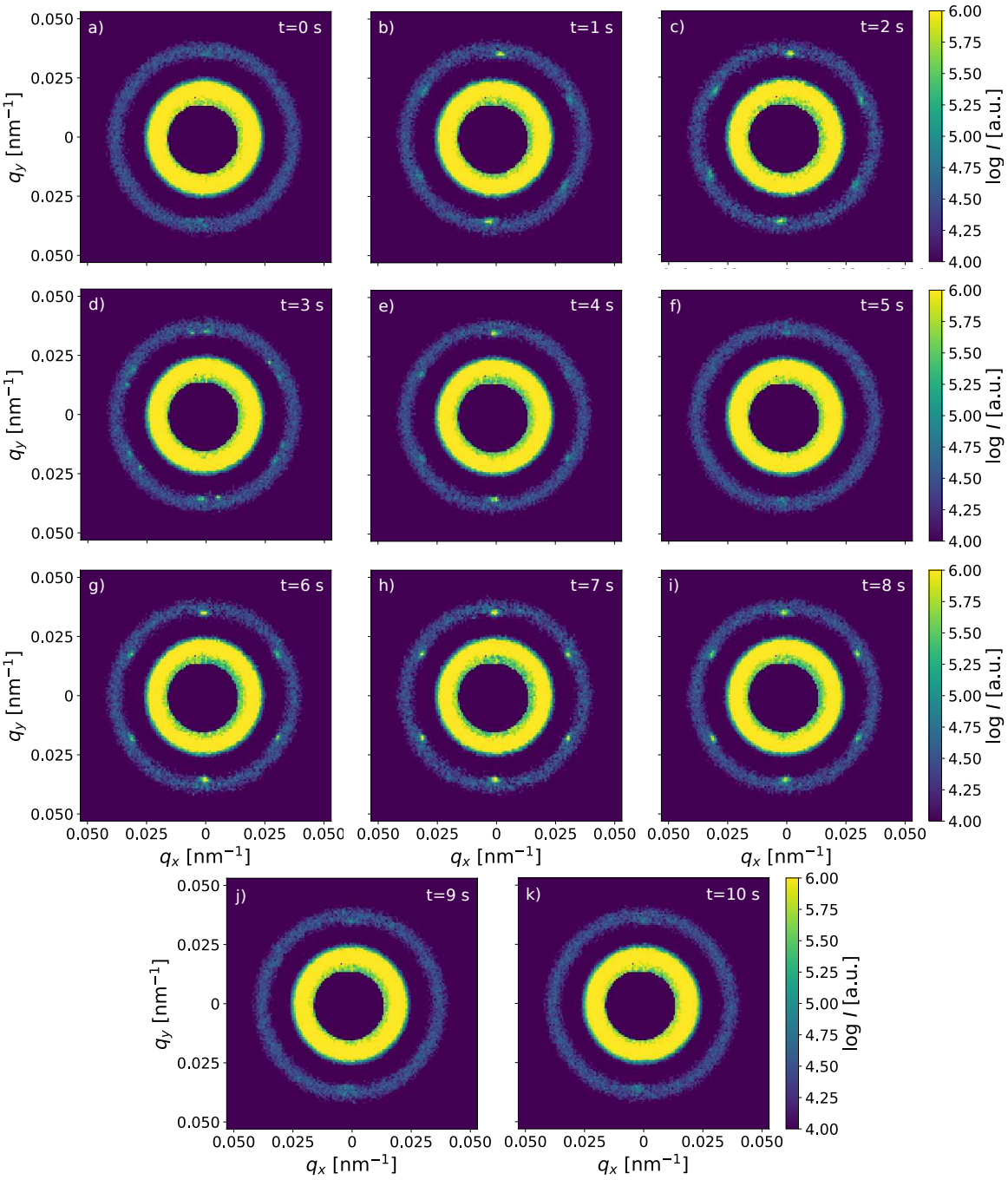

Figure 6.19: Scattering patterns of sample A recorded over one oscillation cycle with a deformation of $\gamma_0 = 0.16$ and an exposure time of 0.2 s each. Image a) represents the beginning of the oscillation cycle and each following pattern is taken one second after the previous one. In images a), f), and k) the shear rate is at a minimum and the pattern is isotropic. In the other images Bragg reflections with a six-fold symmetry are visible. The images were recorded at the end of set 2 of the protocol.

X-ray Cross-Correlation Analysis

To quantify the effects observable in the scattering patterns, higher order correlations in terms of the x-ray cross-correlation analysis are considered. To extract structural information beyond just the structure factor, the small shoulder appearing in the second maximum is reviewed in greater detail. In the first step, the cross-correlation function is calculated for the corresponding scattering vector of $q = 0.035$ nm^{-1}. The amplitudes C_l of the Fourier coefficients l extracted from the cross-correlation function and averaged over the whole 5000 images of this part of the measurement are shown in figure 6.20.

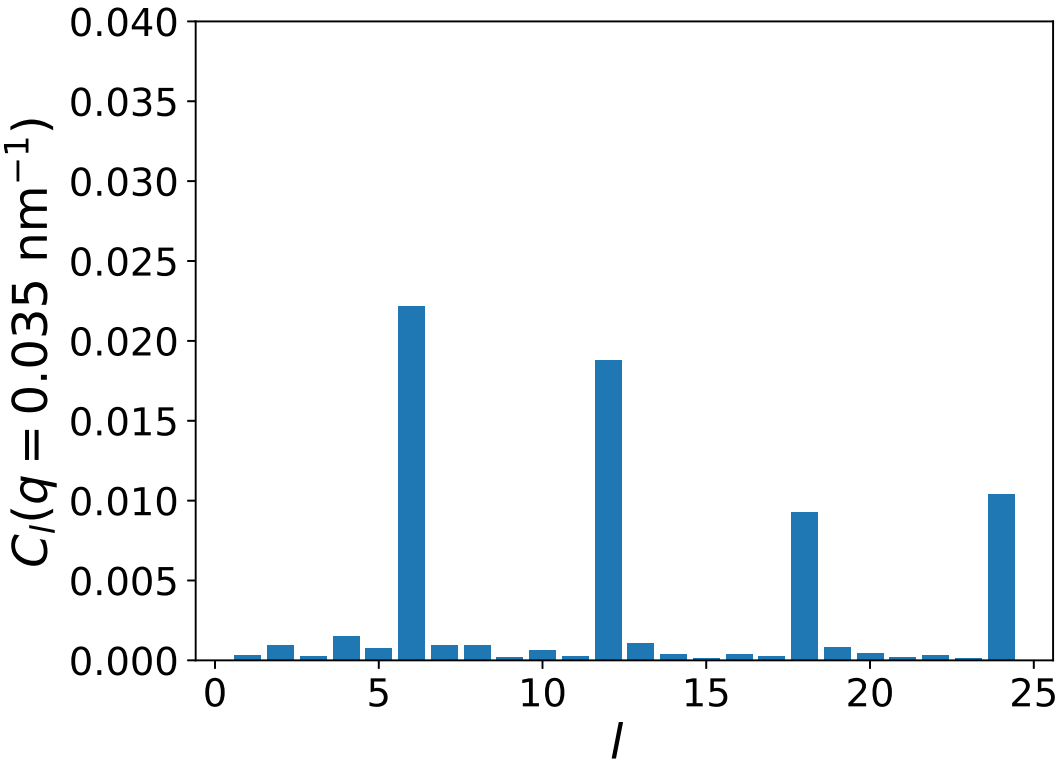

Figure 6.20: Amplitude of the Fourier coefficients calculated from the cross-correlation functions of sample A averaged over the first 5000 images. The cross-correlation functions are calculated at $q = 0.035$ nm^{-1} which is the position of the small shoulder in the second structure factor maximum. Fourier coefficients that are multiples of six are clearly dominant.

As expected from the scattering pattern shown before, the Fourier coefficients which are multiples of six are showing the largest amplitude. The sixth Fourier coefficient itself is a direct result of the hexagonal, azimuthal symmetry of the scattering pattern which leads to an angular cross-correlation function with six maxima in the intervall of 0 and 2π. The amplitude of the higher $6n$th coefficients are a result of the narrow width of the Bragg reflections and, thus, narrow width of the peaks in the cross-correlation function[91]. An examplary cross-correlation

function of a single scattering pattern together with the amplitudes of the extracted Fourier coefficients is shown in figure 6.21.

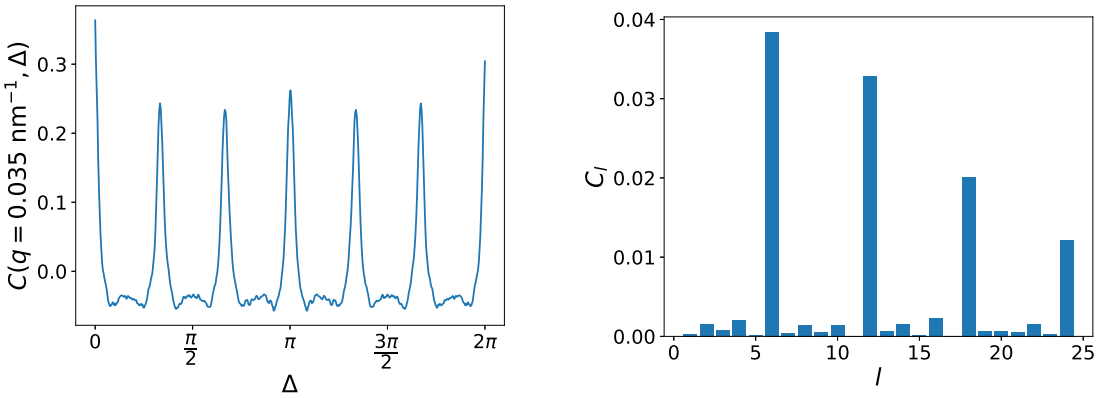

Figure 6.21: Cross-correlation function (left) and corresponding amplitudes of the extracted Fourier coefficients (right) of a single scattering pattern of sample A. The six-fold symmetry of the scattering pattern at the specified scattering vector is reflected in the six peaks of the cross-correlation function occuring at correlation angles that are multiples of $\pi/3$. Consequently, the Fourier coefficients which are multiples of six show the largest amplitudes.

Since the sixth Fourier coefficient is most dominant, it is investigated extensively in the following evaluations. To resolve C_6 in time, it is calculated for each individual scattering pattern and, to have an additional resolution in reciprocal space, for the measured range of scattering vectors q. The result of these calculations are shown in figure 6.22 for sample A in the first 1000 seconds of the experiment.

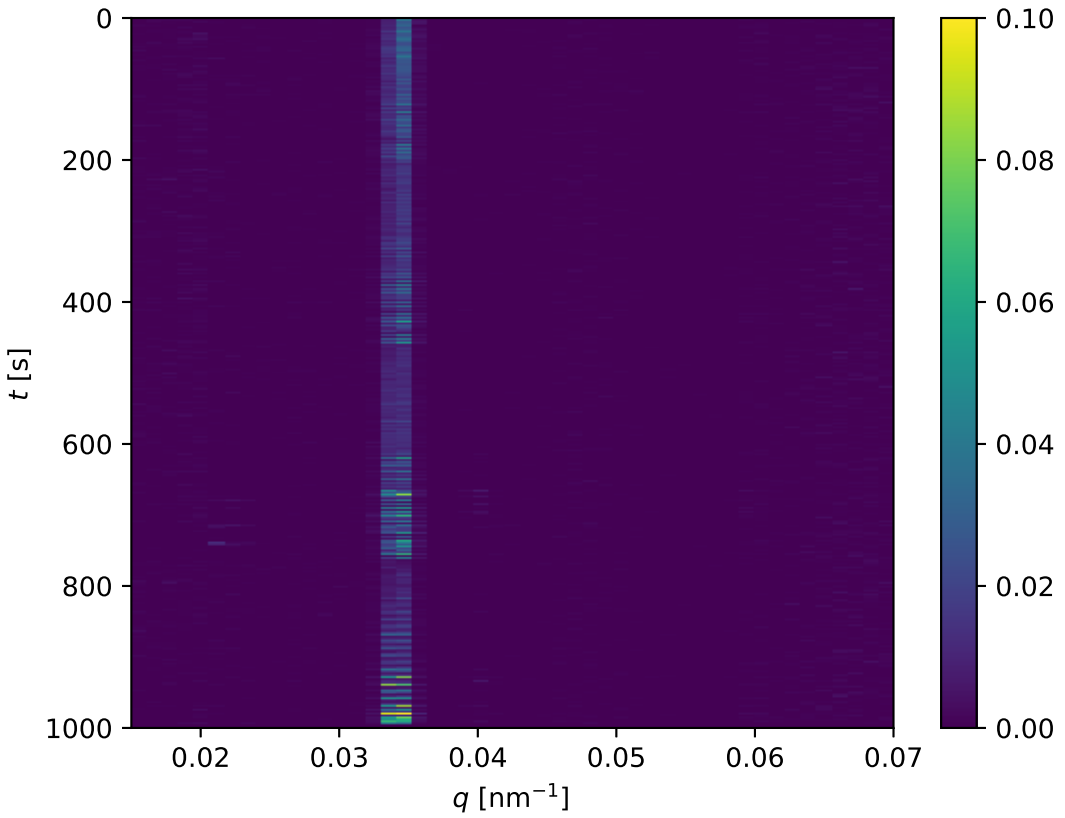

Figure 6.22: Amplitude of the sixth Fourier coefficient C_6 of the x-ray cross-correlation function resolved in time and reciprocal space of sample A. A pronounced amplitude is only observable at $q = 0.035$ nm^{-1}. At this scattering vector, the amplitude varies over time.

As a first result, it can be seen that a pronounced six-fold symmetry is only observable at $q = 0.035$ nm^{-1}. No additional, significant regions of six-fold symmetry in reciprocal space are found.

The second observation is that the amplitude of the sixth Fourier coefficient is not constant but varies over time. First of all, the amplitude increases gradually and then drops off very sharply at certain points in time. These sudden drops happen at around 200 s, 450 s, and 750 s, respectively. At these points in time, the oscillation amplitude switches from its previously highest value to $\gamma_0 = 0.01$ and a new set of increasing deformations starts. This behavior can be quantified by evaluating the amplitude of the sixth Fourier coefficient of the cross-correlation function over time. A few examples are shown in the following figures 6.23 to 6.25.

In these illustrations, C_6, calculated at $q = 0.035$ nm^{-1}, is displayed as a function of time. The time segments are chosen such that the full five oscillation cycles at a constant deformation γ_0 are included. For an oscillation frequency of 0.1 Hz and five oscillation cycles this corresponds to a time period of 50 seconds. With an exposure time of 0.2 seconds, 250 scattering patterns are evaluated in this time frame.

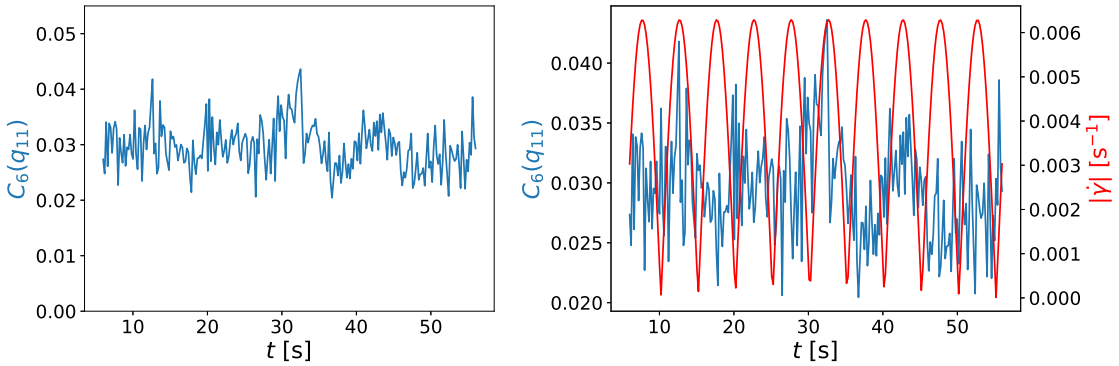

Figure 6.23: Sixth Fourier coefficient of the cross-correlation function of sample A at $\gamma_0 = 0.01$. Left: clean illustration of C_6; right: C_6 overlayed with the corresponding shear rate.

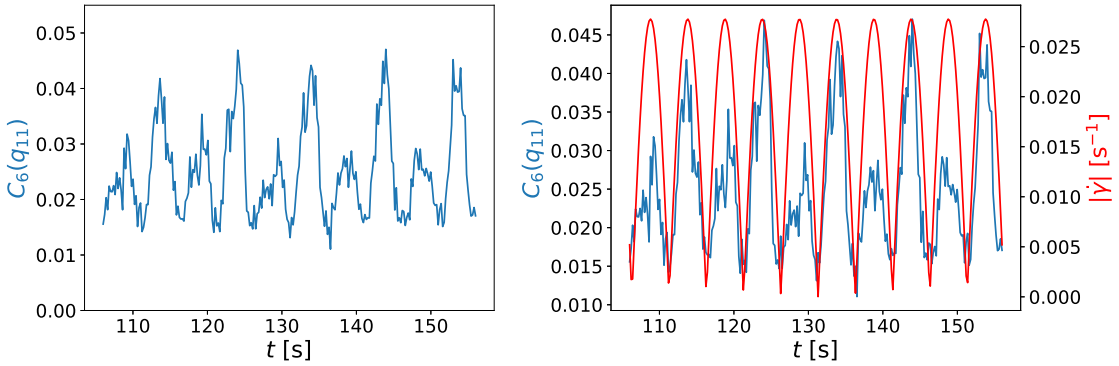

Figure 6.24: Sixth Fourier coefficient of the cross-correlation function of sample A at $\gamma_0 = 0.04$. Left: clean illustration of C_6; right: C_6 overlayed with the corresponding shear rate.

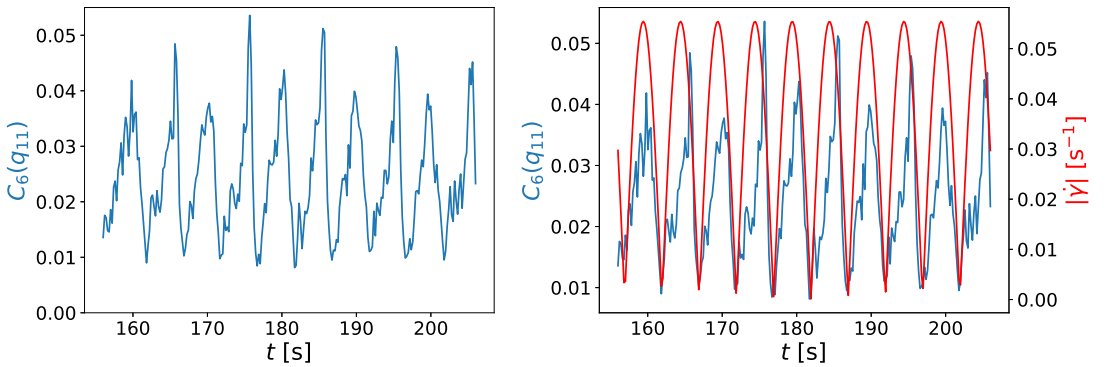

Figure 6.25: Sixth Fourier coefficient of the cross-correlation function of sample A at $\gamma_0 = 0.08$. Left: clean illustration of C_6; right: C_6 overlayed with the corresponding shear rate.

For low deformations γ_0 the sixth Fourier coefficient is low in amplitude and resembles a noisy pattern. As the deformation increases, the amplitude of C_6

becomes larger and, in addition, shows a significant oscillating behavior. When compared to the shear rate, it can be seen that the amplitude of the Fourier coefficient follows the oscillation of the shear rate with the same frequency. When the shear rate drops to zero, the Fourier coefficient shows a minimum as well, whereas the maximum of the shear rate coincides with a maximum of C_6.

It should be highlighted that the absolute value of the shear rate is displayed. Since the shear rate follows a cosine, in principle, negative values of $\dot{\gamma}$ occur. However, the sign of the shear rate only corresponds to the rotation direction of the cone. Since both directions are equal, the sign is not considered here.

At this point, it is also important to note that the phase of the shear rate is corrected such that the maxima of $\dot{\gamma}$ and C_6 match. As mentioned before, the rheometer is not synchronized with the detector so that rheological properties do not match the temporal course of the x-ray measurements perfectly:

First of all, both the detector and the rheometer are not started at exactly the same time, which leads to a general offset between the x-ray scattering and the rheology timelines. Secondly, during the first 1000 s of this particular experiment, the Lambda detector recorded images continuously every 0.2 s. The rheometer, on the other hand, was started with the amplitude program mentioned above. The measurement of a single deformation γ_0 was continuous over the five oscillation cycles, i. e. 50 seconds (as for example shown in figures 6.23 - 6.25). However, whenever the rheometer changes the oscillation amplitude to start the next five cycles, there is a short delay before the cone's oscillation continues. To compensate for that, for the evaluations discussed here, the x-ray data was cut into 50 second segments and for each segment an individual time offset was chosen to fit the criteria mentioned before when calculating the shear rate. The offsets are not significantly large and range only between from 0 to 1.5 seconds. Furthermore, the x-ray measurements were performed in sets of 5000 images. Thus, in between two sets, for a few seconds of the rheology experiment no x-ray images were taken. For the evaluation of the second 5000 images, again, another general time offset is chosen to compensate for the missing seconds.

This procedure does not change the general observation that C_6 changes with the same frequency as $\dot{\gamma}$. Thus, it can be concluded that the six-fold symmetry is induced by shear forces. However, since there is no confirmed phase relation between the rheological data and the x-ray data, it is not necessarily the case that maxima and minima of both measurements coincide. The formation of six-fold symmetry could be slightly shifted out of phase from the variation of the shear rate. Unfortunately, no definitive conclusions can be drawn from the experiment concerning that matter.

A peculiar feature of C_6 as a function of time is that, most of the time, every other peak is significantly less intense than the previous one. This behavior was also observable in the case of sample D. In extreme cases, this leads to the circumstance that sometimes only half of the peaks are observable, whereas sometimes all peaks show the same amplitude. Intriguingly, there does not seem to be any systematic scheme and no conclusion can be drawn at this point. An explanation for this phenomenon requires further investigation.

Time-Resolved Small-Angle X-ray Scattering

For the evaluation of the sixth Fourier coefficient of the cross-correlation functions, the calculations are performed at the scattering vector, where the small shoulder in the second structure factor maximum appears. In addition to that, the first maximum of the structure factor is investigated. Therefore, the position $q_{\max}$ as well as the height $S(q_{\max})$ of the structure factor maximum are observed over the course of time. Both parameters are determined by fitting the first structure factor maximum to a single Gaussian function as defined in equation (6.2).

$$f(x) = a \exp\left(-\frac{(x-b)^2}{c}\right) + d \tag{6.2}$$

Using this equation, the parameters mentioned before can be retrieved as

$$\begin{aligned} q_{\max} &= b \\ S(q_{\max}) &= a + d \quad . \end{aligned}$$

A typical fit is shown in figure 6.26.

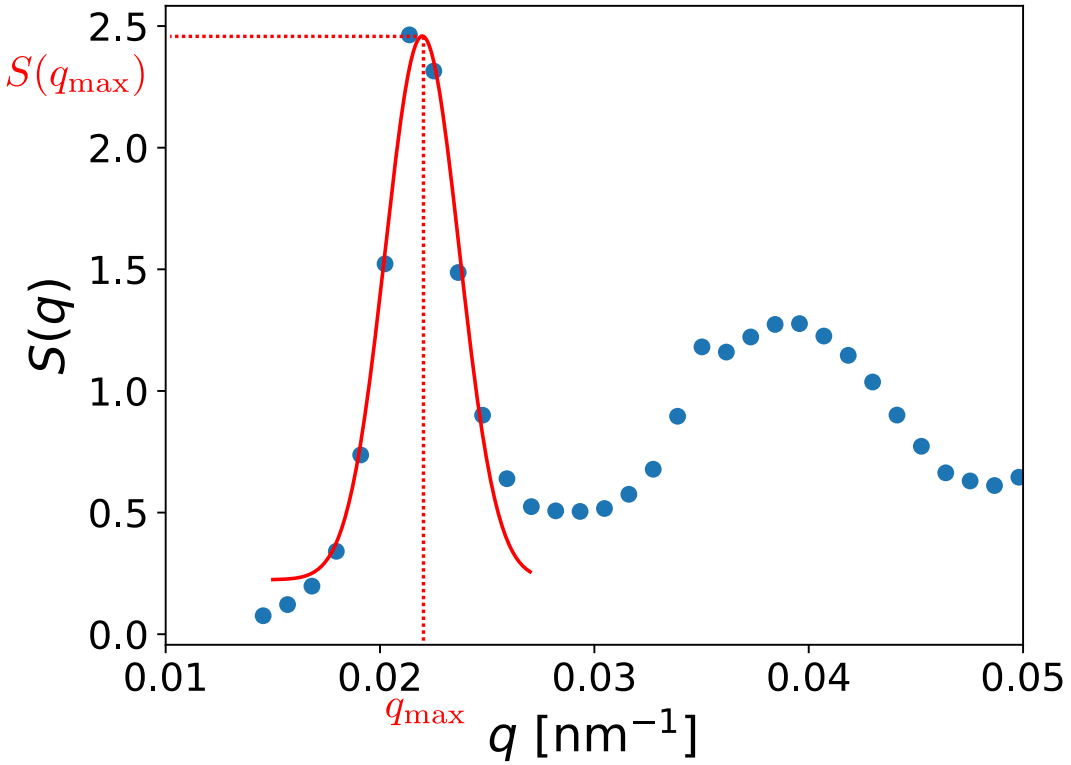

Figure 6.26: First maximum of the structure factor of sample A fitted by a Gaussian function. The height as well as the postion of the maximum can be retrieved from this fit.

The Gaussian function is chosen because of its simplicity: it can be calculated relatively fast and the height and position of the maximum are easily extracted.

A better approach to fit the structure factor would be the Percus-Yevick approximation as used before for the determination of the volume fraction. Fitting such a function is, however, more time consuming and, more importantly, the extraction of $q_{\max}$ as well as $S(q_{\max})$ is not straight forward and involves additional numerical methods.

Admittedly, it is evident from figure 6.26 that a Gaussian function is a very rough approximation of the structure factor maximum. It should be highlighted, that $S(q_{\max})$ is underestimated but the position of the maximum is relatively well approximated. Furthermore, two general problems arise because of the resolution in the scattering vector space. The maximum resolution of one pixel width is used when integrating the detector signal. This leads to the fact that, on the one hand, the structure factor maximum is not well resolved in the original function and, on the other hand, only between five to ten points can be used to perform the fit. Therefore, the results from the Gaussian fit are used as a relative measure during the following evaluations. The absolute values are not considered here.

As in the section above, the postion and height of the first structure factor maximum can be investigated over time. The evolution of these parameters over the course of the experiment is shown in figures 6.27 - 6.29.

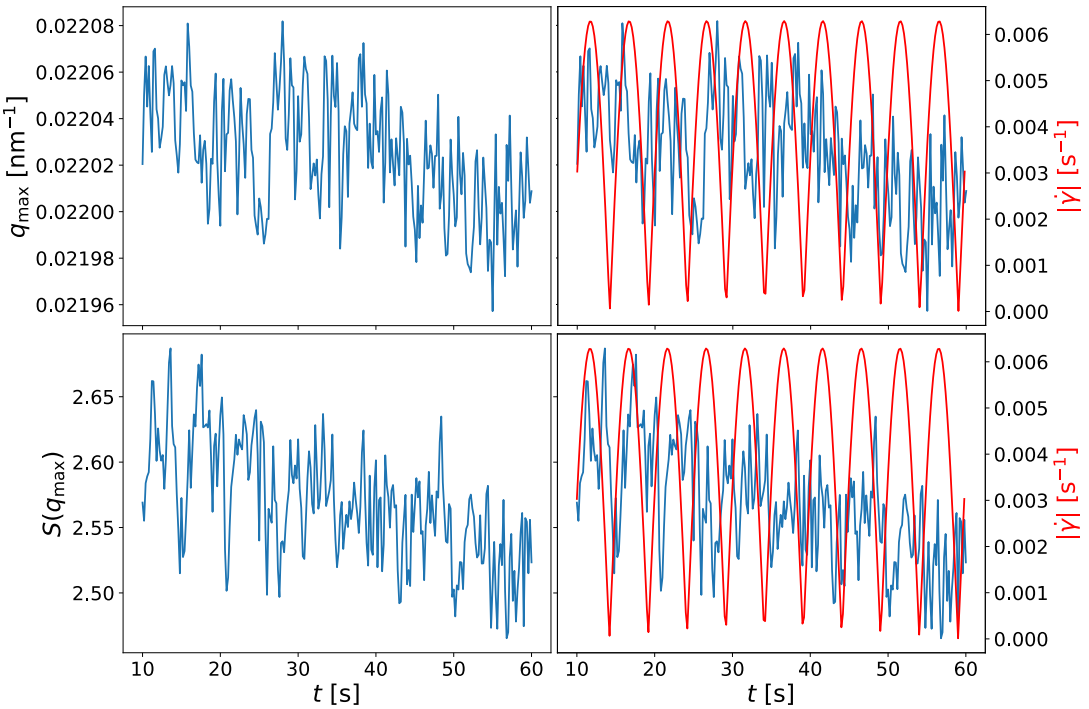

Figure 6.27: Parameters of the first structure factor maximum of sample A at $\gamma_0 = 0.01$. In addition to the clean illustration on the left, an overlay with the corresponding shear rate is shown on the right.

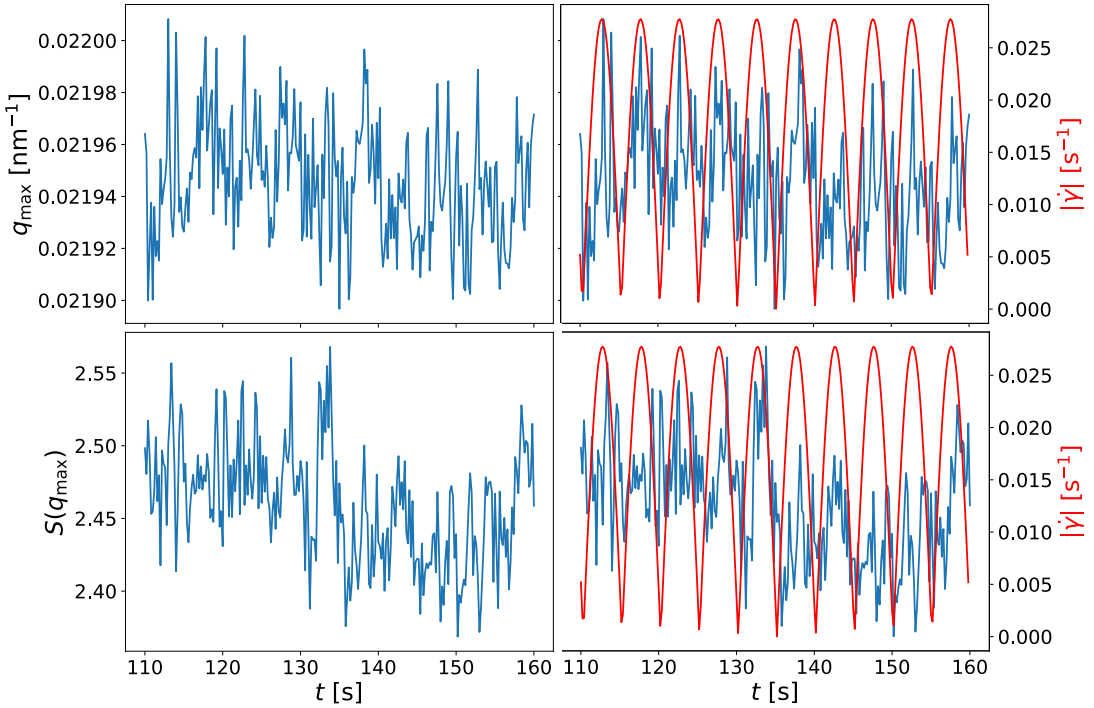

Figure 6.28: Parameters of the first structure factor maximum of sample A at $\gamma_0 = 0.04$. In addition to the clean illustration on the left, an overlay with the corresponding shear rate is shown on the right.

In the figures 6.27 to 6.29, the behavior of the structure factor maximum seems to follow the same course as the sixth Fourier coefficient of the cross-correlation as evaluated in the previous section. At small deformations both the position as well as the height of the maximum show a noise-like pattern. When the deformation is large enough the course of the parameters becomes more structured and the parameters are oscillating with the same frequency as the shear rate. Again, for the calculation of the shear rate individual time offsets were used. These offsets are, however, exactly the same as used before in the XCCA evaluations. As a result, a maximum of the shear rate coincides with a maximum q-position as well as a maximum of $S(q_{max})$.

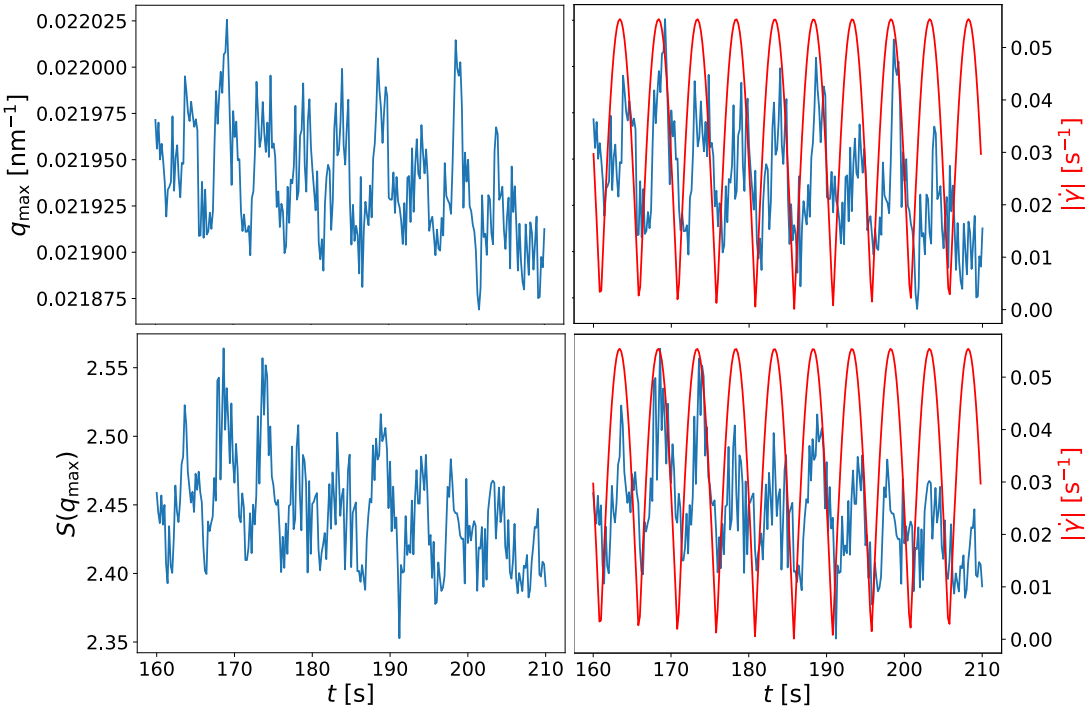

Figure 6.29: Parameters of the first structure factor maximum of sample A at $\gamma_0 = 0.08$. In addition to the clean illustration on the left, an overlay with the corresponding shear rate is shown on the right.

It is important to note that the outcome of these evaluations should be used cautiously. When comparing the range of values of both $q_{\max}$ as well as $S(q_{\max})$ at the smallest deformation with the highest deformation, it is evident that the fluctuation range is nearly the same, i. e. approximately 2.35 - 2.55 in case of the structure factor maximum and 0.0219 nm^{-1} - 0.0220 nm^{-1} in case of the q-position. The difference is only in the "more structured" oscillation of the parameters. In addition to that, the difference between the lowest and the highest values of $q_{\max}$ is in the range of the detector resolution and, thus, somehow artificial.

In comparison, the evaluation using x-ray cross-correlation analysis is more suited to investigate the structure of colloidal dispersions under shear. Not only is the calculation of the Fourier coefficients of the cross-correlation functions more robust, but it contains additional information beyond the structure factor. The symmetry information is not included in the structure factor but in the cross-correlation functions.

Rheological Behavior

The viscosity as a function of deformation is shown in figure 6.30 for samples A and B. Both samples show the same shear thinning behavior. The fits are calculated using the Ostwald-de Waele relationship shown in equation (3.7) and are discussed in detail in section 6.2.2. Sample A is measured using the protocol explained in section 5.4 and two series following this protocol were measured with

two different loadings of the sample. Sample B on the other hand is measured at the same deformation values but in individual measurements of 20 seconds each with an exposure time of 0.01 seconds. The findings and the approach of evaluation are, however, the same so that for sample B only the results are presented here.

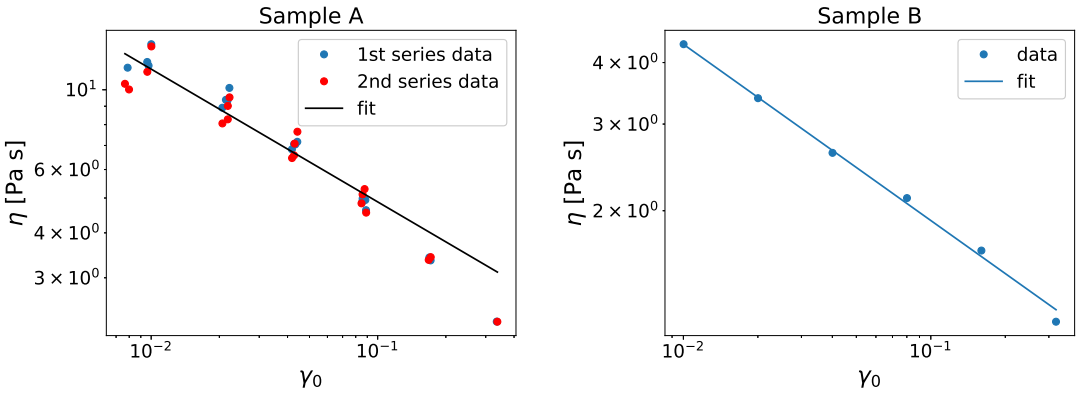

Figure 6.30: Viscosity of sample A (left) and B (right) as a function of deformation.

Since the viscosity is measured over the whole course of the oscillation cycles it can be considered an averaged value and, thus, it is not time resolved. To define a relation between the (time-resolved) XCCA results and the rheology measurements, the variance of the sixth Fourier coefficient is calculated [65]. The variance of C_6 can be used as a measure for the difference in the order of the sample at rest and the sample under shear. The result is shown in figure 6.31.

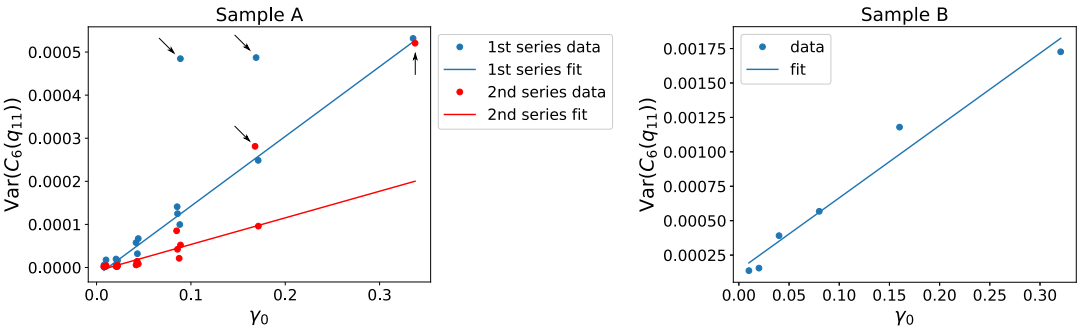

Figure 6.31: Variance of the sixth Fourier coefficient of the cross-correlation function as a function of deformation for sample A (left) and sample B (right). In case of sample A the data points marked by an arrow were omitted for the fit.

For both samples, the variance of C_6 increases with higher deformations nearly linearly. As it is expected from the shear thinning behavior, the magnitude of order increases at higher deformation and, hence, higher shear rates. This is well reflected by the growing variance of the sixth Fourier coefficient of the cross-correlation function.

Discussion of the Results

The small-angle x-ray scatterting data of the sample at rest does not show any distinctive features other than the structure factor. When exerting oscillatory shear forces on the sample, the nanoparticles in the dispersion medium begin to form structures. These structures result in a scattering pattern with hexagonal symmetry in reciprocal space and, thus, correspond to structures with hexagonal symmetry in real space.

This phenomenon can be explained with the formation of two-dimensional layers of close-packed spheres. The close-packing of spheres in two dimensions is the hexagonal one. When the shear rate increases, the inter-particle distance inside the layers becomes smaller as indicated by the shift of the position of the first structure factor maximum $q_{\max}$ to larger q. Thus, the particles become more ordered and the six-fold symmetry as measured by C_6 increases. It can be assumed that in this way, the inter-layer distance is maximized and the layers can slide past each other with less internal friction. This effect can be observed macroscopically in the decrease of the viscosity, i. e. shear thinning. Figure 6.32 illustrates the assumed real space structure of the sample at rest as well as under shear.

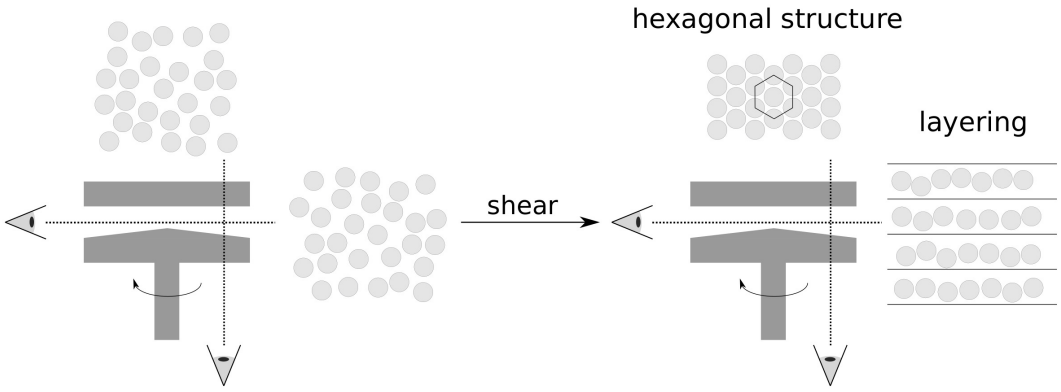

Figure 6.32: Assumed real space structure of the sample at rest as well as under shear.

6.2.2 High Oscillation Amplitudes

In this section, the behavior of samples A and B at deformations exceeding $\gamma_0 = 0.32$ are discussed further. The rheological behavior of the samples displays the expected course, i. e. the viscosity shows a shear thinning behavior. The viscosity as a function of deformation is illustrated in figure 6.33 for both samples. The fits shown in this figure use the Ostwald-de Waele relationship presented in equation (3.7).

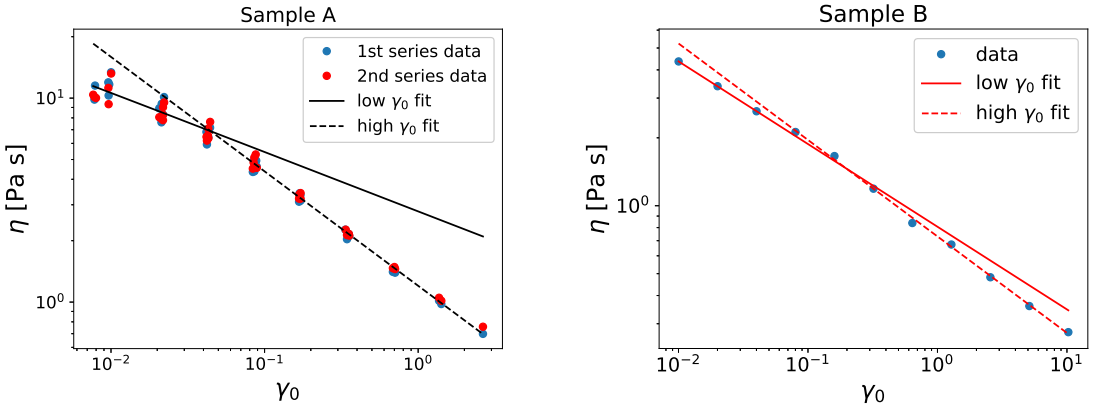

Figure 6.33: Viscosity of samples A (left) and B (right) as a function of deformation. Both samples show the characteristic shear thinning behavior. For sample A, two series with two different sample loadings are measured in the same way, both of which are displayed here.

Equation (3.7) shows the relation between the viscosity η and the shear rate $\dot{\gamma}$. Since the shear rate is extracted as a temporal average in the rheological measurements, it can be shown that the Ostwald-de Waele relationship equally relates the viscosity to the deformation amplitude γ_0. Using equation (3.17), one can show that

$$\langle\dot{\gamma}\rangle_t = \langle\gamma_0\omega\cos(\omega t)\rangle_t = \gamma_0\omega\langle\cos(\omega t)\rangle_t \tag{6.3}$$

$$= A\cdot\gamma_0 \quad \text{, with a constant } A = \omega\langle\cos(\omega t)\rangle_t \quad . \tag{6.4}$$

Therefore, the Oswald-de Waele relationship can be expressed using γ_0 with a modified flow consistency index K':

$$\eta = K\dot{\gamma}^{n-1} = K(A\cdot\gamma_0)^{n-1} = K\cdot A^{n-1}\cdot\gamma_0^{n-1} = K'\cdot\gamma_0^{n-1} \quad . \tag{6.5}$$

The values extracted from the fit are displayed in table 6.1.

Table 6.1: Ostwald-de Waele parameters of samples A and B

	Sample A		Sample B	
	K'	n	K'	n
low γ_0	2.8	-0.29	0.81	-0.37
high γ_0	1.2	-0.56	0.73	-0.43

As discussed in section 3 the interesting parameter is n which is indicative of the rheological behavior of a sample. As expected, for both samples these values are less than one indicating shear thinning behavior. Also, as stated earlier, the values are different in different regions of γ_0 and are lower at higher oscillation amplitudes. The flow consistency index K, or K' in this expression, acts as some kind of reference viscosity which is expectedly lower considering higher shear rates in the case of shear thinning samples.

While the rheological behavior continues to follow the expected course, the SAXS and XCCA results differ from the ones observed at lower amplitudes. Figure 6.35 shows a collection of averaged scattering patterns of sample A recorded after the sample had been deformed with an amplitude of $\gamma_0 = 0.32$ for the first time. The measurement is still the same as discussed in the previous section, i. e. the sample is deformed using the scheme described in section 5.4, but the results discussed here are from later points in time of the measurement. The images in this figure are ordered in time, that is the measurement in a) is directly followed by the measurement in b). The intervals used to produce the averaged scattering patterns of figure 6.35 are shown as an overview in figure 6.34.

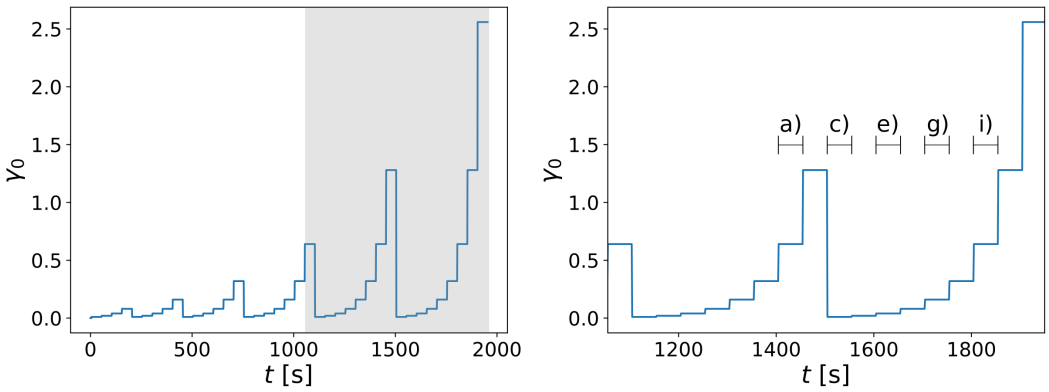

Figure 6.34: Variation scheme of the deformation amplitude over time. The right image shows only the grey part of the left image. The intervals containing the data of the following images in figure 6.35 are denoted in the right image.

In image a) of figure 6.35 the scattering pattern is analogous to the ones shown in the previous section at lower oscillation amplitudes. Bragg reflections with a hexagonal symmetry are observable in the second maximum of the liquid structure factor at the same value of the scattering vector. Interestingly, in image b) at a deformation of $\gamma_0 = 1.28$, all Bragg reflections vanish completely. Since the images are an average over five oscillation cycles and there are no Bragg reflections visible at all, no signs of hexagonal order are observable during the whole 50 seconds of measurement at this deformation. The structure of hexagonal layers is completely destroyed at these high shear rates.

After reaching the first maximum deformation of $\gamma_0 = 1.28$ at the end of the fith amplitude set, the sample is deformed with the minimum amplitude of $\gamma_0 = 0.01$, again (image c), start of the sixth amplitude set). Instead of the previously observed oscillating Bragg reflections with six-fold symmetry, a second set of hexagonal Bragg reflections rotated by 30° becomes visible. This observation corresponds the formation of a second set of close-packed hexagonal layers rotated with respect to the first one.

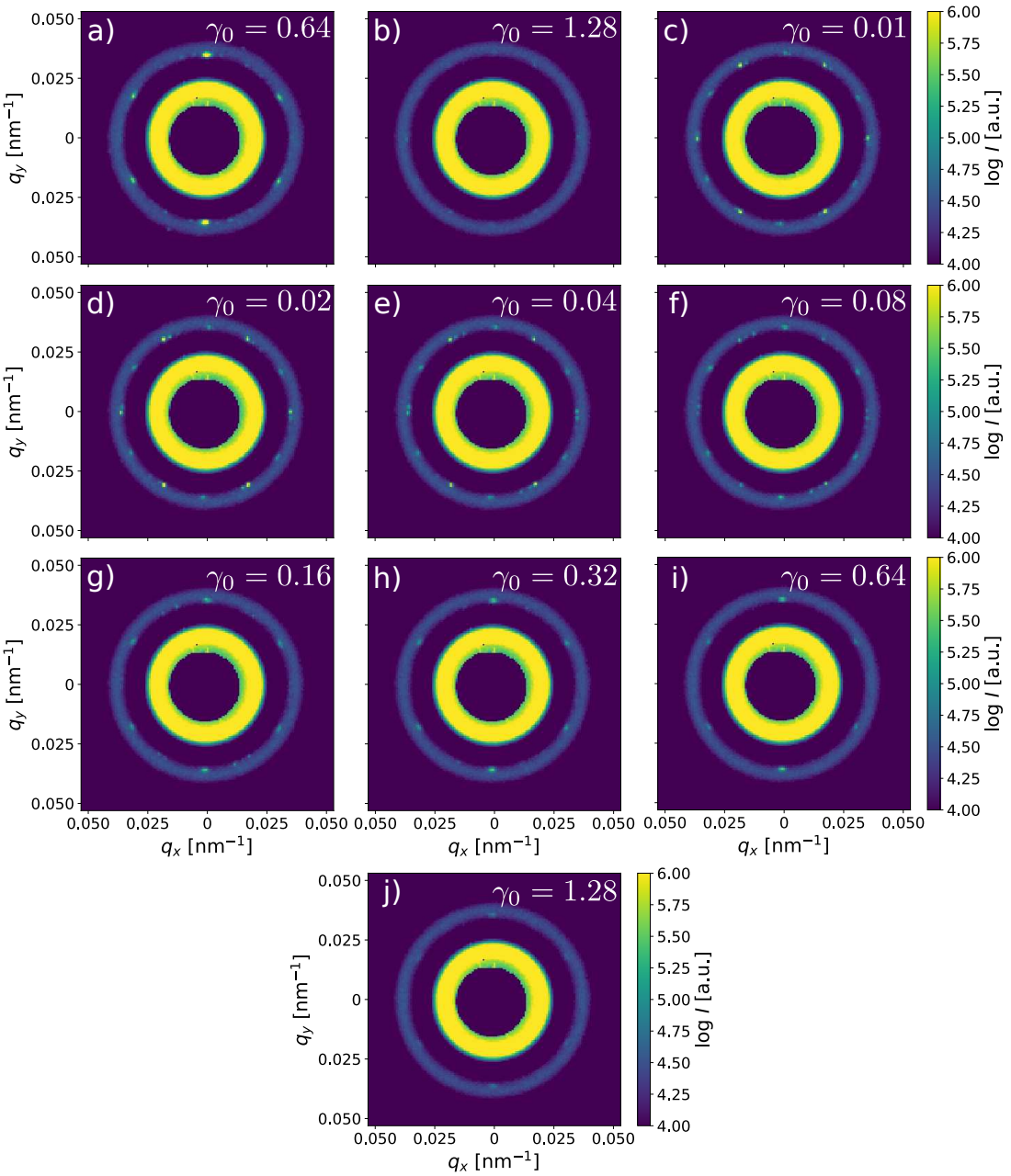

Figure 6.35: Scattering patterns of sample A after being deformed at amplitudes above $\gamma_0 = 0.32$. The patterns are taken in the first series of measurements but are respresentative for the second series, as well. Each scattering pattern is an average over five oscillation cycles at the specified deformations and the patterns are ordered in time.

When increasing the oscillation amplitude, additional Bragg reflections appear at the same scattering vector. The number of Bragg reflections increases up until a deformation of $\gamma_0 = 0.16$ (image g)) which indicates that until this point more and more close-packed layers form in the dispersion which are parallel but not oriented with respect to each other.

Starting from a deformation of $\gamma_0 = 0.32$ (image h)) the behavior is again the

same as seen previously, i. e. only one set of Bragg reflections with hexagonal symmetry can be observed. The hexagonal planes seem to orient themselves at this deformation amplitude. In addition, these reflections vanish once more at the same oscillation amplitude of $\gamma_0 = 1.28$ like described before.

In the following part, the degree of ordering of the sample is quantified using the results from the x-ray cross-correlation analysis. Analogous to the previous analysis at lower oscillation amplitudes, the variance of the sixth Fourier coefficient of the cross correlation function calculated at $q = 0.035$ nm^{-1} is observed as a function of the deformation γ_0. Figure 6.36 shows that for the first (left) and second (right) measurement series of sample A in the full range of measurements.

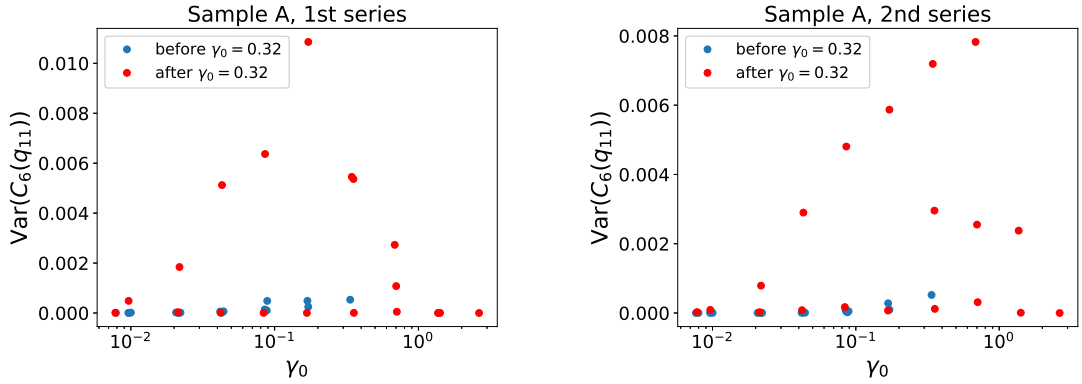

Figure 6.36: Variance of the sixth Fourier coefficient of the cross-correlation function of sample A as a function of deformation. Left: first measurement series; right: second measurement series. After reaching a deformation of $\gamma_0 = 0.32$, the variance of C_6 exhibits a different behavior, which is found for both series.

Figure 6.36 serves as an overview to display the overall difference in the behavior of the C_6 variance before, and after reaching an oscillation amplitude of $\gamma_0 = 0.32$ for the first time. For a more detailed analysis, γ_0 as well as the variance of C_6 are shown as a function of time and, additionally, cut into three time segments as shown in figure 6.37 - 6.39.

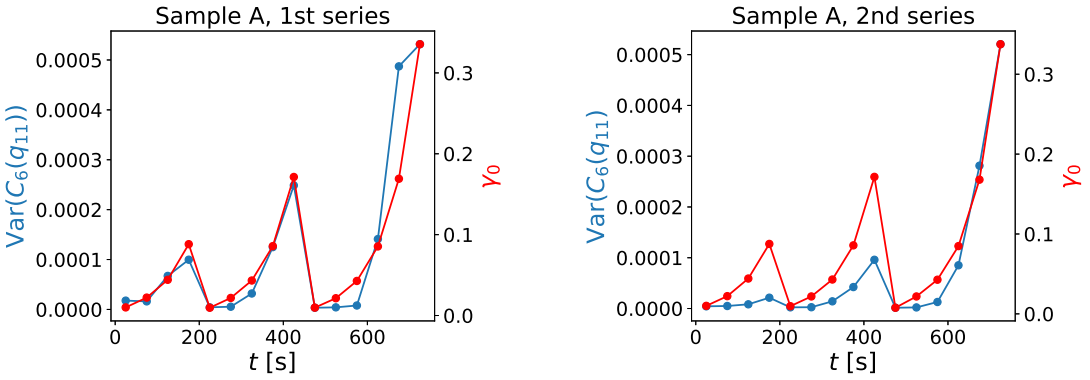

Figure 6.37: Variance of the sixth Fourier coefficient of the cross correlation function as well as the deformation as a function of time for sample A. Left: first measurement series; right: second measurement series. This figure shows the first time segment up until the deformation reaches $\gamma_0 = 0.32$ for the first time in the series.

Figure 6.37 illustrates the course of the variance of C_6 and the deformation as a function of time for the first time segment, in which the deformation does not exceed $\gamma_0 = 0.32$. This segment is discussed in detail in the previous section where the behavior of the sample at low oscillation amplitudes is considered. Overall, the variance of the Fourier coefficient C_6 increases nearly linearly with the deformation and no hysteresis effects are observed.

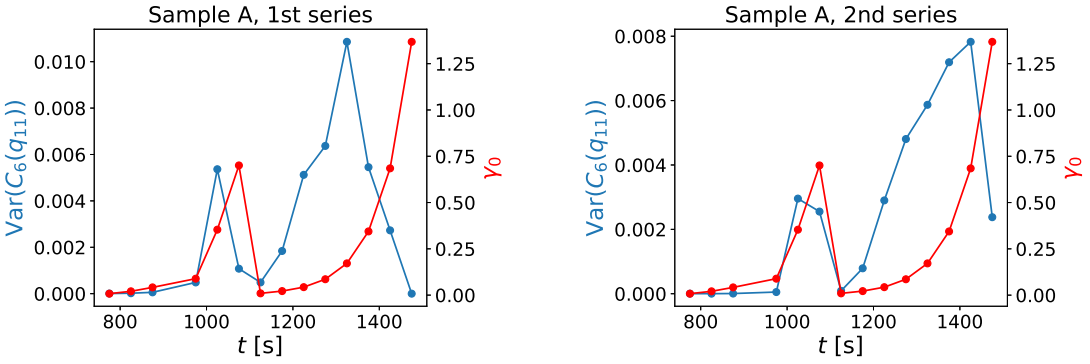

Figure 6.38: Variance of the sixth Fourier coefficient of the cross correlation function as well as the deformation as a function of time for sample A. Left: first measurement series; right: second measurement series. This figure shows the second time segment after the deformation reaches $\gamma_0 = 0.32$ for the first time in the series and before the last set of amplitude changes is performed.

Figure 6.38 shows the time segment of the measurement directly after the amplitude exceeds $\gamma_0 = 0.32$ for the first time. In the first series, until approximately $t = 1000$ s, the variance increases with increasing deformation and reaches a maximum at $\gamma_0 = 0.32$. At $\gamma_0 = 0.64$, the variance decreases and reaches a minimum again after the deformation is lowered to $\gamma_0 = 0.01$.

In the second series, the variance first starts to increase again, however, much faster than before. In this time segment, the scattering pattern becomes more powder-like, i. e. additional Bragg reflections can be observed at the same scattering vector q. The variance of C_6 then begins to drop sharply at a deformation of $\gamma_0 = 0.32$, in case of the first series, and $\gamma_0 = 1.28$ in case of the second series, respectively. The hexagonal close-packed layer structure of the sample is less and less pronounced at increasing amplitudes and vanishes completely at the highest deformations.

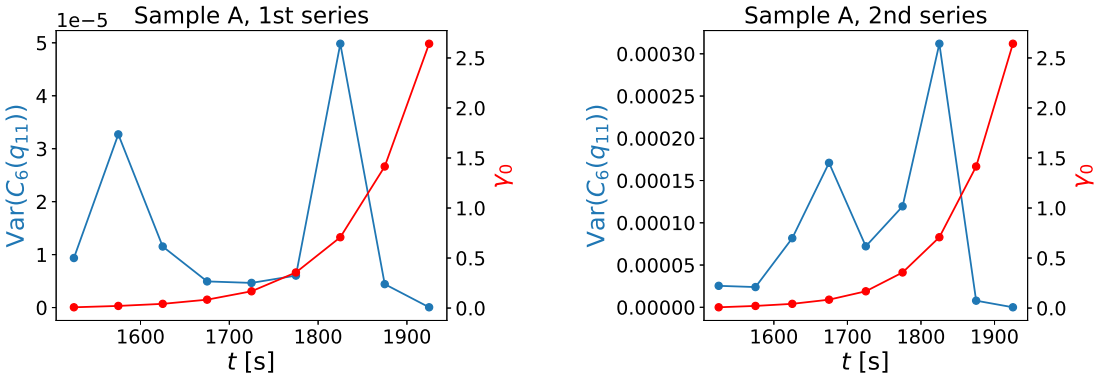

Figure 6.39: Variance of the sixth Fourier coefficient of the cross correlation function as well as the deformation as a function of time for sample A. Left: first measurement series; right: second measurement series. This figure shows the third time segment which contains the last set of amplitude changes of the series.

The time segment displayed in figure 6.39 shows the last set of increasing amplitudes of both series. It is separated from the illustration before, since the variance of the sixth Fourier coefficient is two (first series) or one (second series), respectively, orders of magnitude lower in the latter case. In both series, the overall observable behavior is quite similar: first, the variance of C_6 increases with increasing amplitude. Then, there is a drop (although happening at different oscillation amplitudes) and afterwards the maximum of the variance is reached at $\gamma_0 = 0.64$. Finally, the variance drops sharply and reaches zero at the highest deformation of $\gamma_0 = 2.56$.

To the best of the authors knowledge this behavior was not described before and at this point there is no explanation for the drop of the variance in the middle of this time segment. Also the overall lower variance of one or two orders of magnitude in the last segment cannot be explained yet. Since the intensity recorded at the detector is comparable to the measurements in the previous time segments, a loss of sample due to the high shear rates and corresponding low viscosities can be excluded. Since this effect is observed in the end of the experiment also aging effects could be discussed. One could expect evaporation of the dispersion medium over time but in that case this would lead to further concentration of the sample and, thus, an increasing viscosity which is not obvserved here.

Figure 6.40 shows the variance of the sixth Fourier coefficient of the cross-correlation of sample B calculated at the corresponding scattering vector $q =$

0.038 nm^{-1} where the Bragg reflections are visible. As a reminder, the sample is measured in a different way compared to sample A. Sample B is measured in distinct series of 20 seconds recorded with an exposure time of 0.1 seconds and 2000 images each. Each series is performed using the same deformation values as for sample A. The evaluation procedure is, however, the same for both samples so that only the results are shown for sample B here.

The findings are similar for sample B. The variance of C_6 increases roughly linearly with the deformation until a value of $\gamma_0 = 0.32$ is reached. At higher oscillation amplitudes, the six-fold symmetry of the scattering pattern disappeares completely.

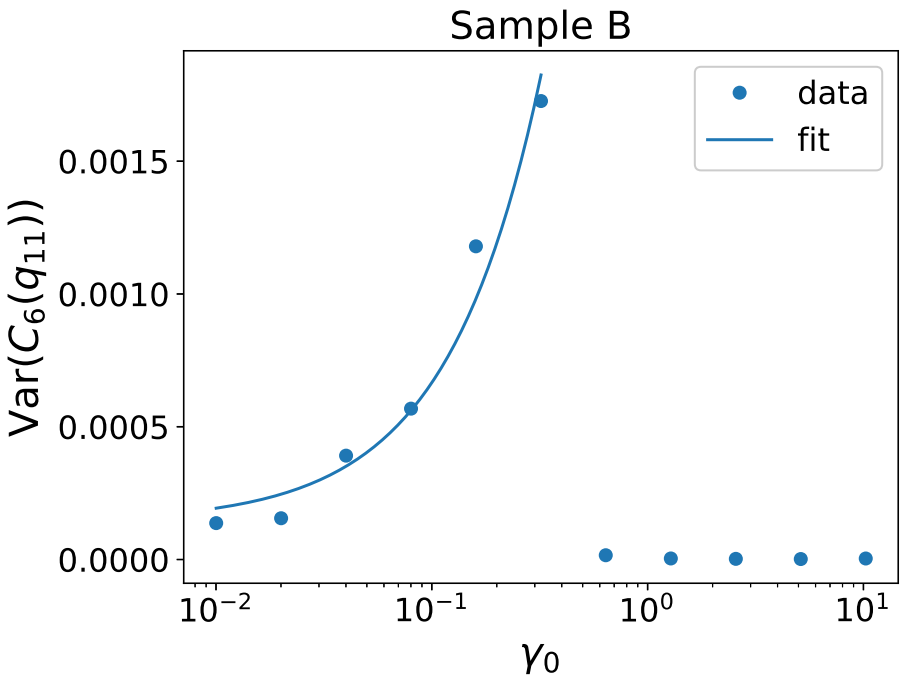

Figure 6.40: Variance of the sixth Fourier coefficient of the cross-correlation function as a function of deformation of sample B.

6.3 Sample at Low Volume Fraction

Sample C consists of monodisperse nanoparticles with a radius of 117 nm dispersed in PEG-200 with a volume fraction of 0.22. Although the size of the particles is similar to samples A and B, the volume fraction of sample C is less than half as high.

Like sample A, sample C is measured following the same protocol as described in section 5.4. The scattering pattern averaged over the first 1000 seconds is shown in figure 6.41.

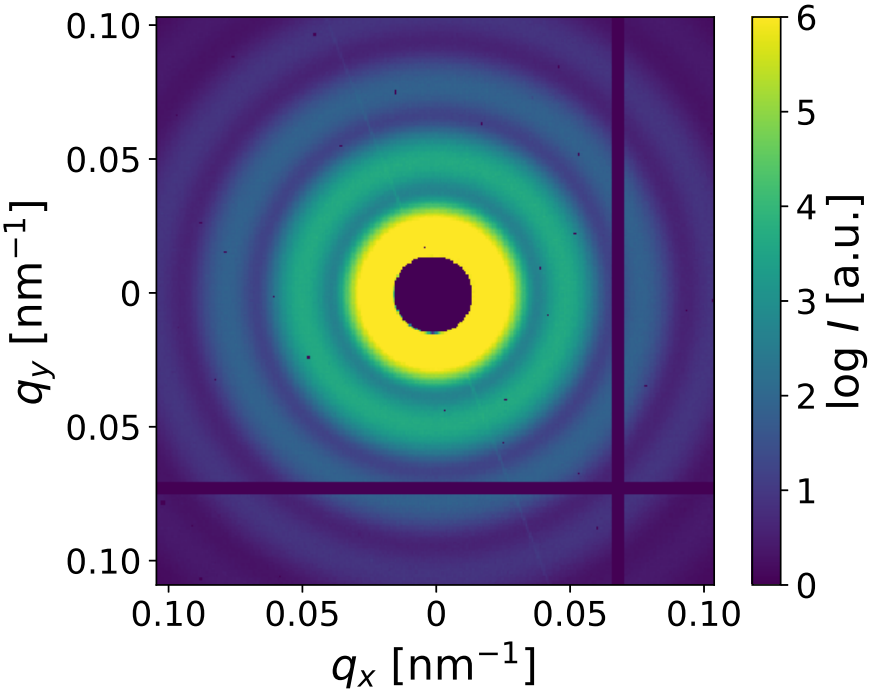

Figure 6.41: Scattering pattern of sample C under shear averaged over the first 1000 seconds of the rheology measurement.

In the average of 5000 scattering patterns, no Bragg reflections are observable. The pattern resembles the structure factor of the sample at rest. To find hidden symmetries that are not visible by eye, x-ray cross-correlation analysis is performed. Since no distinct feature is observable in the scattering pattern, no scattering vector of special interest can be determined to calculate the averaged Fourier coefficients of the cross-correlation function.

Therefore, the first three even Fourier coefficients, i. e. C_2, C_4, and C_6, respectively, are calculated and displayed with as a function of time t and scattering vector q. These distinct Fourier coefficients are chosen because, on the one hand, the x-ray scattering pattern is centrosymmetric according to Friedel's law and, thus, only even Fourier coefficients should be significant. On the other hand, in terms of close-packing structures, higher order symmetries are not expected to be present. The analyses of the Fourier coefficients are shown in figures 6.42 - 6.44.

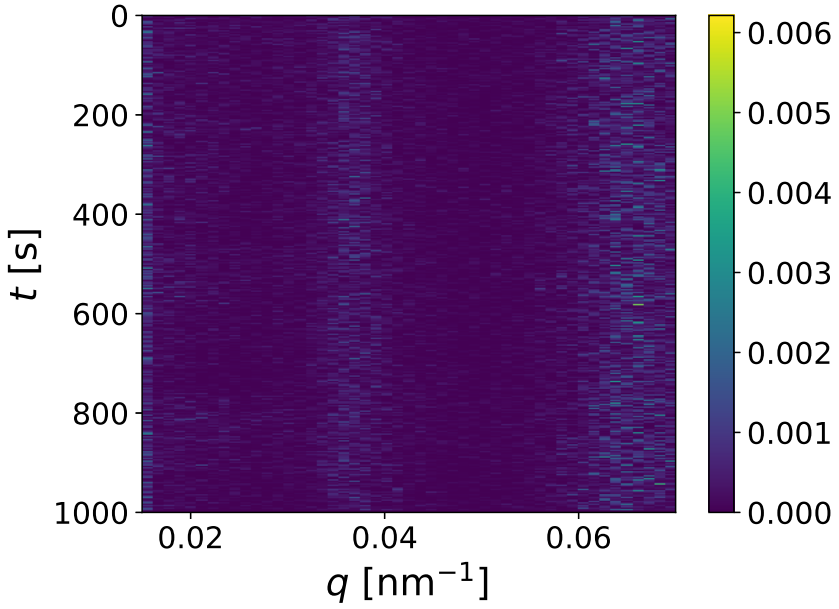

Figure 6.42: Second Fourier coefficient of the cross-correlation function C_2 of sample C.

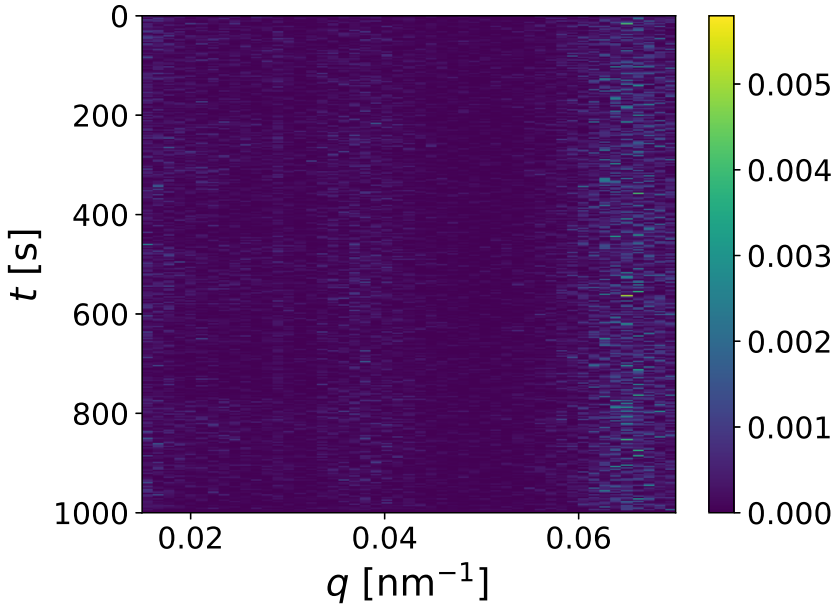

Figure 6.43: Fourth Fourier coefficient of the cross-correlation function C_4 of sample C.

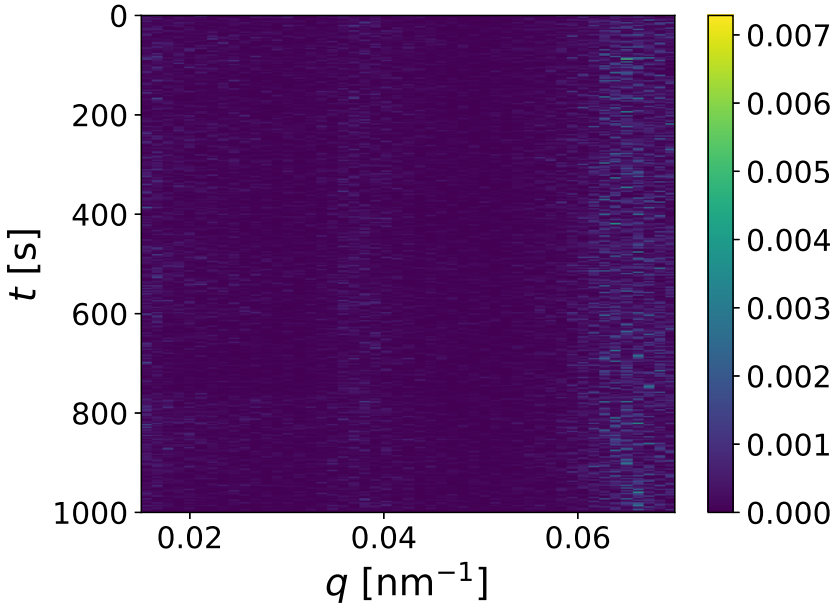

Figure 6.44: Sixth Fourier coefficient of the cross-correlation function C_6 of sample C.

No significant amplitudes of the Fourier coefficients can be observed in the figures above. However, the sample still shows the characteristic shear thinning behavior. The viscosity as a function of deformation is shown in figure 6.45. Again, the fits are calculated using the Ostwald-de Waele relationship described in equation (3.7). As before, two different fits are performed for low and high deformation amplitudes, respectively.

Even though the shear thinning behavior of sample C is observable by the rheology measurement, it should be noted that the initial viscosity is less than a tenth of the viscosity measured for samples A and B. The absolute difference of viscosities between the small deformation and the large deformation is, hence, minor compared to the previously discussed samples.

In addition, the low volume fraction could lead to comparably large interparticle distances inside the potential layer structure. In that way, the particles are not close-packed and, thus, show no hexagonal order and six-fold symmetry, respectively. In terms of the phase diagram (figure 2.2), this sample is deep in the liquid-like phase.

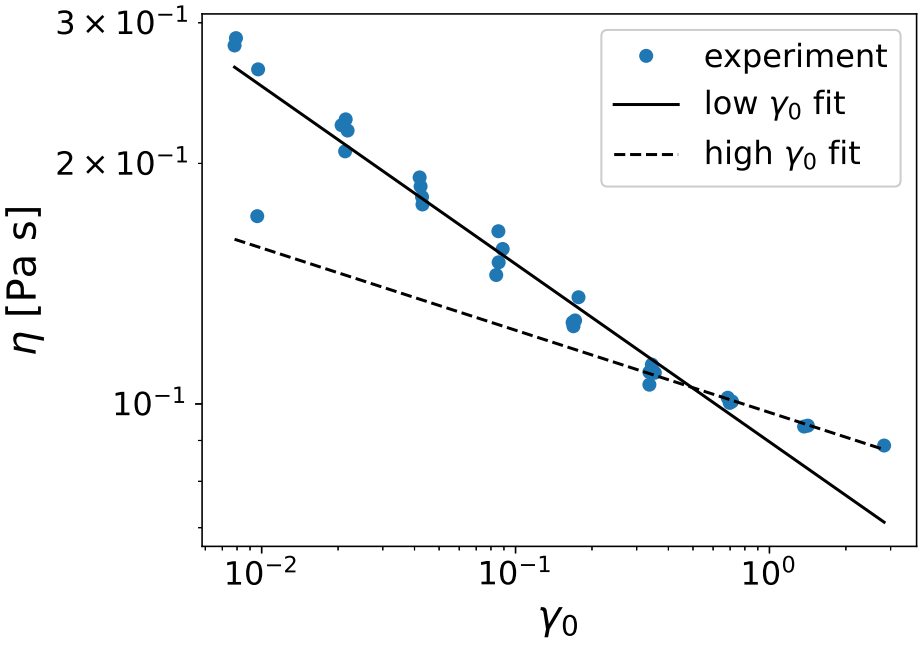

Figure 6.45: Viscosity of sample C as a function of deformation.

6.4 Discussion of the Results

As mentioned earlier, similar findings, compared to the ones presented here, were made in small-angle neutron scattering[1–5], light scattering[6–8], and small-angle x-ray scattering experiments[5,9] before and scattering patterns with hexagonal symmetry were observed for colloidal samples under shear. In contrast to this work, the colloidal samples discussed in these experiments were in a crystalline equilibrium state in the beginning of the rheology experiments. The samples were found to form crystallites which are oriented under shear and finally melt under intermediate shear rates. In this state, the samples form hexagonal close-packed layers sliding past each other and the viscosity of the sample decreases. At even higher shear rates this ordered layer structure breaks down and an amorphous, liquid-like, structure is observed which is accompanied by an increase of viscosity.

In comparison, in this work, the samples are in a liquid-like equilibrium state in the beginning of the experiments. Under shear, the samples become ordered forming hexagonal layers of close-packed spheres which can be observed by the emergence of the {11} Bragg reflection with six-fold symmetry corresponding to such structure. In the evaluation of sample D which forms a structure with oriented layers it is shown that the {11} reflection is the most intense. Hence, this reflection is the first one becoming visible while others remain buried under the liquid structure factor of the sample. A possible explanation for the varying intensity of this reflection is the growth of the layers under shear, i. e. layers of close-packed spheres start forming already at low shear rates and the thickness of the layers is increasing with increasing shear rate. Likewise, the decreasing shear rate leads to a decrease of layer thickness and, thus, a decrease of intensity of the {11} reflection. This behavior is resolved over time and quantified by the

sixth Fourier coefficient of the cross-correlation functions calculated using x-ray cross-correlation analysis.

Under the influence of low shear rates, only one or two sets of six-fold Bragg reflections, respectively, can be observed. One can assume that, likely, the layer structure starts forming at the surfaces of the plate or the cone of the shear cell, respectively. In case of the formation at both surfaces simultaneously, the layers are not necesseraly oriented to each other which leads to the occurence of a second set of {11} Bragg reflections, which is still of hexagonal symmetry but rotated in the detector plane.

At higher shear rates, additional sets of {11} reflections can be observed which leads to a more and more powder-like scattering pattern. This can be interpreted as the independent formation of multiple layers between the layers at the shear cell surfaces. While the surfaces could facilitate an initial layer formation, the gradient of shear is constant over the whole rheometer gap so that the emergence of additional layers is equally likely over the sample volume. As these layers would form independently, no preferred orientation is expected between them. In case of sample D, however, it can be seen that the layers can be oriented by applying rotational shear at a high shear rate for a short amount of time.

The increase of the number of close-packed layers sliding past each other leads to less internal friction in the sample. This is macroscopically reflected by the decrease of the viscosity, i. e. shear thinning behavior.

Analogous to the results discussed in the literature mentioned at the beginning of this section, also in this work it was found that at the highest shear rates, the hexagonal structure of the samples vanishes. In case of samples A and B, the hexagonal symmetry of the scattering pattern starts to disappear when the amplitude exceeds 0.32, i. e. when the maximum shear rate is higher than 0.2 s^{-1}. The layer structure cannot be retained at these shear rates. Interestingly, the viscosity of the samples decreases further in the same manner as observed for lower shear rates and shear-thickening behavior, which is usually explained as the result of particles jamming each other, as discussed for example in [9], cannot be observed. It could be, that in the framework of this thesis, the shear rate necessary to induce shear-thickening is not reached. Since this shear rate depends on the specific parameters of the individual sample, no definitive answer can be given. The hexagonal layer structure could, for instance, transition into a structure of co-flowing strings which could be observed in liquid microjet experiments[38]. Such structure could still minimize internal friction and, as a result, decrease the viscosity, while no features of hexagonal symmetry would be expected in the scattering pattern.

The fact, that non of the above features could be observed for sample C, is likely due to the comparably low volume fraction. Since shear thinning is nonetheless occuring for this sample, one could still assume the formation of a layered structure. One possible reason for the absence of an observable hexagonal symmetry in the scattering pattern could be that the inter-particle distances in a potential layer would be larger compared to the other samples. As a result, the particles would be far from beeing in contact distance to each other and no close-packed, hexagonal, structure would emerge. As a consequence, no hexagonal Bragg reflections would be observable.

7 Conclusion and Outlook

In this work, the structural changes of nanoparticle dispersions accompanying shear-thinning behavior were investigated using a combination of rheology, small-angle x-ray scattering (SAXS), and x-ray cross-correlation analysis (XCCA). The experiments were carried out at the coherence application beamline P10 of the storage ring PETRA III at DESY in Hamburg, Germany. A unique, vertical rheoSAXS setup was used to collect x-ray scattering data in situ while applying oscillatory shear to the sample in a cone-plate rheometer geometry.

Spherical, colloidal, silica nanoparticles were prepared using the Stöber method [31] and coated with a poly-acrylate layer. The particles were dispersed in PEG-200 with volume fractions varying from $\phi = 0.22$ to $\phi = 0.53$ and characterized by dynamic light scattering, transmission electron microscopy, and SAXS.

It could be shown that the higly concentrated colloidal dispersions undergo a transition from a liquid-like ordered equilibrium state at rest to a two-dimensional hexagonal layer structure under the influence of shear. While the occurence of such structures was discussed in the literature previously [1–15], in this thesis the effect could be time-resolved and quantified for the first time. Therefore, the SAXS data was evaluated using XCCA. By evaluating the sixth Fourier coefficient calculated from the cross-correlation functions from the XCCA results over time and comparing it with the shear rate applied to the sample, it was demonstrated that the degree of hexagonal order oscillates with the shear rate.

An increasing shear rate is accompanied by an increase of the sixth Fourier coefficient of the x-ray cross-correlation evaluated at the scattering vector where the $\{11\}$ Bragg reflection of a two-dimensional hexagonal layer structure was observed. The variance of the Fourier coefficient was calculated for time segments of the same shear deformation as a measure of the average degree of hexagonal order. It was shown that the variance increases nearly linearly with the shear deformation in the regime of low deformations. In the regime of high shear deformations, the hexagonal order disappeared.

The rheological measurements showed a shear-thinning behavior for all samples investigated, i. e. the viscosity decreased with increasing shear deformations. Comparing this rheological result with the structural findings from the x-ray scattering data, leads to the final conclusion: The higher the deformation, and, thus, the higher the shear rate, the larger the variance of the sixth Fourier coefficient and the lower the viscosity of the sample. Thus, more two-dimensional, hexagonal close-packed, layers form within the dispersion with increasing shear rates which minimize internal friction in the dispersions, reflected by the decrease of the viscosity.

As discussed above, in case of high shear rates the hexagonal order vanishes. This would be expected since the jamming of particles is often observed under the influence of high shear rates [9,15]. This is, however, accompanied by a shear thickening behavior. In this thesis, the samples still display shear thinning without showing hexagonal order which was not observed before. As stated before, a possible explanation could be the formation co-flowing strings in the dispersion. That kind of behavior could be observed recently in liquid microjet experiments [38].

For future experiments it would be interesting to investigate the influence of the volume fraction and the particle size on the order formation and the rheological behavior. A significant difference in the behavior was observed between the samples A and B on the one hand and sample D on the other hand. Whether or not this difference is caused by the different concentrations or the different particle sizes could not completely be verified.

The second notable difference could be seen between the samples with intermediate volume fraction (samples A and B) and low volume fraction (sample C). While the former ones show structure formation through the occurence of Bragg reflections with hexagonal order in the SAXS patterns the latter one does not. Investigating samples with volume fractions in between would be necessary to further explore the limits of the XCCA approach in a rheoSAXS setup.

List of Figures

List of Tables

Bibliography

[1] B. J. Ackerson, J. B. Hayter, N. A. Clark, and L. Cotter. Neutron scattering from charge stabilized suspensions undergoing shear. *J. Chem. Phys*, 84:2344, 1986.

[2] S. Ashdown, I. Markovic, R. H. Ottewill, P. Lindner, R. C. Oberthür, and A. R. Rennie. Small-Angle Neutron-Scattering Studies on Ordered Polymer Colloid Dispersions. *Langmuir*, 6:303, 1990.

[3] H. Versmold. Neutron Diffraction from Shear Ordered Colloidal Dispersions. *Phys. Rev. Lett.*, 75:763, 1995.

[4] C. Dux, S. Musa, V. Reus, H. Versmold, D. Schwahn, and P. Lindner. Small angle neutron scattering experiments from colloidal dispersions at rest and under sheared conditions. *J. Chem. Phys.*, 109:2556, 1998.

[5] H. Versmold, S. Musa, C. Dux, P. Lindner, and V. Urban. Shear-Induced Structure in Concentrated Dispersions: Small Angle Synchrotron X-ray and Neutron Scattering. *Langmuir*, 17:6812, 2001.

[6] B. J. Ackerson and P. N. Pusey. Shear-Induced Order in Suspensions of Hard Spheres. *Phys. Rev. Lett.*, 61:1033, 1988.

[7] C. Dux and H. Versmold. Shear induced structures in charge stabilized colloidal dispersions. *Physica A*, 235:75, 1997.

[8] C. Dux and H. Versmold. Light Diffraction from Shear Ordered Colloidal Dispersions. *Phys. Rev. Lett.*, 78:1811, 1997.

[9] J. Lee, Z. Jiang, J. Wang, A. R. Sandy, and S. Narayanan. Unraveling the Role of Order-to-Disorder Transition in Shear Thickening Suspensions. *Phys. Rev. Lett.*, 120:028002, 2018.

[10] H. Versmold and P. Lindner. Reinterpretation of Small-Angle Neutron-Scattering Studies on Ordered Colloid Dispersions. *Langmuir*, 10:3043, 1994.

[11] W. Loose and B. J. Ackerson. Model calculations for the analysis of scattering data from layered structures. *J. Chem. Phys.*, 101:7211, 1994.

[12] H. Versmold, S. Musa, and C. Dux. On the Structure of Shear-Ordered Colloidal Dispersions: Bragg-Rod Intensity Distribution. *Langmuir*, 15:5065, 1999.

[13] H. Versmold, C. Dux, and S. Musa. On the Structure of Charge Stabilized Polymer Dispersions. *J. Mol. Liq.*, 98-99:145, 2002.

[14] C.-T. Liao, Y.-F. Wu, W. Chien, J.-R. Huang, and Y.-L. Chen. Modeling shear-induced particle ordering and deformation in a dense soft particle suspension. *J. Phys.: Condens. Matter*, 29:435101, 2017.

[15] F. Khabaz, M. Cloitre, and R. T. Bonnecaze. Structural state diagram of concentrated suspensions of jammed soft particles in oscillatory shear flow. *Phys. Rev. Fluids*, 3:033301, 2018.

[16] P. Wochner, C. Gutt, T. Autenrieth, T. Demmer, V. Bugaev, A. Diaz-Ortiz, A. Duri, F. Zontone, G. Grübel, and H. Dosch. X-ray cross correlation analysis uncovers hidden local symmetries in disordered matter. *Proc. Natl. Acad. Sci.*, 106:11511, 2009.

[17] P. Wochner, M. Castro-Collins, S. N. Bogle, and V. N. Bugaev. Of fluctuations and cross-correlations: finding order in disorder. *Int. J. Mat. Res.*, 102:7, 2011.

[18] A. D. MacNaught and A. Wilkinson. *IUPAC. Compendium of Chemical Terminology (the "Gold Book").* Blackwell Scientific Publications, 2nd edition, 1997.

[19] R. Eisenschitz and F. London. Über das Verhältnis der van der Waalschen Kräfte zu den homöpolaren Bindungskräften. *Z. Physik*, 60:491, 1930.

[20] F. London. Zur Theorie und Systematik der Molekularkräfte. *Z. Physik*, 63:245, 1930.

[21] F. London. The General Theory of Molecular Forces. *Trans. Faraday Soc.*, 33:8, 1937.

[22] H. C. Hamaker. The London-Van-der-Waals Attraction Between Spherical Particles. *Physica IV*, (10):1058, 1937.

[23] H. Löwen. Possibilities of phase separation in colloidal suspensions. *Physica A*, 235:129, 1997.

[24] H. Löwen. Melting, freezing and colloidal suspensions. *Phys. Rep.*, 237(5):249, 1994.

[25] G. L. Hunter and E. R Weeks. The physics of the colloidal glass transition. *Rep. Prog. Phys.*, 75:066501, 2012.

[26] G. Nägele. On the dynamics and structure of charge-stabilized suspensions. *Phys. Rep.*, 272:215, 1996.

[27] B. Derjaguin and L. Landau. Theory of the Stability of Strongly Charged Lyophobic Sols and of the Adhesion of Strongly Charged Particles in Solutions of Electrolytes. *Acta Phys. Chim. URSS*, 14:30, 1941.

[28] E. J. W. Verwey and J. T. G. Overbeek. *Theory of the Stability of Lyophobic Colloids. The Interaction of Sol Particles Having an Electric Double Layer.* Elsevier, 1948.

[29] E. B. Sirota, H. D. Ou-Yang, S. K. Sinha, and P. M. Chaikin. Complete Phase Diagram of a Charged Colloidal System: A Synchrotron X-Ray Scattering Study. *Phys. Rev. Lett.*, 62:1524, 1989.

[30] I. Ab Rahman and V. Padavettan. Synthesis of Silica Nanoparticles by Sol-Gel: Size-Dependent Properties, Surface Modification, and Applications in Silica-Polymer Nanocomposites - A review. *Journal of Nanomaterials*, 2012:1687, 2012.

[31] W. Stöber and A. Fink. Controlled Growth of Monodisperse Silica Spheres in the Micron Size Range. *J. Colloid Interface Sci.*, 26:62, 1968.

[32] G. H. Bogush, M. A. Tracy, and C.F. Zukoski IV. Preparation of Monodisperse Silica Particles: Control of Size and Mass Fraction. *J. Non-Cryst. Solids*, 104:95, 1988.

[33] T. Matsoukas and Erdogan Gulari. Dynamics of Growth of Silica Particles from Ammonia-Catalyzed Hydrolaysis of Tetra-ethyl-orthosilicate. *J. Colloid Interface Sci.*, 124:252, 1988.

[34] C. W. Macosko. *Rheology: Principles, Measurements, and Applications.* Wiley-VCH, 1994.

[35] R. G. Larson. *The Structure and Rheology of Complex Fluids.* Oxford University Press, 1999.

[36] F. Lehmkühler, I. Steinke, M. A. Schroer, B. Fischer, M. Sprung, and G. Grübel. Microsecond Structural Rheology. *J. Phys. Chem. Lett.*, 8:3581, 2017.

[37] J. Schulz, J. Bielecki, R. B. Doak, K. Dörner, R. Graceffa, R. L. Shoeman, M. Sikorski, P. Thute, D. Westphal, and A. P. Mancuso. A versatile liquid-jet setup for the European XFEL. *J. Synchrotron Radiat.*, 26:339, 2019.

[38] V. Markmann, M. Dartsch, J. Valerio, L. Frenzel, I. Lokteva, M. Walther, F. Westermeier, G. Grübel, and F. Lehmkühler. Shear-induced ordering in liquid microjets seen by x-ray cross correlation analysis. *Struct. Dyn.*, 7:054901, 2020.

[39] W. Ostwald. Ueber die rechnerische Darstellung des Strukturgebietes der Viskosität. *Kolloid-Zeitschrift*, 47:176, 1929.

[40] W. C. Röntgen. Über eine neue Art von Strahlen. *Sitzungsberichte der Würzburger Physik.-medic. Gesellschaft*, 1896.

[41] J. D. Watson and F. H. C. Crick. Molecular Structure of Nucleic Acids - A Structure for Deoxyribose Nucleic Acid. *Nature*, 171:737, 1953.

[42] J. C. Kendrew, G. Bodo, H. M. Dintzis, R. G. Parrish, and H. Wyckoff. A Three-Dimensional Model of the Myoglobin Molecule Obtained by X-Ray Analysis. *Nature*, 181:662, 1958.

[43] J. Moonen, C. Pathmamanoharan, and A. Vrij. Small-angle X-ray scattering of silica dispersions at low particle concentrations. *J. Colloid Interface Sci.*, 131:349, 1989.

[44] G. Walter, R. Kranold, and U. Lembke. Small-Angle X-ray Scattering of Inorganic Glasses. Data Treatment and Analysis. *J. Apll. Cryst.*, 30:1048, 1997.

[45] J. Als-Nielsen and D. McMorrow. *Elements of Modern X-ray Physics*. John Wiley & Sons, 2011.

[46] R. Borsali and R. Pecora, editors. *Soft-Matter Characterization*. Springer, 2008.

[47] B. J. Berne and R. Pecora. *Dynamic Light Scattering*. Dover Publications, Inc., 2000.

[48] S. R. Aragon and R. Pecora. Theory of dynamic light scattering from polydisperse systems. *J. Chem. Phys.*, 64:2395, 1976.

[49] B. H. Zimm. The Scattering of Light and the Radial Distribution Function of High Polymer Solutions. *J. Chem. Phys.*, 16:1093, 1948.

[50] G. V. Schulz. Über die Kinetik der Kettenpolymerisationen V. *Z. Phys. Chem. B*, 43:25, 1939.

[51] P. J. Flory. Molecular Size Distribution in Linear Condensation Polymers. *J. Am. Chem. Soc.*, 58:1877, 1936.

[52] T. Li, A. J. Senesi, and B. Lee. Small Angle X-ray Scattering for Nanoparticle Research. *Chem. Rev.*, 116:11128, 2016.

[53] J. S. Pedersen. Analysis of small-angle scattering data from colloids and polymer solutions: modeling and least-squares fitting. *Adv. Colloid Interface Sci.*, 70:171, 1997.

[54] L. S. Ornstein and F. Zernike. Accidental deviations of density and opalescence at the critical point of a single substance. *Proc. Acad. Sci. Amsterdam*, 17:793, 1914.

[55] J. L . Lebowitz and J. K. Percus. Mean Spherical Model for Lattice Gases with extended Hard Cores and Continuum Fluids. *Phys. Rev.*, 144:251, 1966.

[56] J. B. Hayter and J. Penfold. An analytic struture factor for macroion solutions. *Mol. Phys.*, 42:109, 1981.

[57] J.-P. Hansen and J. B. Hayter. A rescaled MSA structure factor for dilute charged colloidal dispersions. *Mol. Phys.*, 46:651, 1982.

[58] J. M. J. van Leeuwen, J. Groeneveld, and J. de Boer. New method for the calculation of the pair correlation function. *Physica*, 25:792, 1959.

[59] J. K. Percus and G. J. Yevick. Analysis of Classical Statistical Mechanics by Means of Collective Coordinates. *Phys. Rev.*, 110:1, 1957.

[60] M. S. Wertheim. Excact Solution of the Percus-Yevick Integral Equation for Hard Spheres. *Phys. Rev. Lett.*, 10:321, 1963.

[61] Z. Kam. Determination of Macromolecular Structure in Solution by Spatial Correlation of Scattering Fluctuations. *Macromolecules*, 10:927, 1977.

[62] D. K. Saldin, V. L. Shneerson, R. Fung, and A. Ourmazd. Structure of isolated biomolecules obtained from ultrashort x-ray pulses: exploiting the symmetry of random orientations. *J. Phys.: Condens. Matter*, 21:134014, 2009.

[63] M. Altarelli, R. P. Kurta, and I. A. Vartanyants. X-ray cross-correlation analysis and local symmetries of disordered systems: General theory. *Phys. Rev. B.*, 82:104207, 2010.

[64] D. K. Saldin, H. C. Poon, V.L. Shneerson, M. Howells, H.N. Chapman, R. A. Kirian, K. E. Schmidt, and J. C. H. Spence. Bayond small-angle x-ray scattering: Exploiting angular correlations. *Phys. Rev. B*, 81:174105, 2010.

[65] F. Lehmkühler, G. Grübel, and C. Gutt. Detecting orientational order in model systems by X-ray cross-correlation methods. *J. Appl. Cryst.*, 47:1315, 2014.

[66] T. Latychevskaia, G. F. Mancini, and F. Carbone. The role of the coherence in the cross-correlation analysis of diffraction patterns from two-dimensional dense mono-disperse systems. *Sci. Rep.*, 5:16573, 2015.

[67] F. Lehmkühler, B. Fischer, L. Müller, B. Ruta, and G. Grübel. Structure beyond pair correlations: X-ray cross-correlation from colloidal crystals. *J. Appl. Cryst.*, 49:2046, 2016.

[68] M. A. Schroer, C. Gutt, and G. Grübel. Characteristics of angular cross correlations studied by light scattering from two-dimensional miscrosphere films. *Phys. Rev. E*, 90:012309, 2014.

[69] M. A. Schroer, C. Gutt, F. Lehmkühler, B. Fischer, I. Steinke, F. Westermeier, M. Sprung, and G. Grübel. Nano-beam X-ray microscopy of dried colloidal films. *Soft Matter*, 11:5465, 2015.

[70] F. Lehmkühler, F. Schulz, M. A. Schroer, L. Frenzel, H. Lange, and G. Grübel. Heterogeneous local order in self-assembled nano-particle films revealed by X-ray cross-correlations. *IUCrJ*, 5:354, 2018.

[71] F. Lehmkühler, F. Schulz, M. A. Schroer, L. Frenzel, H. Lange, and G. Grübel. Local orientational order in self-assembled nanoparticle films: the role of ligand composition and salt. *J. Appl. Cryst.*, 52:777, 2019.

[72] I. A. Zaluzhnyy, R. P. Kurta, A. P. Menushenkov, B. I. Ostrovskii, and I. A. Vartanyants. Direct reconstruction of the two-dimensional pair distribution function in partially ordered systems with angular correlations. *Phys. Rev. E*, 94:030701, 2016.

[73] I. A. Zaluzhnyy, R. P. Kurta, E. A. Sulyanova, O. Yu. Gorobtsov, A. G. Shabalin, A. V. Zozulya, A. P. Menushenkov, M. Sprung, A. Krowczynski, E. Gorecka, B. I. Ostrovskii, and I. A. Vartanyants. Structural studies of the bond-orientational order and hexatic–smectic transition in liquid crystals of various compositions. *Soft Matter*, 13:3240, 2017.

[74] I. Lokteva, M. Koof, M. Walther, G. Grübel, and F. Lehmkühler. Coexistence of hcp and bct Phases during In Situ Superlattice Assembly from Faceted Colloidal Nanocrystals. *J. Phys. Chem. Lett.*, 10:6331, 2019.

[75] I. Lokteva, M. Koof, M. Walther, G. Grübel, and F. Lehmkühler. Monitoring Nanocrystal Self-Assembly in Real Time Using In Situ Small-Angle X-Ray Scattering. *Small*, 15:1900438, 2019.

[76] D. K. Saldin, H. C. Poon, M. J. Bogan, S. Marchesini, D. A. Shapiro, R. A. Kirian, U. Weierstall, and J. C. H. Spence. New Light on Disordered Ensembles: Ab Initio Structure Determination of One Particle from Scattering Fluctuations of Many Copies. *Phys. Rev. Lett.*, 106:115501, 2011.

[77] G. Chen, M. A. Modestino, B. K. Poon, A.Schirotzek, S. Marchesini, R. A. Segalman, A. Hexemer, and P. H. Zwart. Structure determination of Pt-coated Au dumbbells via fluctuation X-ray scattering. *J. Synchrotron Rad.*, 19:695, 2012.

[78] D. Starodub, A. Aquila ans S. Bajt, M. Barthelmess, A. Barty, C. Bostedt, J. D. Bozek, N. Coppola, R. B. Doak, S. W. Epp, B. Erk, F. Foucar, L. Gumprecht, C. Y. Hampton, A. Hartmann, R. Hartmann, P. Holl, S. Kassemeyer, N. Kimmel, H. Laksmono, M. Liang, N. D. Loh, L. Lomb, A. V. Martin, K. Nass, C. Reich, D. Rolles, B. Rudek, A. Rudenko, J. Schulz, R. L. Shoeman, R. G. Sierra, H. Soltau, J. Steinbrener, F. Stellato, S. Stern, G. Weidenspointner, M. Frank, J. Ullrich, L. Strüder, I. Schlichting, H.N. Chapman, J. C. H. Spence, and M. J. Bogan. Single-particle structure determination by correlations of snapshot X-ray diffraction patterns. *Nat. Commun.*, 3:1276, 2012.

[79] B. Pedrini, A. Menzel, M. Guizar-Sicairos, V. A. Guzenko, S. Gorelick, C. David, B. D. Patterson, and R. Abela. Two-dimensional structure from random multiparticle X-ray scattering images using cross-correlations. *Nat. Commun.*, 4:1647, 2013.

[80] N. Wiener. Generalized harmonic analysis. *Acta Math.*, 55:117, 1930.

[81] A. Chintchin. Korrelationstheorie der stationären stochastischen Prozesse. *Mathematische Annalen*, 109:604, 1934.

[82] A. Einstein. Über die von der molekularkinetischen Theorie der Wärme geforderte Bewegung von in rruhenden Flüssigkeiten suspendierten Teilchen. *Annalen der Physik*, 322:549, 1905.

[83] D. E. Koppel. Analysis of Macromolecular Polydispersity in Intensity Correlation Spectroscopy: The Method of Cumulants. *J. Chem. Phys.*, 57:4814, 1972.

[84] J. Hadamard. Sur les problèmes aux dérivés partielles et leur signification physique. *Princeton University Bulletin*, 13:49, 1902.

[85] B. J. Frisken. Revisiting the method of cumulants for the analysis of dynamic light-scattering data. *Applied optics*, 40:4087, 2001.

[86] S. W. Provencher. A Constrained Regularization Method for Inverting Data Represented by Linear Algebraic or Integral Equations. *Comput. Phys. Commun.*, 27:213, 1982.

[87] S. W. Provencher. CONTIN: A General Purpose Constrained Regularization Program for Inverting Noisy Linear Algebraic and Integral Equations. *Comput. Phys. Commun.*, 27:229, 1982.

[88] A. N. Tikhonov and V. Y. Arsenin. *Solution of Ill-posed Problems*. Winston & Sons, 1977.

[89] E. Stellamanns, D. Meissner, M. Lohmann, and B. Struth. A Unique Rheology / SAXS Combination at DESY / PETRA III. *J. Phys.: Conf. Ser.*, 425:202007, 2013.

[90] D. Pennicard, S. Lange, S. Smoljanin, H. Hirsemann, and H. Graafsma. LAMBDA - Large Area Medipix3-Based Detector Array. *J. Instrum.*, 7:C11009, 2012.

[91] F. Schulz, F. Westermeier, F. Dallari, V. Markmann, H. Lange, G. Grübel, and F. Lehmkühler. Plasmonic Supercrystals with a Layered Structure Studied by a Combined TEM-SAXS-XCCA Approach. *Adv. Mater. Interfaces*, 7:2000919, 2020.

Publications

1. L. Frenzel, M. Dartsch, G. Marti Balaguer, F. Westermeier, G. Grübel and F. Lehmkühler. Glass-liquid and glass-gel transitions of soft-shell particles. *Phys. Rev. E*, 104:L012602, 2021.

2. I. Lokteva, M. Dartsch, F. Dallari, F. Westermeier, M. Walther, G. Grübel and F. Lehmkühler. Real-Time X-ray Scattering Discovers Rich Phase Behavior in PbS Nanocrystal Superlattices during In Situ Assembly. *Chem. Mater.*, 13:6553, 2021.

3. F. Lehmkühler, F. Dallari, A. Jain, M. Sikorski, J. Möller, L. Frenzel, I. Lokteva, G. Mills, M. Walther, H. Sinn, F. Schulz, M. Dartsch, V. Markmann, R. Bean, Y. Kim, P. Vagovic, A. Madsen, G. Grübel and A. Mancuso. Emergence of Anomalous Dynamics in soft matter probed at the European XFEL. *Proc. Natl. Acad. Sci. U.S.A.*, 117:24110, 2020.

4. V. Markmann, M. Dartsch, J. Valerio, L. Frenzel, I. Lokteva, M. Walther, F. Westermeier, G. Grübel and F. Lehmkühler. Shear-induced ordering in liquid microjets seen by x-ray cross-correlation analysis. *Struct. Dyn.*, 7:054901, 2020.

5. L. Frenzel, F. Lehmkühler, M. Koof, I. Lokteva and G. Grübel. The Phase Diagram of Colloidal Silica-PNIPAm core-shell Nanogels. *Soft Matter*, 16:466, 2020.

6. L. Frenzel, I. Lokteva, M. Koof, S. Narayanan, G. Grübel and F. Lehmkühler. Influence of TMAO as co-solvent on the gelation of silica-PNIPAm core-shell nanogels at intermediate volume fractions. *ChemPhysChem*, 21:1318, 2020.

7. I. Lokteva, M. Walther, M. Koof, G. Grübel and F. Lehmkühler. In situ small-angle X-ray scattering environment for studying nanocrystal self-assembly upon controlled solvent evaporation. *Rev. Sci. Instrum.*, 90:036103, 2019.

8. I. Lokteva, M. Koof, M. Walther, G. Grübel and F. Lehmkühler. Monitoring Nanocrystal Self-Assembly in Real Time Using In Situ Small-Angle X-Ray Scattering. *Small*, 15:1900438, 2019.

9. I. Lokteva, M. Koof, M. Walther, G. Grübel and F. Lehmkühler. Coexistence of hcp and bct Phases during In Situ Superlattice Assembly from Faceted Colloidal Nanocrystals. *J. Phys. Chem. Lett.*, 10:6331, 2019.

Acknowledgements

I would like to acknowledge all the people that helped me on my way to create this work and made this whole project possible.

First of all, I would like to thank my supervisor Gerhard Grübel. Thank you for your invaluable support, your guidance and your trust in me, especially during tough times. I am glad that I could be a part of your group and work in such a stimulating, friendly, and supportive environment.

I also want to thank Arwen Pearson who supported me as my co-supervisor. Particularly during the beginning of my thesis you gave me a lot of fruitful advice and suggestions on how to solve my scientific problems.

I would like to express my sincere thanks to Felix Lehmkühler. You taught me a lot during my time in this group and supported me at all stages of my work. You were a guide in many ways and took a huge part in my scientific development. You helped me proposing my beamtimes, supported me during experiments, taught me how to evaluate and make sense of the collected data. You proofread all my proposals, posters, presentations, and, of course, this thesis and offered helpful advice on how to improve these works. I am especially thankful for all your patience and encouragement. I learned a lot from you and I greatly appreciate everything you have done for me. Without you this project would not have been possible.

For financial support I would like to thank The Hamburg Centre for Ultrafast Imaging CUI.

For sure, synchrotron experiments cannot be done by a single person and many people contributed part of their time and energy to support me. Thanks a lot to Felix Lehmkühler, Lara Frenzel, Joana Valerio, Verena Markman, Francesco Dallari, and Irina Lokteva for helping me with my experiments. You were a great help not only during beamtimes themselves but also for the preparation beforehand as well as the evaluation afterwards. Many thanks also go to the staff of the P10 beamline at PETRA III. Thank you Michael Sprung, Fabian Westermeier, and Eric Stellamanns for setting up the experiments and providing support during the beamtimes. Special thanks to Eric who supported me performing the rheological pre-characterization experiments, showed me the perks and quirks of the rheometers, and gave invaluable tips and strategies for my measurements.

I also would like to thank the FS-CXS group of DESY as a whole. I felt welcome from the very beginning and had many fruitful conversations during our time together. I learned a lot from you and had a great time. Even though they are part of this group, I want to thank some people in particular.

Thanks to Donatella for taking care of everything that needs to be taken care of. I was glad to always have your aid. You are truly the backbone of this group.

Thanks to my former office mate Joana. We became friends very fast and I always had a very nice time with you.

Thanks to Wojtek for the many nice chats, coffees, and discussions. You were always a great help, especially with everything related to Python, Matlab, or the DLS setup.

Thanks to Irina, my fellow chemist in this world of physicists. You were not only my company in the lab but also during lunch time and, of course, all the coffee breaks.

Many thanks to Christopher who was my supervisor during lab work when I studied chemistry in Rostock and later followed me to DESY in Hamburg. You became a good friend and always had an advice when I needed it.

Thank you Joachim, Annemarie, Falko, and Jules of my former group at Rostock University. You laid the foundations of my scientific development and my fascination for the world of colloids and soft matter.

Many thanks go to the team from LAVES Lüneburg who began my chemical education. A special thank you to Dorit, Regina, Jens, and Claudia who encouraged me to study chemistry and set me on this path.

Finally, my biggest thanks go to my wonderful wife, my equally amazing daughter, and my family as a whole. You were always there for me and gave me strength and support that I needed to complete this work. Without you I would not be where I am today. Vielen Dank!

Eidesstattliche Versicherung / Declaration on oath

Hiermit versichere ich an Eides statt, die vorliegende Dissertationsschrift selbst verfasst und keine anderen als die angegebenen Hilfsmittel und Quellen benutzt zu haben.

Die eingereichte schriftliche Fassung entspricht der auf dem elektronischen Speichermedium.

Die Dissertation wurde in der vorgelegten oder einer ähnlichen Form nicht schon einmal in einem früheren Promotionsverfahren angenommen oder als ungenügend beurteilt.

Hamburg, den 26.11.2021

Michael Dartsch